Nonlinear Dynamics

John F. Lindner
Physics Department
The College of Wooster

2024 July 13

Contents

List of Tables **7**

List of Figures **9**

1 Sampler **13**
1.1 A New Science . . . 13
1.2 Cellular Automata . . . 14
1.3 Billiards . . . 15
1.4 Logistics Map . . . 16
1.5 Lorenz Flow . . . 17
1.6 3-Body Problem . . . 18
1.7 Nonlinear Wave Equation . . . 19
1.8 Navier-Stokes . . . 20
Problems . . . 21

2 Maps & Flows **23**
2.1 Logistic Map . . . 23
2.2 Lorenz Flow . . . 25
Problems . . . 28

3 1D Maps **29**
3.1 Definition . . . 29
3.2 Linear Map . . . 29
3.3 Cobwebs . . . 30
3.4 Quadratic Map . . . 30
3.5 Bifurcations . . . 32
3.5.1 Overview . . . 32
3.5.2 Stability . . . 32
3.5.3 Period-1 (Fixed Point) . . . 33
3.5.4 Period-2 (2-Cycle) . . . 33
3.5.5 Superstable Orbits . . . 34
3.6 Universality . . . 35
3.6.1 Overview . . . 35
3.6.2 Sharkovsky Ordering . . . 35

3.6.3 Feigenbaum Scaling . . . 36
3.6.4 Renormalization . . . 37
3.7 Nonquadratic Maps . . . 40
Problems . . . 41

4 2D Maps 43
4.1 Mandelbrot Map . . . 43
4.2 Mandelbrot Set . . . 45
4.3 Generalized Mandelbrot Sets . . . 47
4.4 Hénon Map . . . 47
Problems . . . 50

5 Nonlinear Pendulum 51
5.1 Flows . . . 51
5.2 Classical Analysis . . . 51
5.2.1 Small Angles . . . 51
5.2.2 Large Angles . . . 52
5.3 Qualitative Analysis . . . 55
5.4 Numerical Analysis . . . 57
5.5 Forced Damped . . . 57
Problems . . . 59

6 1D Flows 61
6.1 Fixed Points . . . 61
6.2 Lyapunov Exponent . . . 61
6.3 Bifurcations . . . 63
6.3.1 Overview . . . 63
6.3.2 Limit Point . . . 63
6.3.3 Transcritical . . . 65
6.3.4 Pitchfork . . . 66
6.3.5 Broken Pitchfork . . . 67
6.3.6 Hysteresis . . . 68
6.4 Bead on Hoop Example . . . 70
Problems . . . 73

7 2D Flows 75
7.1 Fixed Points . . . 75
7.1.1 Classification . . . 75
7.1.2 Compound Example . . . 78
7.1.3 Homoclinic & Heteroclinic Orbits . . . 78
7.2 Limit Cycles . . . 80
7.2.1 Overview . . . 80
7.2.2 Limit Cycle Example . . . 80
7.2.3 Poincaré-Bendixson Theorem . . . 81
7.3 Bifurcations . . . 82
7.3.1 Overview . . . 82

7.3.2 Fixed Point . . . 82
7.3.3 Limit Cycle . . . 84
Problems . . . 85

8 3D Flows **87**
8.1 Fixed Points . . . 87
8.2 Limit Cycles . . . 89
8.3 Lorenz Flow . . . 89
8.3.1 Equations . . . 89
8.3.2 Obervations . . . 89
8.3.3 Bifurcation . . . 90
8.4 Rössler Flow . . . 93
8.4.1 Equations . . . 93
8.4.2 Observations . . . 93
8.4.3 Bifurcation . . . 93
8.5 Strange & Chaotic Attractors . . . 96
Problems . . . 98

9 The *N*-Body Problem **99**
9.1 2-Bodies . . . 99
9.2 3-Bodies . . . 101
9.3 Restricted 3-Body Problem . . . 102
9.3.1 Inertial Reference Frame . . . 102
9.3.2 Rotating Reference Frame . . . 104
9.3.3 Poincaré Section . . . 104
Problems . . . 107

10 Fractals **109**
10.1 Canonical Examples . . . 109
10.1.1 Cantor Dust . . . 109
10.1.2 Koch Curve . . . 110
10.2 Dimension Generalizations . . . 111
10.2.1 Coordinate . . . 111
10.2.2 Similarity . . . 111
10.2.3 Box . . . 112
10.2.4 Correlation . . . 113
10.3 Applications . . . 114
Problems . . . 115

A Mathematics Background **117**
A.1 Complex Numbers . . . 117
A.2 Hyperbolic Functions . . . 118
A.3 Spatial Rotations . . . 120
A.4 Partial Derivatives . . . 121
A.5 Function Notation . . . 121
Problems . . . 122

Bibliography **123**

List of Tables

9.1 3-Body Parameters. 103

List of Figures

1.1 Rule 110 Evolution 14
1.2 Chaotic Billiards 15
1.3 Logistics Series 16
1.4 Lorenz state space 17
1.5 3-body orbit 18
1.6 Classical Waves 19
1.7 Navier-Stokes 20

2.1 Quadratic Map 23
2.2 Logistics Period 2 and ∞ 24
2.3 Logistics Period 3 and ∞ 24
2.4 Rayleigh-Bénard Convection, ... 25
2.5 Lorenz Steady & Chaotic 26
2.6 Lorenz Map 26

3.1 Linear Cobwebs 30
3.2 Quadratic Cobwebs 31
3.3 Quadratic Bifurcations 32
3.4 Quadratic 2-Cycle 34
3.5 Quadratic Superstable 35
3.6 Sharkovsky Ordering 36
3.7 Bifurcation Scaling 37
3.8 Translation & Dilation 37
3.9 Superstable Bifurcations 38
3.10 Renormalization 39
3.11 Nonquadratic Map 40

4.1 Mandelbrot Maps Unit Circle 44
4.2 Mandelbrot Fixed Point Stability 45
4.3 Mandelbrot 46
4.4 Mandelbrot Generalization 47
4.5 Henon Transformations 48
4.6 Henon Attractor 48
4.7 Henon Chaos 49

5.1 Pendulum . . . 52
5.2 Pendulum Time Series . . . 54
5.3 Pendulum Period . . . 55
5.4 Pendulum State Space . . . 56
5.5 Pendulum Viscosity State Space . . . 56
5.6 Pendulum State Space Gallery . . . 58

6.1 1D Velocity Fields . . . 62
6.2 1D Bifurcations . . . 63
6.3 Pair Creation . . . 64
6.4 Pair Annihilation . . . 65
6.5 Transcritical Bifurcations . . . 66
6.6 Pitchfork Bifurcations . . . 67
6.7 Broken Pitchforks . . . 68
6.8 Hysteresis Bifurcation . . . 69
6.9 Hysteresis Cycle . . . 69
6.10 Bead on a Hoop . . . 70
6.11 Bead on a Hoop Bifurcation Diagram . . . 72
6.12 Bead on a Hoop Equilibria . . . 72

7.1 Generic 2D Fixed Points . . . 76
7.2 2D Fixed Point Classification . . . 77
7.3 Example 2D Flow . . . 78
7.4 Homoclinic Heteroclinic Orbits . . . 79
7.5 2D Limit Cycle . . . 81
7.6 Supercritical Hopf Bifurcation . . . 83
7.7 Subcritical Hopf Bifurcation . . . 83

8.1 Fixed Point Classification 3D . . . 88
8.2 Saddle Cycle 3D . . . 89
8.3 Lorenz Bifurcation . . . 91
8.4 Lorenz Bifurcating Flows . . . 92
8.5 Rössler Bifurcation . . . 94
8.6 Rössler Bifurcating Flows . . . 95
8.7 Lorenz & Rössler Geometry . . . 96
8.8 Lorenz & Rössler Maps . . . 97

9.1 Kepler Orbit Complex Plane . . . 99
9.2 Kepler Orbit . . . 101
9.3 3-Body Orbit . . . 103
9.4 3-Body Section . . . 105
9.5 3-Body Section Closeup . . . 106
9.6 3-Body Tangle . . . 106

10.1 Cantor Set . . . 109
10.2 Koch Curve . . . 110

10.3 Scaling 111
10.4 Box Covering 112
10.5 Box Dimension 113
10.6 Correlation 2D 114
10.7 Correlation Dim 114

A.1 Complex plane 118
A.2 Hyperbolic functions 119
A.3 Rotated coordinates 120

Chapter 1

Sampler

1.1 A New Science

Twentieth century physics may be remembered for three great knowledge revolutions: relativity, quantum mechanics, and **chaos**.

Chaos, or more generally **nonlinear dynamics**, was anticipated by mathematician Henri Poincaré [11] at the dawn of the century. It blossomed in the twenty years 1960-1980, facilitated in part by the availability of cheap and fast computers, and thanks to the efforts of researchers like meteorologist Edward Lorenz [6] and physicist Mitchell Feigenbaum [3].

Nonlinear dynamics includes a rich variety of fascinating behavior. While the output of a linear system is simply proportional to the input, the response of a nonlinear system may vary widely as the input varies. This can lead to the extreme sensitivity to initial conditions that characterizes chaotic dynamics.

Nonlinear dynamics is ubiquitous. Linear systems, although simpler to analyze, are the exception rather than the rule (everywhere, that is, except in typical introductory physics courses). In this regard, the mathematician Stanislaw Ulam is purported to have said, "Studying nonlinear dynamics is like studying nonelephant animals".

Nonlinear dynamics is an interdisciplinary science. Applications abound in mathematics, physics, biology, engineering, and economics, among other disciplines, and ideas from researchers in one area cross fertilize with ideas from researchers in other areas.

The new science of nonlinear dynamics has wrested an important insight from nature: Even simple nonlinear systems can exhibit very complicated chaotic motion, which is **nonperiodic** yet **deterministic** and extremely **sensitive** to initial conditions.

Conversely, irregular phenomena need not require complicated or stochastic modeling equations. Simple systems need not behave in complex ways. Complex behavior may not require complex causes. Yet, diverse nonlinear systems often share chaotic dynamics with common features. There is **universality** in chaos.

1.2 Cellular Automata

Broadly construed, a dynamical system is one that evolves according to a set of rules. For cellular automata, space and time are discrete. For example, the updates

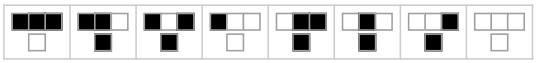

(1.1)

define Wolfram's Rule 110. Figure 1.1 is a typical evolution from random initial conditions. Rule 110 is **Turing-complete** and hence is computationally universal.

Figure 1.1: Example evolution of cellular automaton Rule 110.

1.3 Billiards

When a ball collides **elastically** with a frictionless wall, the normal component of its velocity reverses, so the simple map

$$v_{\parallel} \leftarrow +v_{\parallel}, \tag{1.2a}$$
$$v_{\perp} \leftarrow -v_{\perp} \tag{1.2b}$$

determines its dynamics. If the walls are circular or rectangular, the motion is periodic. However, more complicated geometries can produce a mix of order and chaos, as in Fig. 1.2, where each color in the **sectional plot** records the angular location θ and tangential momentum p_θ of each collisions with the outer circle. Rows of dots at the top and bottom of the section correspond to orbits that skim along the outer circle, either clockwise or counterclockwise, without colliding with the inner circle.

Quantum versions of classical billiards manifest the classically chaotic orbits in the statistics of their energy **eigenvalue** separations and manifest the classically periodic orbits in "scars" in their **eigenfunctions**.

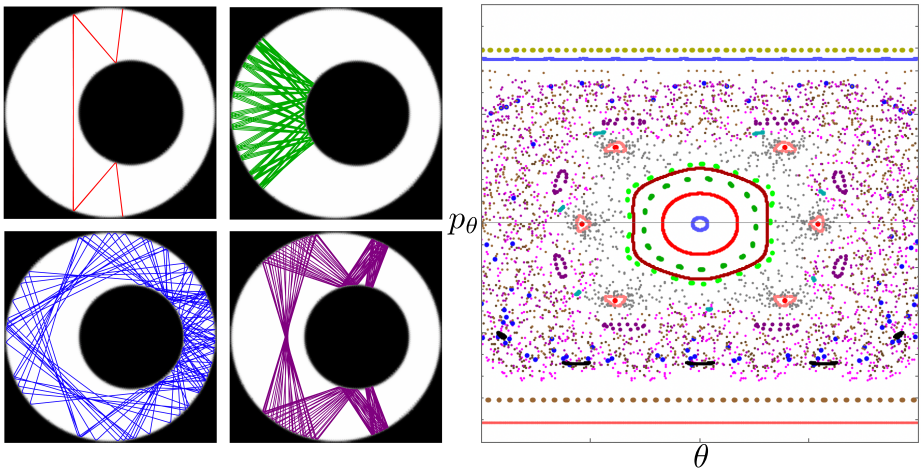

Figure 1.2: Point particle bouncing elastically between two circles (left) can execute regular or irregular motion, which can be summarized in a sectional plot of tangential momentum p_θ versus angular location θ for the nth collision (right), where each color corresponds to a different orbit.

1.4 Logistics Map

The logistics map is a simple biological model of population growth. It models the evolution of a population in a limited environment with linear growth and quadratic die-off according to the iterated map

$$x \leftarrow \mu x(1-x), \tag{1.3}$$

or difference equation

$$x_{n+1} = \mu x_n(1-x_n), \tag{1.4}$$

where x represents the normalized population and n indicates the generation. The normalized population exhibits an extraordinary range of varied and subtle behavior as the growth parameter μ changes, as in Fig. 1.3.

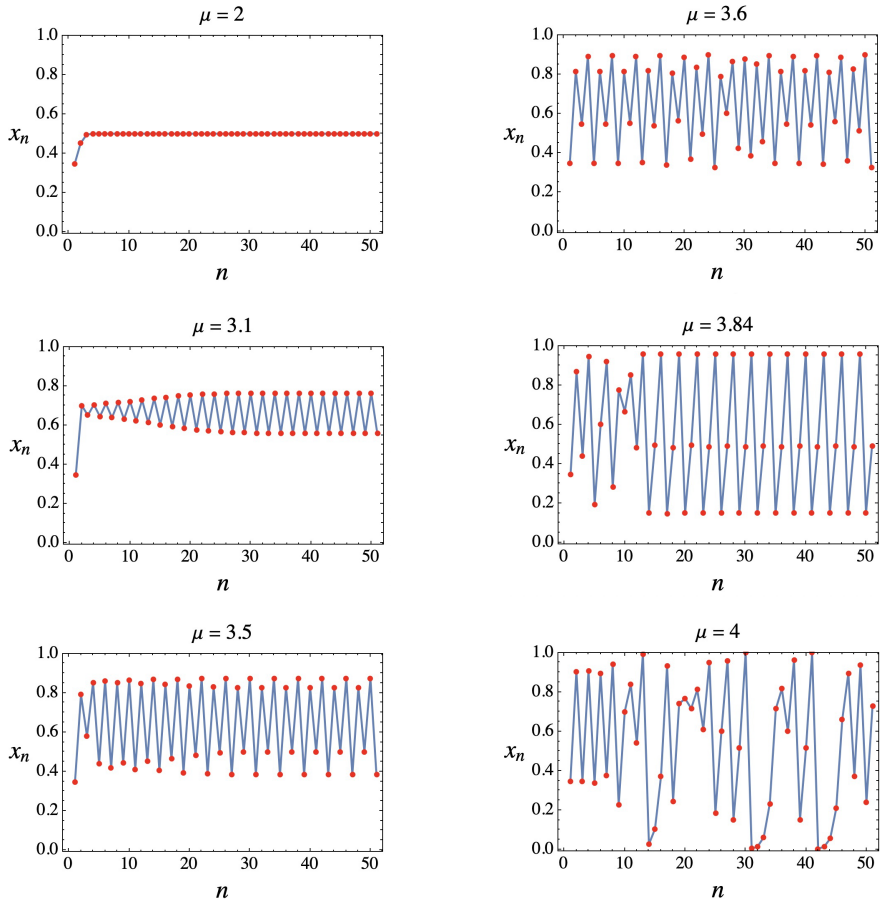

Figure 1.3: Logistics evolution exhibits both periodic and chaotic evolution as the growth parameter μ changes.

1.5 Lorenz Flow

The Lorenz flow is a simple model of a convecting fluid. It was invented and first studied by meteorologist Edward Lorenz [6] in the 1960s. Lorenz (not Lorentz) considered a fluid under combined gravity and temperature gradients described by the system of first-order differential equations

$$\dot{x} = -\sigma x + \sigma y, \tag{1.5a}$$
$$\dot{y} = +\rho x - y - xz, \tag{1.5b}$$
$$\dot{z} = -\beta z + xy. \tag{1.5c}$$

For some parameters the fluid motion is irregular and never repeats, as in Fig. 1.4.

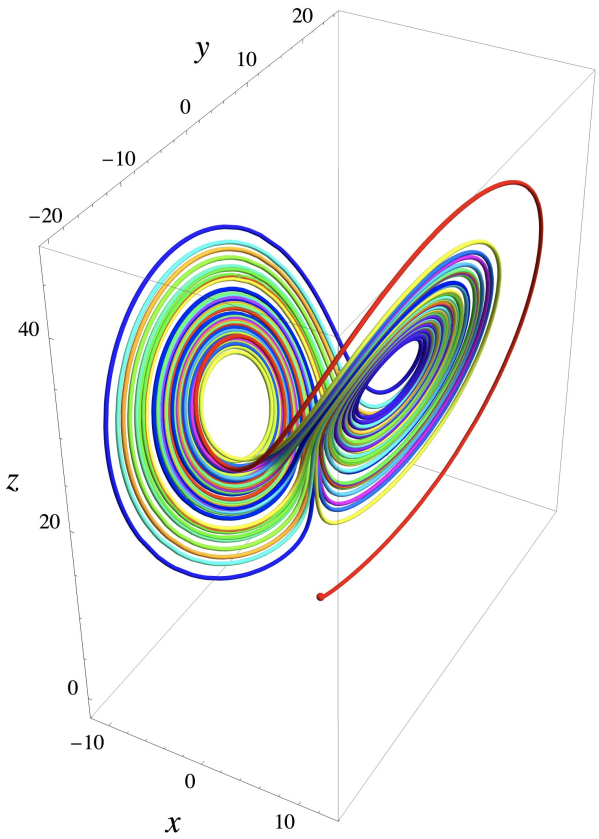

Figure 1.4: Chaotic cycling of the Lorenz weather model in its $\{x, y, z\}$ state space. Rainbow hues code time, from red to violet.

1.6 3-Body Problem

The positions $\vec{r}_i = \{x_i, y_i, z_i\}$ of n point masses m_i interacting via Newtonian gravity obey the system of second-order differential equations

$$m_i \ddot{\vec{r}}_i = -\sum_{j \neq i} \frac{G m_i m_j}{r_{ij}^2} \hat{r}_{ij} = -\sum_{j \neq i} \frac{G m_i m_j}{\|\vec{r}_i - \vec{r}_j\|^3} (\vec{r}_i - \vec{r}_j) \,, \tag{1.6}$$

where the over-dots denote time differentiation, the indices $i, j \in \{1, 2, 3, \ldots, n\}$, and the unit vector $\hat{r} = \vec{r}/r$. Henri Poincaré famously discovered [11] extreme sensitivity to initial conditions or chaos in these orbits, as suggested by Fig. 1.5.

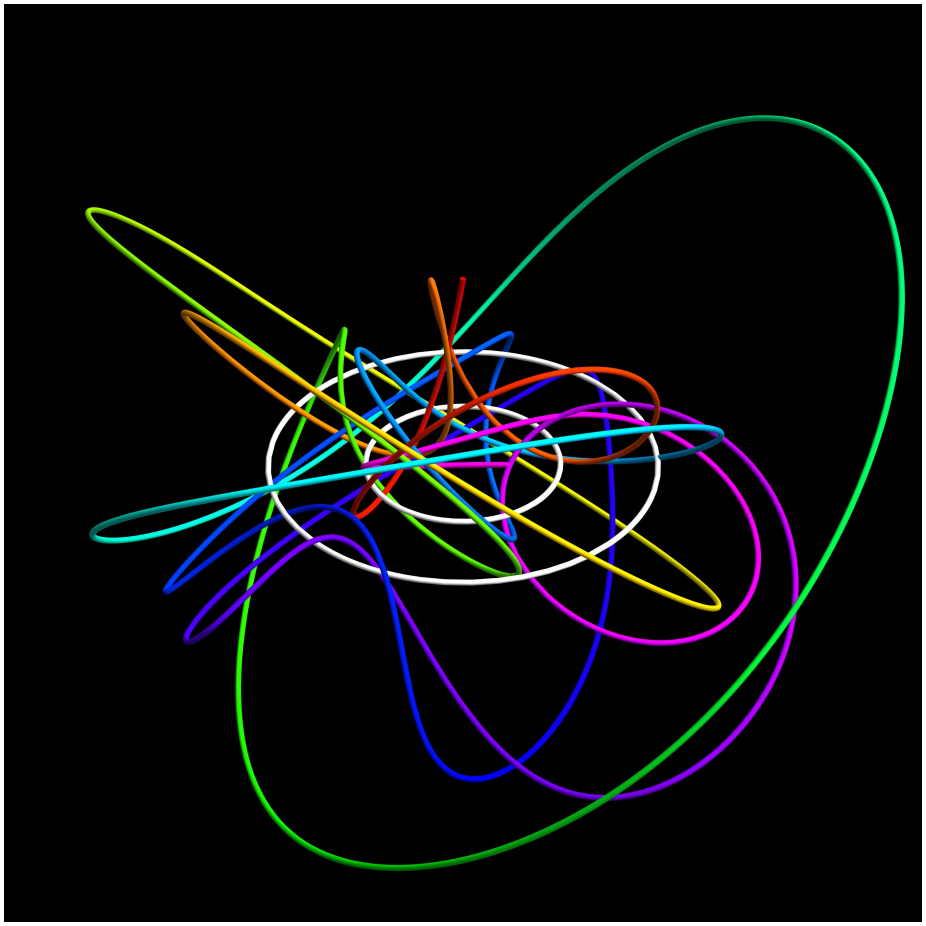

Figure 1.5: Asteroid released from rest directly above the orbit of two binary stars. Rainbow hues code time, from red to violet.

1.7 Nonlinear Wave Equation

The nonlinear **Sine-Gordon** partial differential equation

$$\Box^2\varphi = \partial_x^2\varphi - \partial_t^2\varphi = \sin\varphi \tag{1.7}$$

describes the continuum limit of a linear array of pendulums rotated by angles φ from their stable equilibria and coupled by torsional springs in a gravitational field. For small angles, $\sin\varphi \sim \varphi \ll 1$, and it becomes the linear **Klein-Gordon** equation, which describes spinless relativistic quantum particles or wave propagation in a **dispersive** medium. By contrast, the **classical wave equation**

$$\Box^2\varphi = \partial_x^2\varphi - \partial_t^2\varphi = 0 \tag{1.8}$$

describes wave propagation in a **dispersionless** medium. When nonlinear **solitons** collide, they interact nontrivially instead of merely superposing, as in Fig. 1.6 (bottom), where a soliton collides with a stationary **breather** and permanently shifts it. In this way, soliton or breather-like solutions to nonlinear wave equations can model atoms.

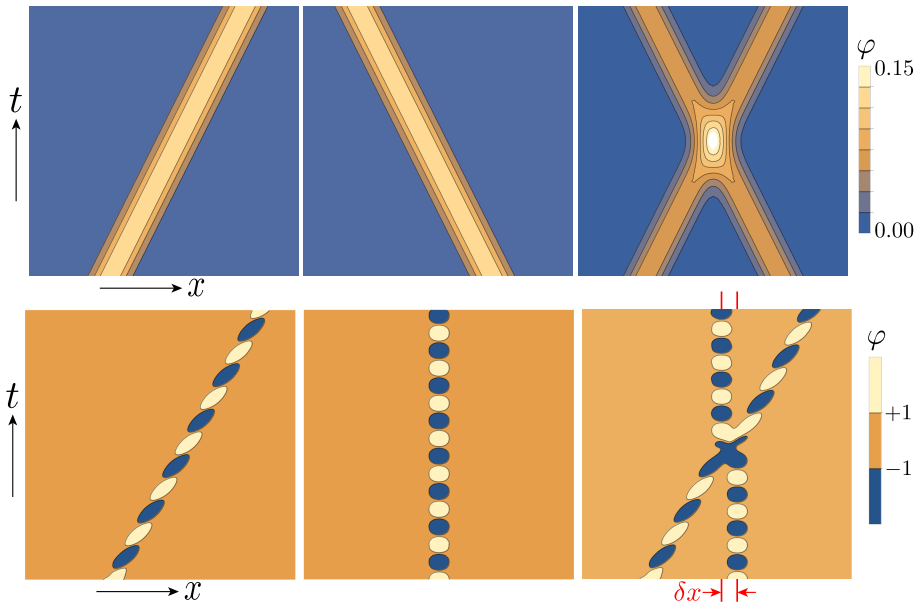

Figure 1.6: Spacetime contour plots of solitary solutions or solitons. Classical waves obey a linear wave equation (top), and trivial solitons pass through each other unaffected. Sine-Gordon solitons obey a nonlinear wave equation (bottom), support both propagating and nonpropagating modes, and collide with an interaction that shifts the stationary breather mode.

1.8 Navier-Stokes

The velocity $\vec{v} = \{v_x, v_y\}$ and pressure p of an incompressible, divergence-free

$$\vec{\nabla} \cdot \vec{v} = 0 \tag{1.9}$$

2D fluid flow obey the **Navier-Stokes** force-per-volume partial differential equation

$$\rho \left(\frac{\partial \vec{v}}{\partial t} + \vec{v} \cdot \vec{\nabla} \vec{v} \right) = -\vec{\nabla} p + \mu \nabla^2 \vec{v}, \tag{1.10}$$

where ρ is density and μ is viscosity. As one of the Clay Mathematics Institute's Millennium Problems, one million dollars is available for a proof of existence and uniqueness of solutions of this equation.

Place a circular obstacle in the fluid flow. At low speeds, the flow is smooth and laminar. At intermediate speeds, vortices develop downstream, as in Fig. 1.7, and begin to shed, creating a **von Kármán vortex street**. At high speeds, downstream of the cylinder becomes turbulent. According to Lewis Fry Richardson [12],

> Big whorls have little whorls
> Which feed on their velocity,
> And little whorls have lesser whorls
> And so on to viscosity.

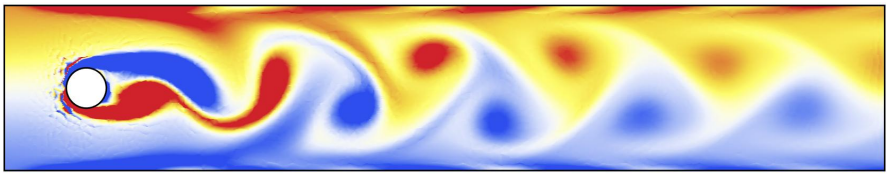

Figure 1.7: Fluid flow behind a cylinder is laminar for low speeds, vortex shedding for intermediate speeds (shown), and turbulent for high speeds. Colors code vorticities $\vec{\nabla} \times \vec{v}$, with blue positive and red negative.

Problems

1. **Rule 110.** Hand simulate Wolfram's Rule 110 on 16×16 quad ruled paper (or similar). Continue the investigation on a larger scale using Mathematica. Try different initial conditions.

2. **Classical Wave Equation.** Differentiate with the chain rule to verify that the linear classical wave Eq. 1.8 has solutions

$$\varphi[x,t] = f[x-t] + g[x+t] \tag{1.11}$$

for any functions $f[\bullet]$ and $g[\bullet]$, which are **superpositions** of waves of any shapes moving in both directions at velocities ± 1.

3. **Sine-Gordon Equation.** Differentiate with the chain rule to verify that the nonlinear Sine-Gordon wave Eq. 1.7 has **soliton** and **breather** solutions

$$\varphi[x,t] = 4\arctan\left[\sqrt{\frac{1-\omega^2}{\omega^2}}\frac{\cos\left[\omega(t-vx)/\sqrt{1-v^2}\right]}{\cosh\left[\sqrt{1-\omega^2}(x-vt)/\sqrt{1-v^2}\right]}\right], \tag{1.12}$$

with frequency ω and velocity v. (Hint: Use Mathematica's TrigExpand and Simplify assuming $|\omega| < 1$ and $|v| < 1$.)

Chapter 2

Maps & Flows

As in introduction to nonlinear dynamics, first focus on two canonical examples, the **logistics map** and the **Lorenz flow**.

2.1 Logistic Map

The logistics map is a simple biological model of population growth. It has a long history, but it was popularized and studied in the 1970s by biologist Robert May [10] and physicist Mitchell Feigenbaum [3]. It models the evolution of a population in a limited environment with linear growth and quadratic die-off. Represent it as the map

$$x \leftarrow \mu x(1-x), \tag{2.1}$$

or difference equation

$$x_{n+1} = \mu x_n(1-x_n), \tag{2.2}$$

where x is the normalized population and n is the generation. A plot of the left side versus the right, for a fixed value of the parameter μ, results in a parabola, as in Fig. 2.1. What happens to iterates of the map as the parameter μ varies?

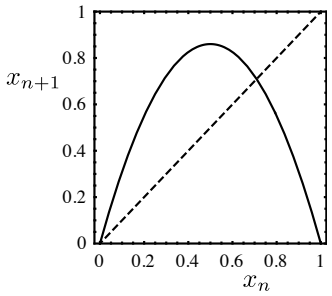

Figure 2.1: A parabola defines the quadratic logistics map.

In honor of Robert May [10], suppose the map represents the population of mayflies, as in Fig. 2.2. For small μ, after an initial transient, and for almost all initial conditions, iterates of x are attracted to a fixed point of 0.5; the mayflies' population reaches a steady state of half its maximum. Larger μ results in a period-2 steady state; the population alternates between large generations (which overtax the mayflies' resources) and small generations (which under use the mayflies' resources). Still larger μ results in a period-4 steady state, a period-8 steady state, and so on, in a period-doubling cascade. At about $\mu = 3.6$, the period of the orbit is infinite, and the population of mayflies never settles down but varies randomly from one generation to the next.

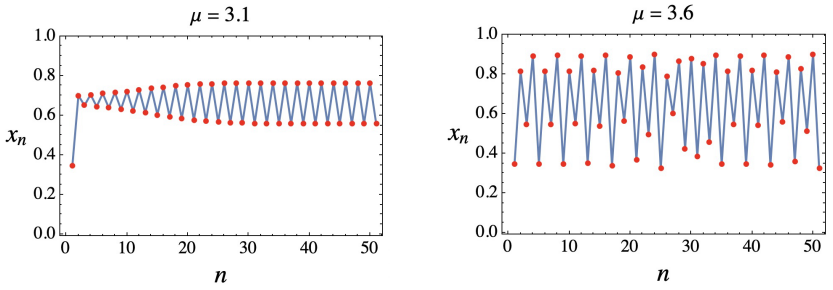

Figure 2.2: Logistics map period-2 (left) and period-∞ (right) orbits.

In exasperation, May purportedly challenged his graduate students to figure out what happens next, as μ is increased further. Surprisingly, at about $\mu = 3.84$, a period-3 orbit emerges from chaos, as in Fig. 2.3. In the 1970s, mathematicians Tien-Yien Li and James Yorke would coin **chaos** as a new scientific term in the article "Period Three Implies Chaos" [5], and Feigenbaum [3] would uncover a geometrical universality underlying the period-doubling route to chaos.

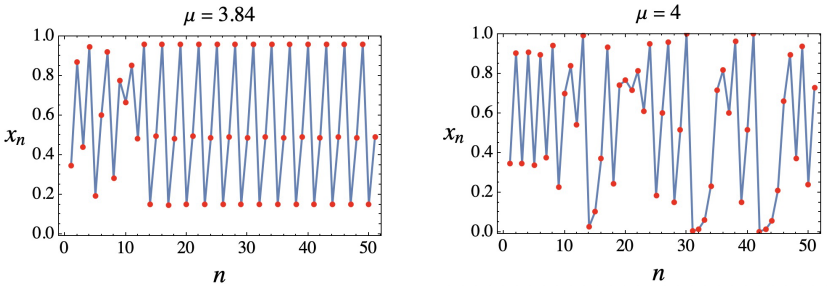

Figure 2.3: Logistics map period-3 (left) and period-∞ (right) orbits. Some early computers used the latter orbit as a pseudo-random number generator.

2.2 Lorenz Flow

The Lorenz flow is a simple model of a convecting fluid. It was invented and first studied by meteorologist Edward Lorenz [6] in the 1960s. Lorenz considered a fluid under combined gravity and temperature gradients, as in Fig. 2.4

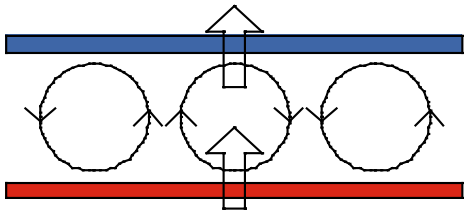

Figure 2.4: In Rayleigh-Bénard convection, a fluid circulates between a hot bottom plate and a cold top plate.

The fluid absorbs heat at the bottom hot plate, becomes buoyant and rises, releases the heat to the cold top plate, becomes dense and descends. This is the mechanism behind **Rayleigh-Bénard convection**. Lorenz "boiled" the problem down to a system of three ordinary differential equations in three unknowns,

$$\dot{x} = -\sigma x + \sigma y, \tag{2.3a}$$
$$\dot{y} = +\rho x - y - xz, \tag{2.3b}$$
$$\dot{z} = -\beta z + xy. \tag{2.3c}$$

The velocity of the convecting fluid can be derived from the variable x, while the vertical temperature difference across the fluid is proportional to the parameter ρ. What happens to the dynamics as ρ varies?

For small ρ, the temperature differential does not induce sufficient buoyancy for the fluid to overcome viscosity, and no fluid motion results. For larger ρ, the buoyancy of the heated fluid generates steady convection, clockwise or counterclockwise, depending upon the initial conditions, as in Fig. 2.5. This steady cellular flow spontaneously breaks the **space-translation symmetry** of the system. At even higher ρ, the fluid in the fast-turning convection rolls have little time to release their heat to the cold top plate; consequently, they can start descending and find themselves lighter than the surrounding fluid, making a reversal possible. This irregular motion persists for all time, never repeating exactly, thereby spontaneously breaking the **time-translation symmetry** of the system.

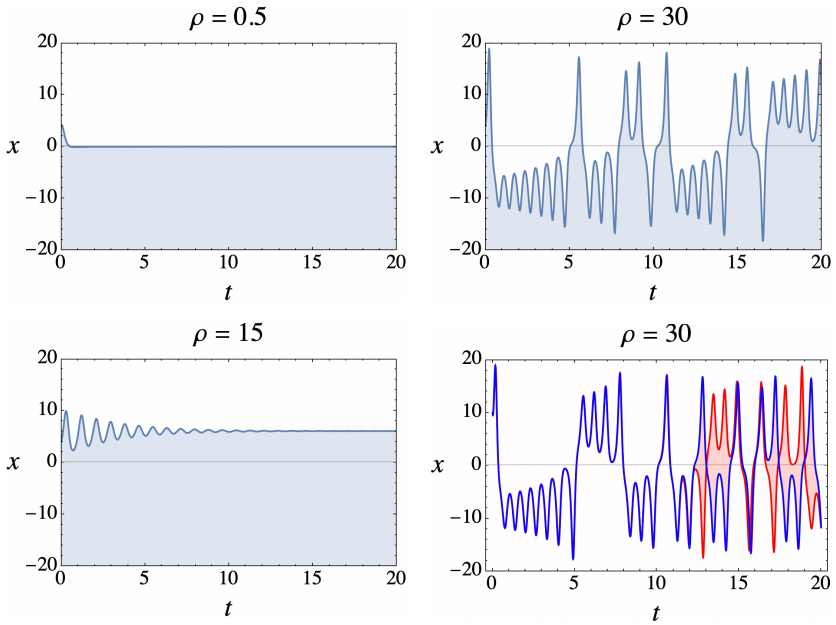

Figure 2.5: Lorenz flow x-coordinate as parameter ρ increases from no flow (top left) to steady-state circulation (bottom left) to chaotic flow (top right) exhibiting extreme sensitivity to initial condition (bottom right), where blue and red time series diverge even with virtually the same start.

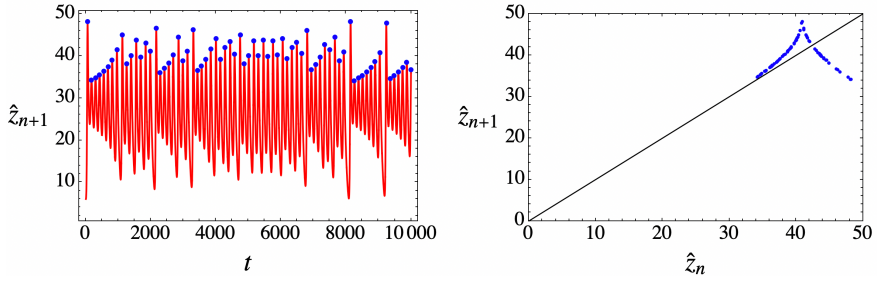

Figure 2.6: Chaotic Lorenz flow z-coordinate for $\rho = 30$ (left) and Lorenz map of successive maxima (right) demonstrates order within chaos.

Furthermore, Lorenz demonstrated that this deterministic nonperiodic flow also exhibits extreme sensitivity to initial conditions, the third essential ingredient of chaos. In a lecture in 1972, Lorenz coined the phrase **the butterfly effect** when he wondered if the flap of a butterfly's wings in Brazil could initiate a tornado in Texas [7].

However, Lorenz also found **order within chaos**. He located successive maxima in the z-component of the flow and plotted each maximum against the previous maximum, as in Fig. 2.6. Instead of a featureless blob, he found a curve (with a slight thickness), thereby reducing a 3D flow to a 1D map, and enabling him to use the current maximum to predict the next maximum.

Problems

1. **Logistics Time Series** Create a Mathematica manipulator and use it study the logistics time series, as in Fig. 2.2.

2. **Lorenz Time Series** Create a Mathematica manipulator and use it study the Lorenz time series, as in Fig. 2.5.

Chapter 3

1D Maps

Fascinating in themselves, one-dimensional (1D) maps are also useful in analyzing flows.

3.1 Definition

Maps are defined by **difference equations**, like

$$\vec{x}_{n+1} = \vec{f}_p[\vec{x}_n], \tag{3.1}$$

where p is a parameter. For simplicity, sometimes omit the indices labeling successive iterations and write

$$\vec{x} \leftarrow \vec{f}[\vec{x}\,]. \tag{3.2}$$

The dimension of the map is the dimension of the vector $\vec{x}$.

3.2 Linear Map

The most general 1D linear map can be expressed as the 2-parameter difference equation

$$x_{n+1} = Ax_n + B. \tag{3.3}$$

By scaling and translating x appropriately with $x \leftarrow \sigma x + \delta$, reduce this to the 1-parameter map

$$x_{n+1} = Ax_n. \tag{3.4}$$

This difference equation is explicitly solved by

$$x_n = A^n x_0. \tag{3.5}$$

The origin $x_0 = 0$ is a **fixed point** for the map. The fixed point is **stable** for $|A| < 1$, and it is an **attractor** to which all iterates converge. The fixed point is **unstable** for $|A| > 1$, and it is a **repellor** away from which all iterates diverge to infinity.

3.3 Cobwebs

A good way to graphically analyze 1D maps is the cobweb **construction**. Superimpose a 45° line on a plot of a map $f[x]$. Draw a vertical line from the initial iterate x_0 to $f[x_0]$, then alternate drawing horizontal lines to the 45° line to find x_n and vertical lines back to $f[x_n]$. Figure 3.1 illustrates this "vertical to the curve and horizontal to the diagonal" procedure for linear maps.

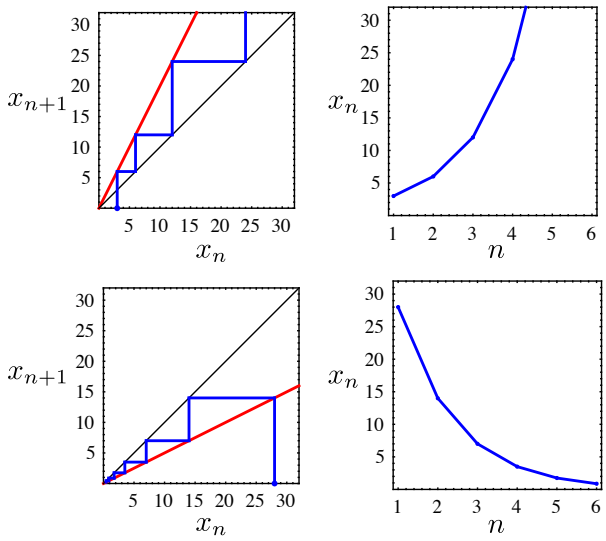

Figure 3.1: Cobweb construction for steep linear map, where iterates diverge to infinity (top); cobweb construction for shallow linear map, where iterates converge to zero.

3.4 Quadratic Map

The most general 1D quadratic map can be expressed as the 3-parameter map

$$x_{n+1} = Ax_n^2 + Bx_n + C. \tag{3.6}$$

By scaling and translating x appropriately with $x \leftarrow \sigma x + \delta$, reduced this to the 1-parameter map

$$x_{n+1} = x_n^2 + C, \tag{3.7}$$

which is simplest and fastest for numerical calculations or

$$x_{n+1} = \mu x_n(1 - x_n), \tag{3.8}$$

which is best for graphical illustration and is often called the **logistics map**. The Fig. 3.2 cobweb constructions elucidate some of the rich behavior of this well-studied map.

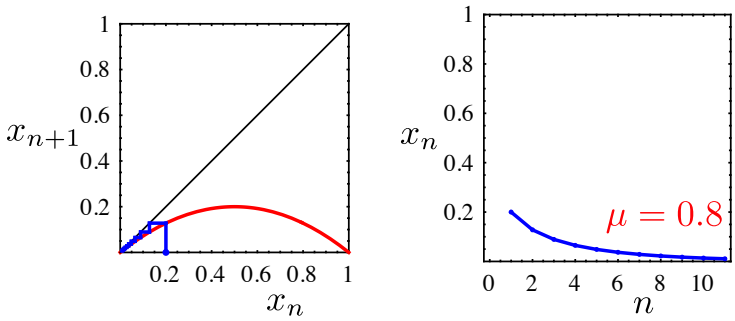

Origin is a stable period-1 (fixed point attractor).

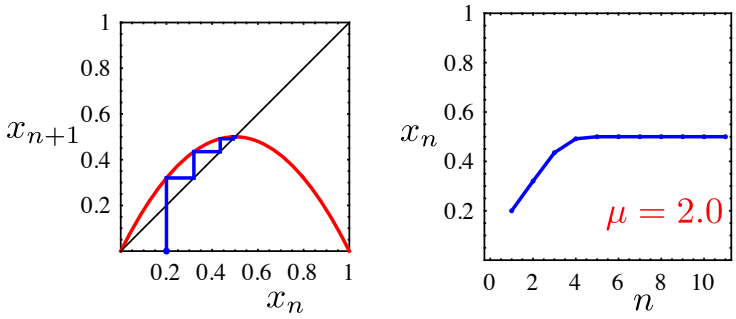

Origin becomes an unstable repellor.

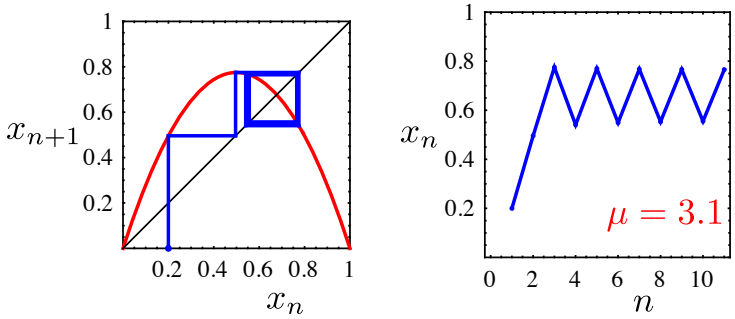

A 2-cycle attracts almost all orbits.

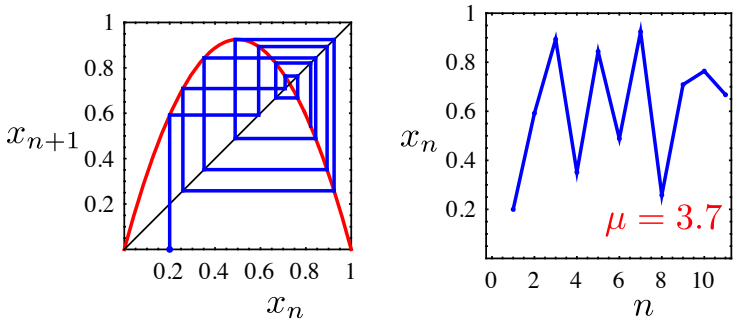

Aperiodic orbit, characteristic of chaos.

Figure 3.2: Cobwebs and time series for the quadratic map for $0.8 \leq \mu \leq 3.7$.

3.5 Bifurcations

3.5.1 Overview

A famous picture summarizes the intricate asymptotic behavior of iterates of the logistics map. For each μ, iterate the map many times until the orbit settles down to some attracting set, and plot these points. The Fig. 3.3 **bifurcation diagram**, sometimes called Feigenbaum's fig tree ("feigen baum" = "fig tree"), summarizes these **qualitative changes**.

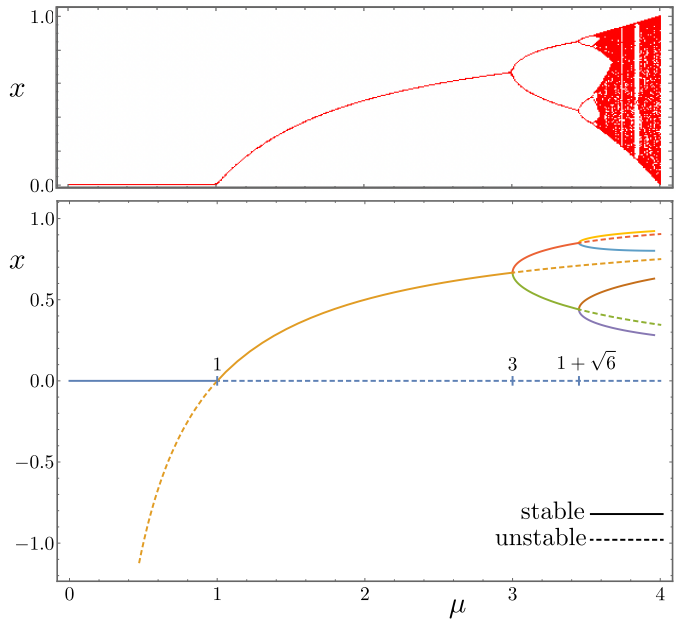

Figure 3.3: Logistics map asymptotic invariant sets bifurcate as the parameter μ varies from 0 to 4 (top); exact structure of stable and unstable manifolds (bottom).

3.5.2 Stability

Suppose that x_* is a fixed point of a map f, so $f[x_*] = x_*$. What is the **stability** of x_*? Are orbits that start nearby x_* attracted to or repelled from x_*? Let

$$x_n = x_* + \xi_n, \tag{3.9}$$

and expand

$$x_{n+1} = f[x_n] \tag{3.10}$$

in a **Taylor series** about x_* to get

$$\xi_{n+1} = f'[x_*]\xi_n + \mathcal{O}[\xi_n^2]. \tag{3.11}$$

From above, this linear map is stable provided the absolute value of the slope of the map at the fixed point is less than unity, $|f'[x_*]| < 1$, and unstable if this slope is greater than unity, $|f'[x_*]| > 1$. (Higher order terms in the Taylor series expansion determine the stability in the special case of unit slope, $|f'[x_*]| = 1$.)

3.5.3 Period-1 (Fixed Point)

First investigate the fixed points of the logistics map. Solve

$$x_* = f_\mu[x_*] = \mu x_*(1 - x_*) \tag{3.12}$$

to find

$$x_* = 0 \tag{3.13}$$

or

$$x_* = 1 - 1/\mu. \tag{3.14}$$

Now solve

$$1 > |f'[x_*]| = \mu(1 - 2x_*) \tag{3.15}$$

at each of these points to find that $x_* = 0$ is stable for $\mu < 1$ and $x_* = 1 - 1/\mu$ is stable for $1 < \mu < 3$, as in Fig. 3.3.

3.5.4 Period-2 (2-Cycle)

At μ increases through 3 a stable fixed point bifurcates into a stable **2-cycle** as the fixed point becomes unstable. A 2-cycle $x_\pm$ of the map, namely $f[x_\pm] = x_\mp$ or

$$f[x_+] = x_-, \tag{3.16a}$$

$$f[x_-] = x_+, \tag{3.16b}$$

consists of two fixed points of the twice nested map,

$$f\big[f[x_\pm]\big] = x_\pm, \tag{3.17}$$

as illustrated by Fig. 3.4, where $x_{n+2} = f\big[f[x_n]\big]$.

Investigate the 2-cycle of the map by studying the fixed point of the twice nested map. Solve

$$x_\pm = f\big[f[x_\pm]\big] = \mu\big(\mu x_\pm(1 - x_\pm)\big)\big(1 - \mu x_\pm(1 - x_\pm)\big) \tag{3.18}$$

to find the equations for its two branches

$$x_\pm = \frac{(\mu + 1) \pm \sqrt{(\mu - 3)(\mu + 1)}}{2\mu}. \tag{3.19}$$

Because, $x_\pm = 2/3 = x_*$ at $\mu = 3$, the bifurcation is continuous. Next solve

$$1 > \left|\frac{d}{dx} f\big[f[x_\pm]\big]\right| = f'\big[f[x_\mp]\big] f'[x_\pm] = f'[x_\mp] f'[x_\pm] = \mu(1 - 2x_\mp)\mu(1 - 2x_\pm) \tag{3.20}$$

to find that the $x_\pm$ 2-cycle is stable for $3 < \mu < 1 + \sqrt{6}$, as in Fig. 3.3.

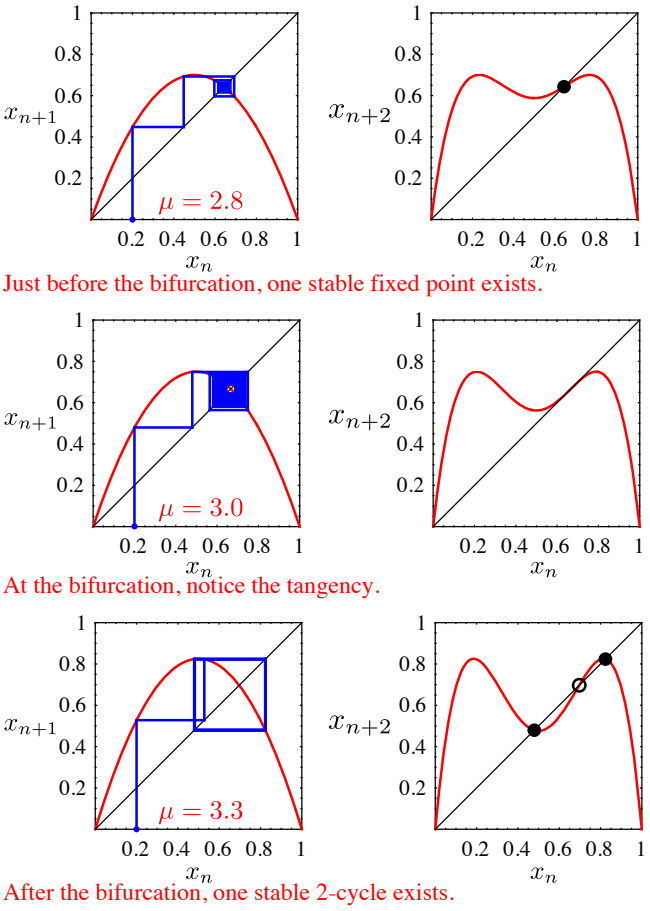

Figure 3.4: Logistics 2-cycle emerges as μ passes through 3.

3.5.5 Superstable Orbits

Superstable orbits pass through the **critical point** where the slope of the map vanishes. Stability of the fixed point x_* requires $1 > |f'[x_*]|$; superstability requires that this be minimized by $0 = |f'[x_*]$. Stability of a period n-cycle requires

$$1 > \left|f^{n\prime}[x_1]\right| = \left|f'[x_n]f'[x_{n-1}]\cdots f'[x_1]\right|; \tag{3.21}$$

superstability requires that this be minimized by

$$0 = f^{n\prime}[x_1] = f'[x_n]f'[x_{n-1}]\cdots f'[x_1], \tag{3.22}$$

and this happens if any iterate of the orbit is a critical point, $f'[x_i] = 0$.

The superstable orbits shape the bifurcation diagram as nearby orbits stay close by, at least for a while, due to the vanishing derivative. The results are

crests of high density that sweep through the bifurcation diagram, as illustrated by Fig. 3.5.

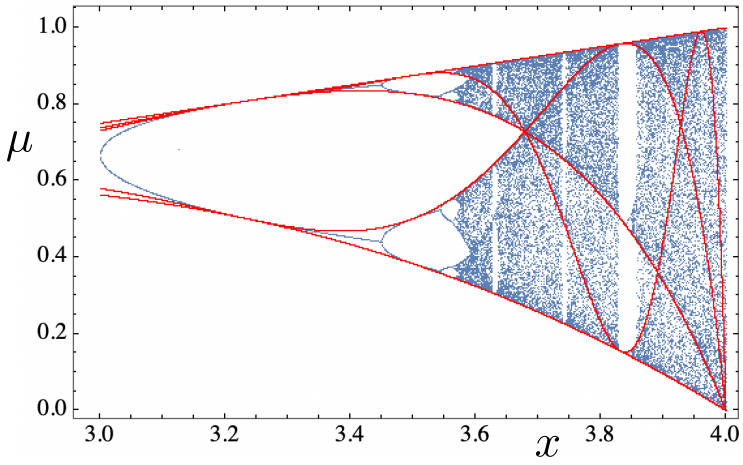

Figure 3.5: First five iterates of superstable orbits (red) outline bifurcation diagram (blue).

3.6 Universality

3.6.1 Overview

The logistics map shares qualitative (or topological) features as well as quantitative (or metrical) features in common with a whole class of unimodal maps with quadratic maxima. These include the sine map $f(x) = \mu \sin x$ but not the quartic map $f(x) = \mu - x^4$. Next investigate some of these universal features.

3.6.2 Sharkovsky Ordering

In the 1970s, Li and Yorke published a famous article entitled "Period-3 Implies Chaos" [5]. They established a remarkable result, independently obtained by Sharkovsky in the 1960s [14]. Consider the following ordering of the **natural numbers**, visualized by Fig. 3.6,

$$\begin{aligned} 1 \prec 2 \prec 2^2 \prec 2^3 \prec \cdots & \\ & \cdots \\ & \cdots \prec 9 \times 2^3 \prec 7 \times 2^3 \prec 5 \times 2^3 \prec 3 \times 2^3 \\ & \cdots \prec 9 \times 2^2 \prec 7 \times 2^2 \prec 5 \times 2^2 \prec 3 \times 2^2 \\ & \cdots \prec 9 \times 2 \prec 7 \times 2 \prec 5 \times 2 \prec 3 \times 2 \\ & \cdots \prec 9 \prec 7 \prec 5 \prec 3, \end{aligned} \tag{3.23}$$

where $x \prec y$ means x **precedes** y, so 3 is the last element in the sequence. If a continuous map f of an interval onto itself has a periodic point with period n, then f also has a periodic point of period $m \prec n$. An immediate corollary is that if the map has a period-3 orbit, it also has a period-∞ orbit, a necessary ingredient of chaos. Because almost all of these orbits are unstable, as in Fig. 3.3, they cannot be experimentally observed. However, these unstable orbits can influence the dynamics. Furthermore, because each unstable orbit is typically born in a pitchfork bifurcation, the stable periodic orbits first appear in the reverse order of the U-sequence. For example, the logistics map first undergoes a period doubling cascade to a chaotic accumulation point $\mu \approx 3.57$, afterwards periodic windows first appear culminating in the large period-3 window at $\mu \approx 3.83$.

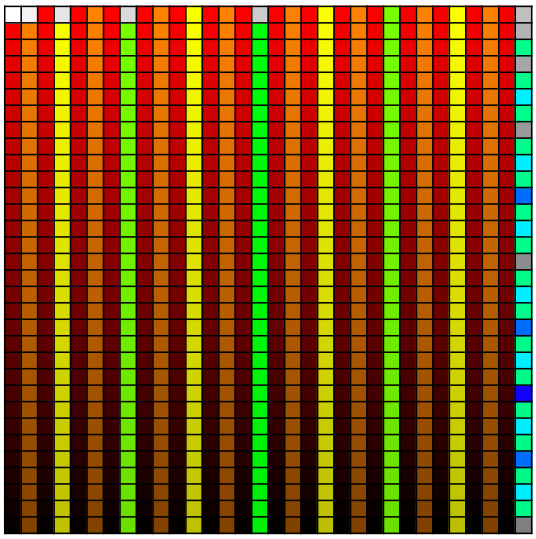

Figure 3.6: Raster pattern of 2^{10} squares colored according to the Eq. 3.23 Sharkovsky ordering. Gray squares represent powers-of-two and darken with increasing power; colored squares represent power-of-two multiples of odd numbers and redden with increasing powers and brighten with increasing odd numbers.

3.6.3 Feigenbaum Scaling

In the 1970s, Feigenbaum studied the self-similarity of the bifurcation diagram: the entire diagram is contained in small pieces of it! Using just a programmable calculator, he noticed that the bifurcations converge geometrically with the same ratio for different maps with quadratic maxima [3].

Feigenbaum discovered two universal numbers to quantify this convergence.

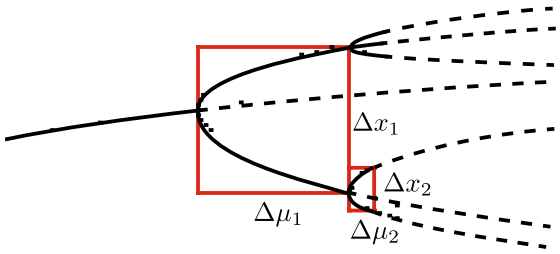

Figure 3.7: Scaling of first two quadratic map bifurcations.

The first describes the frequency of the parameter convergence

$$\delta \equiv \lim_{n\to\infty} \frac{\Delta\mu_n}{\Delta\mu_{n+1}} = 4.669\ldots, \tag{3.24}$$

while the second describes the size branch splittings

$$\alpha \equiv \lim_{n\to\infty} \frac{\Delta x_n}{\Delta x_{n+1}} = 2.5029\ldots, \tag{3.25}$$

as in Fig. 3.7. The first few bifurcations only approximate these limits.

Many real physical systems undergo period-doubling cascades to chaos. Experiments on fluid, electrical, optical, acoustic, and other systems estimate Feigenbaum's δ from the first few bifurcations, and typically agree with the theoretical value to 20% or less. This is astonishing, given the complexity of these systems and the simplicity of 1D maps. Somehow these diverse physical systems share common geometries in the abstract phase spaces of their dynamics.

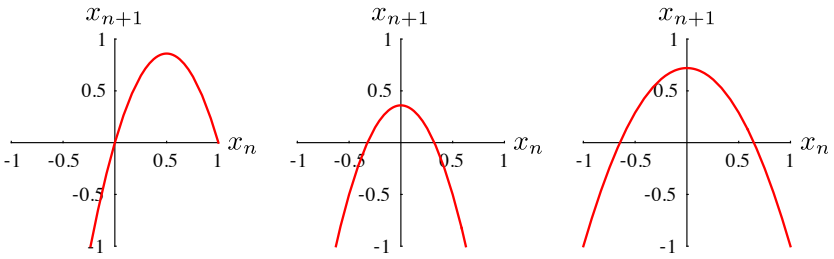

Figure 3.8: Successive translation and dilation of the logistics map.

3.6.4 Renormalization

To understand Feigenbaum scaling, first understand map scaling, as in Fig, 3.8. Translate the logistics map $x_{n+1} = f[x_n]$ (left) by 1/2 by writing $x_{n+1} = f[x_n +$

$1/2] - 1/2$ (middle). Dilate the translated map by 2 by writing $x_{n+1} = 2f[x_n/2]$ (right). Note the combination of direct and inverse operations (addition and subtraction, multiplication and division).

Estimate Feigenbaum's α using a **renormalization** technique. (Estimating δ is similar but more difficult.) Renormalization techniques rely on size scaling, or similarity under magnification. Such methods are very important in the theory of **phase transitions** and **quantum field theory**.

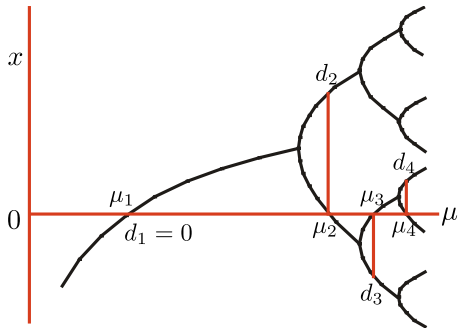

Figure 3.9: Schematic bifurcation diagram and first few super stable cycles.

Since α is the same for all unimodal maps with quadratic maxima (as experience shows), consider a generic map $f_\mu[x]$ centered about the origin, so that $f'_\mu[0] = 0$. Focus on the **superstable** 2^n-cycles at μ_n, as in Fig. 3.9. The distances d_n from the origin to the next nearest iterate of the cycle converge to α.

Next consider the return maps for the first few super stable cycles. Notice how the maps $f^{2^{n-1}}_{\mu_n}$ are similarly parabolic near the origin, as in Fig. 3.10. Express this shrink-flip self-similarity algebraically with the scaling relation

$$f_{\mu_1}[x] \sim -\alpha f^2_{\mu_2}[-x/\alpha] \tag{3.26}$$

and

$$f^2_{\mu_2}[x] \sim -\alpha f^4_{\mu_3}[-x/\alpha] \tag{3.27}$$

and

$$f^4_{\mu_3}[x] \sim -\alpha f^8_{\mu_4}[-x/\alpha] \tag{3.28}$$

and more generally

$$\begin{aligned} f^{2^{n-1}}_{\mu_n}[x] &\sim -\alpha f^{2^n}_{\mu_{n+1}}[-x/\alpha] \\ &= -\alpha f^{2^{n-1}}_{\mu_{n+1}}\left[f^{2^{n-1}}_{\mu_{n+1}}[-x/\alpha]\right], \end{aligned} \tag{3.29}$$

where $\alpha > 1$. In the limit as $n \to \infty$, $\mu_n \sim \mu_{n+1} \to \mu_\infty$ and these scaling relations converge to

$$g[x] = -\alpha g\big[g[-x/\alpha]\big], \tag{3.30}$$

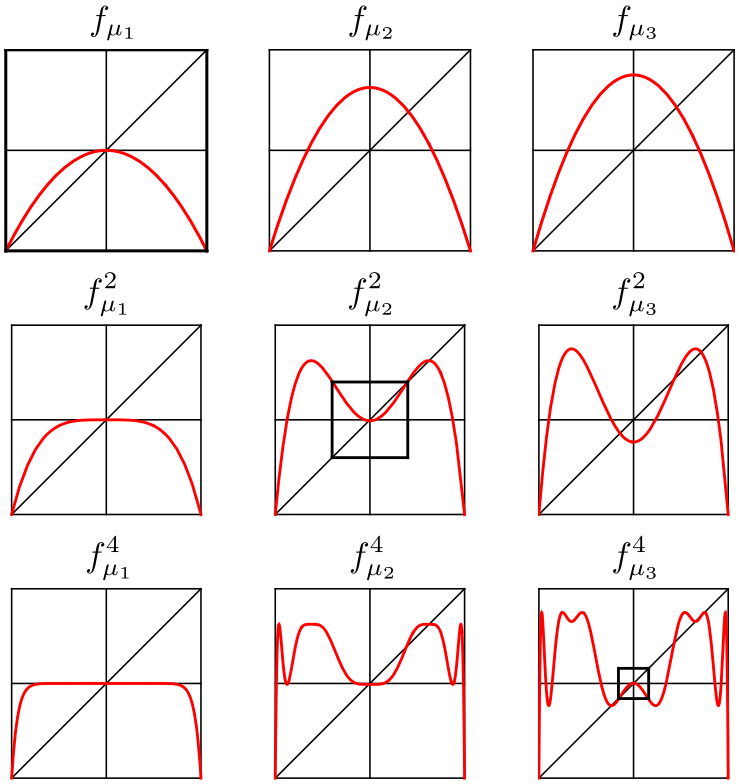

Figure 3.10: The curves inside the thick black boxes are similar, thereby facilitating renormalization.

where $g[x] \equiv \lim_{n\to\infty} f^{2^{n-1}}_{\mu_n}[x]$ is a universal function depending only upon the details of the map $f_\mu[x]$ near the origin.

Solve this **functional equation** simultaneously for the function g and the scaling factor α; the function g is itself an unknown! Evidently, $g[x]$ is parabolic near the origin but infinitely wiggly elsewhere. It is **symmetric** $g[-x] = g[x]$ and may be **normalized** by scaling to $g[0] = 1$. Seek a power series solution of the form

$$g[x] = 1 - kx^2 + \mathcal{O}[x^4] \tag{3.31}$$

for $x \ll 1$. Into Eq. 3.30, substitute, expand, and discard terms of $\mathcal{O}[x^4]$ and higher to find

$$1 - kx^2 \sim -\alpha\left(1 - k\left(1 - \frac{kx^2}{\alpha^2}\right)^2\right) \sim (k-1)\alpha - \frac{2k^2}{\alpha}x^2. \tag{3.32}$$

Equate x^n coefficients

$$1 = (k-1)\alpha, \tag{3.33a}$$

$$-k = -\frac{2k^2}{\alpha} \tag{3.33b}$$

to find

$$k = \frac{\alpha}{2} \tag{3.34}$$

and

$$\alpha^2 - 2\alpha - 2 = 0, \tag{3.35}$$

so

$$1 < \alpha = 1 + \sqrt{3} \approx 2.73, \tag{3.36a}$$

$$k = \frac{1+\sqrt{3}}{2} \approx 1.37. \tag{3.36b}$$

Retaining more terms improves the scaling factor estimate to $\alpha = 2.5029\ldots$.

3.7 Nonquadratic Maps

Not all unimodal maps have quadratic maxima. In fact, consider the map resulting from the function

$$f_{\mu\sigma} = \mu - \sigma e^{-1/|x|}. \tag{3.37}$$

This map is much flatter at $x = 0$ then the quadratic map: not only does its first derivative vanish there, *all* of its derivatives vanish there! Consequently, its bifurcation diagram is qualitatively different, as in Fig. 3.11.

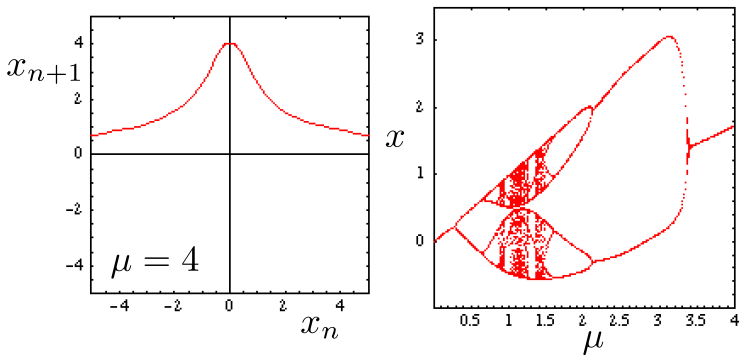

Figure 3.11: "Flat" unimodal map (left) and its bifurcation diagram (right) for $\sigma = 4$.

Problems

1. **Real Mandelbrot Map.** Use Mathematica to analyze the map

$$x_{n+1} = x_n^2 + C. \tag{3.38}$$

   Include sample time series, cobweb constructions, periodic points and stability analyses for the first few bifurcations, and estimates of Feigenbaum's α and δ.

2. **Sine Map.** Use Mathematica to analyze the map

$$x_{n+1} = r \sin[\pi x_n] \tag{3.39}$$

   for $0 \le x_n \le 1$. Include sample time series, cobweb constructions, periodic points and stability analyses for the first few bifurcations, and estimates of Feigenbaum's α and δ. What happens on different intervals, like $-1 \le x_n \le 1$?

3. **Tent Map.** Use Mathematica to analyze the map

$$x_{n+1} = \left\{ \begin{array}{ll} Ax_n, & 0 \le x_n \le 1/2 \\ A(1-x_n), & 1/2 \le x_n \le 1 \end{array} \right\}. \tag{3.40}$$

   Include sample time series, cobweb constructions, periodic points and stability analyses for the first few bifurcations, and estimates of Feigenbaum's α and δ (if they exist).

4. **Feigenbaum α.** Improve the Eq. 3.36a Feigenbaum α estimate by retaining more terms in the power series solution to the renormalization functional equation.

Chapter 4

2D Maps

Consider two ways to generalize the quadratic map from 1D to 2D. Mathematician Benoit Mandelbrot and astrophysicist Michel Hénon first studied these generalizations in the 1960s and 1970s.

4.1 Mandelbrot Map

Consider making the quadratic map complex. Namely,

$$z \leftarrow z^2 + \mu \tag{4.1}$$

or

$$z_{n+1} = z_n^2 + \mu \equiv f[z_n], \tag{4.2}$$

where $z = x + iy$ and μ are complex numbers. Decompose this map into real and imaginary parts to obtain the real 2D map

$$x_{n+1} = x_n^2 + y_n^2 + \operatorname{Re}\mu \equiv f_x[x_n, y_n], \tag{4.3a}$$

$$y_{n+1} = 2x_n y_n + \operatorname{Im}\mu \equiv f_y[x_n, y_n]. \tag{4.3b}$$

Successively applying this **Mandelbrot map** to a unit circle in the complex plane contracts it to fixed point, as in Fig. 4.1, which provide some intuition for its behavior

The first step in analyzing the Mandelbrot map is to look for **fixed points**. Set $z = f[z]$ and find

$$z_\pm = \frac{1 \pm \sqrt{1 - 4\mu}}{2}. \tag{4.4}$$

The next step is to determine the **stability** of the fixed points. In 1D, a fixed point is stable if the magnitude of the derivative of the map at the fixed point is less than unity. In 2D, arrange the four different partial derivatives in the **Jacobian** matrix

$$J = \frac{\partial \vec{f}}{\partial \vec{r}} = \boxed{\begin{matrix} \partial_x f_x & \partial_y f_x \\ \partial_x f_y & \partial_y f_y \end{matrix}} = 2\boxed{\begin{matrix} x & -y \\ y & x \end{matrix}}. \tag{4.5}$$

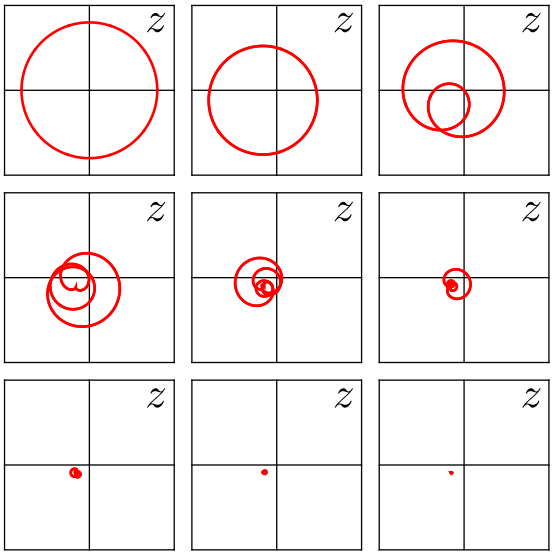

Figure 4.1: For fixed μ, successive Mandelbrot mappings $z \leftarrow z^2 + \mu$ contract the complex unit circle onto a zero-dimensional fixed point.

The absolute value of the determinant of the Jacobian matrix is the ratio of infinitesimal areas after and before the mapping. If this ratio is less than unity, the map is said to be **contracting** or **dissipative**. Since

$$1 > |\det J| = 4x^2 + 4y^2 = 4|z|^2, \tag{4.6}$$

the Mandelbrot map is sometimes contracting, if $|z| < 1/2$, and sometimes expanding, if $|z| > 1/2$, depending upon the location of the iterate in the complex plane.

In 2D, a fixed point is stable if the magnitudes of the **eigenvalues** of the Jacobian matrix, evaluated at the fixed point, are less than unity. The eigenvalues are solutions to $Jz = \lambda z$. Evaluate the characteristic equation $\det[J - \lambda I] = 0$ for λ to find

$$\lambda = 2(x \pm iy) = \left\{ \begin{array}{c} 2z \\ 2z^* \end{array} \right\}. \tag{4.7}$$

For stability of the Eq. 4.4 fixed points $z_\pm$, demand $1 > |\lambda|$, so they lose their stability along the curve defined by $1 = |\lambda| = |2z_\pm| = |2z_\pm^*|$ or

$$e^{i\varphi} = 2z_\pm = 1 \pm \sqrt{1 - 4\mu}. \tag{4.8}$$

Square both sides, solve for μ, and decompose into real and imaginary parts to

obtain

$$\mathrm{Re}\,\mu = \frac{2\cos\varphi - \cos 2\varphi}{4}, \tag{4.9}$$

$$\mathrm{Im}\,\mu = \frac{2\sin\varphi - \sin 2\varphi}{4}, \tag{4.10}$$

which is the parameterized representation of the Fig. 4.2 origin-enclosing cardioids. If the parameter μ lies inside the cardioid, the corresponding fixed point is stable, and iterates of the map will spiral in toward it.

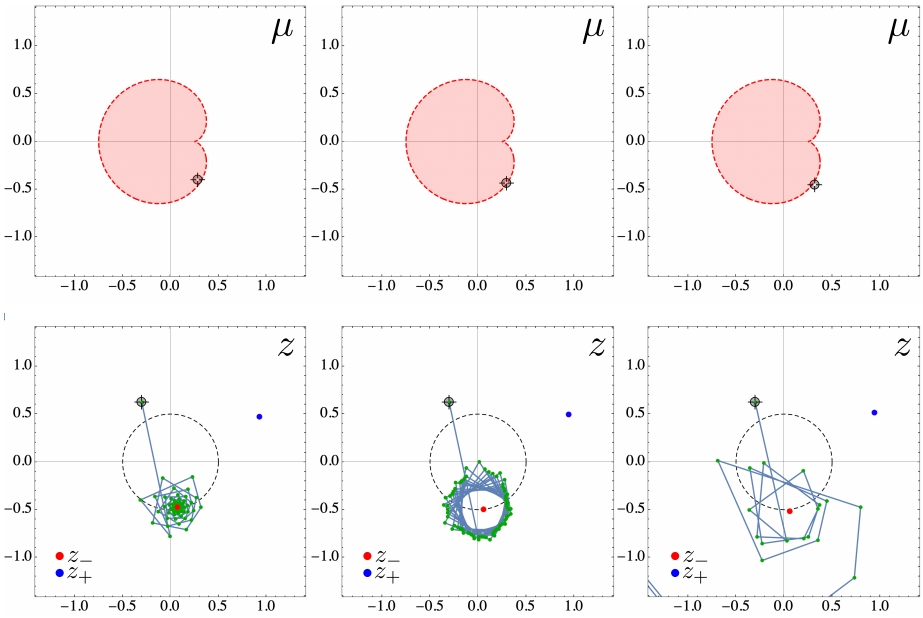

Figure 4.2: Mandelbrot fixed point is stable and orbit (successive iterates) spirals inward to it (top); fixed point is marginally stable and the inward spiral is very slow (middle); fixed point is unstable and orbit spirals outward to infinity.

4.2 Mandelbrot Set

Benoit Mandelbrot studied the complex quadratic map circa 1980 while at I.B.M. using early computer graphics [9]. The beautiful pictures he produced have become a dramatic visual paradigm for nonlinear dynamics (even if their physical relevance is unclear). In particular, he studied the following set. For each point in the complex plane μ, iterate the complex quadratic map starting from the origin. The point μ is in the **Mandelbrot set** if and only if the sequence

$$0 \prec \mu \prec \mu^2 + \mu \prec (\mu^2 + \mu)^2 + \mu \prec ((\mu^2 + \mu)^2 + \mu)^2 + \mu \prec \ldots \tag{4.11}$$

remains bounded. More formally,

$$M = \left\{ \mu : \left| f_\mu^\infty[0] \right| < \infty \right\}. \tag{4.12}$$

The diverging points can be colored or raised according to how quickly they reach infinity, as in Fig. 4.3. (In fact, if the iterates get beyond $|z| = 2$, they will diverge.)

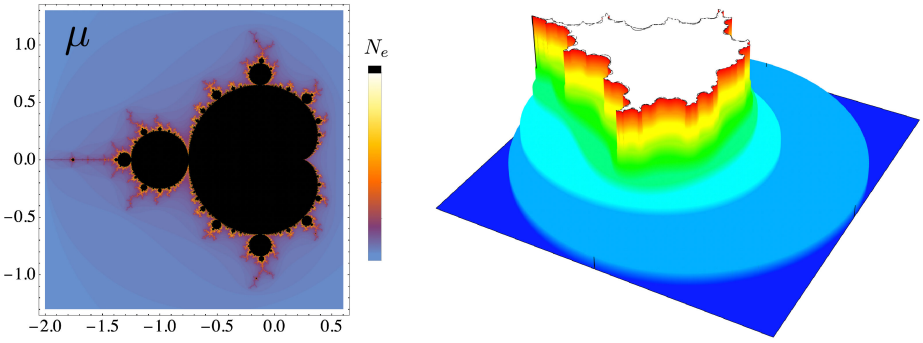

Figure 4.3: Mandelbrot sets where color (left) and height (right) code escape "times" (number of iterates N_e to exceed $|z| = 2$ units from the origin).

The body of the Mandelbrot set is simply the cardioid we calculated above. (Indeed, "mandel brot" means "almond bread" or, with some artistic license, "ginger bread man".) The body corresponds to stable fixed points, or 1-cycles, while the bulbs correspond to different stable n-cycles. Successive bulbs decrease in size geometrically according to the **Feigenbaum scaling** and correspond to bifurcating sequences of orbits.

Mathematicians John Hubbard and Adrien Douady proved [2] that the boundary of the Mandelbrot set is as complicated as it can be: although the boundary has area zero, it has dimension two, and it is completely connected. (An ordinary Euclidean object, like a disk, has a boundary with area zero and dimension one.)

In the 1910s, mathematicians Gaston Julia and Pierre Fatou studied related sets and even without the aid of computer graphics glimpsed some of their complexity. Fix the complex parameter μ, and iterate the complex quadratic map starting from each point z_0 in the complex plane. The point z_0 is in a **Julia set** if and only if the sequence

$$z_0 \prec z_0^2 + \mu \prec (z_0^2 + \mu)^2 + \mu \prec ((z_0^2 + \mu)^2 + \mu)^2 + \mu \prec \ldots \tag{4.13}$$

remains bounded. More formally,

$$J_\mu = \left\{ z_0 : \left| f_\mu^\infty[z_0] \right| < \infty \right\}. \tag{4.14}$$

Connected Julia sets are sometimes referred to as **Julia lace**, and unconnected Julia sets are sometimes referred to as **Fatou dust**. Fatou dust has the in-

teresting property that no two pieces are "together", yet no piece is "alone". Investigate such sets later.

4.3 Generalized Mandelbrot Sets

Interesting generalizations of the Mandelbrot set result by considering maps derived from functions like

$$f_\sigma[z] = z^\sigma + \mu, \tag{4.15}$$

where the exponent σ may be positive or negative, rational or irrational, real or complex. Figure 4.4 is one example.

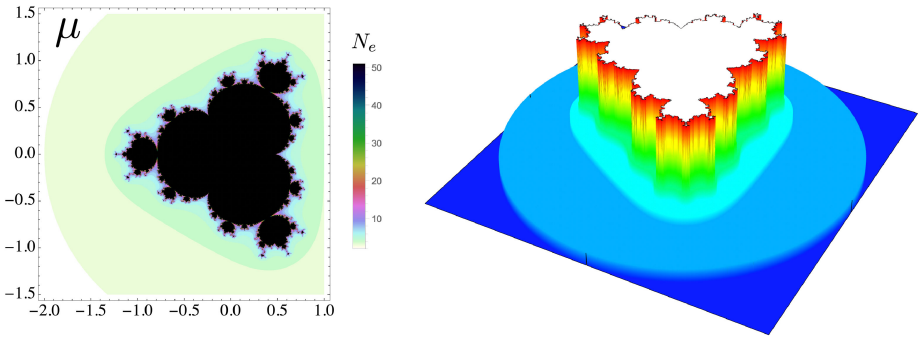

Figure 4.4: Generalized Mandelbrot set with exponent $\sigma = 4$.

4.4 Hénon Map

Consider the 1D map

$$x_{n+1} - bx_{n-1} = 1 - ax_n^2. \tag{4.16}$$

If $b = 0$, then this is equivalent to the logistic map. Otherwise, if $y_n \equiv bx_{n-1}$, it is equivalent to

$$x_{n+1} = 1 + y_n - ax_n^2, \tag{4.17a}$$
$$y_{n+1} = bx_n. \tag{4.17b}$$

This famous 2D map was first studied by theoretical astronomer Michel Hénon [4]. He designed it to incorporate the folding and stretching transformations that mathematician Stephen Smale had demonstrated were at the core of chaotic dynamics. Figure 4.5 illustrates these transformations by successively applying the map to points along a unit circle, for the canonical parameter values $a = 1.4$, $b = 0.3$.

The final or **asymptotic** set is more than a line but less than a plane. It has a self-similar structure that can be assigned a fractional dimension of about

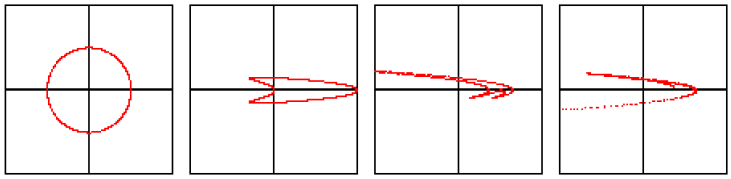

Figure 4.5: Successive mappings fold and stretch a unit circle onto the Hénon "horseshoe".

1.26. Such an asymptotic set is called a **strange attractor**. The self-similar "1-2-3" structure is preserved at all magnifications, as illustrated in Fig. 4.6.

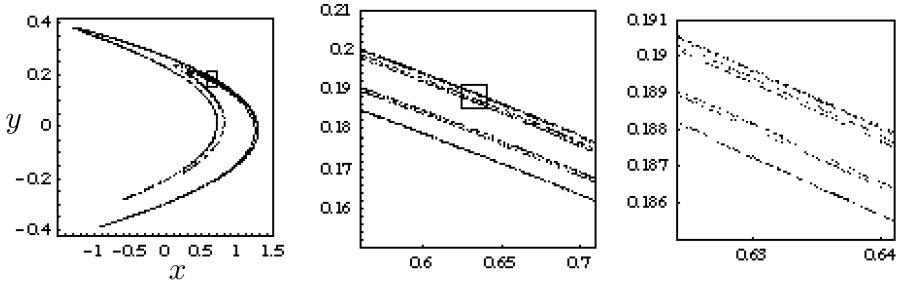

Figure 4.6: Hénon self-similar structure is preserved at all magnifications.

Furthermore, orbits on the attractor exhibit extreme sensitivity to initial conditions, with nearby points diverging exponentially, a necessary condition for chaos. For example, starting with two points, initially very close together, say $\{0.5, 0.2)\}$ and $\{0.5001, 0.2)\}$, after just 25 iterations of the Hénon mapping the points are as far apart as they can be and still be on the attractor, as in Fig. 4.7.

To compare with the Mandelbrot map, note that the fixed points of the Hénon map are

$$x_\pm = \frac{b - 1 \pm \sqrt{(b-1)^2 + 4a}}{2a}, \tag{4.18a}$$

$$y_\pm = bx_\pm. \tag{4.18b}$$

The Jacobian matrix of partial derivatives

$$J = \frac{\partial \vec{f}}{\partial \vec{r}} = \boxed{\begin{matrix} \partial_x f_x & \partial_y f_x \\ \partial_x f_y & \partial_y f_y \end{matrix}} = \boxed{\begin{matrix} -2ax & 1 \\ b & x \end{matrix}}. \tag{4.19}$$

The absolute value of the determinant of the Jacobian matrix

$$1 > |\det J| = |-b| = |b|. \tag{4.20}$$

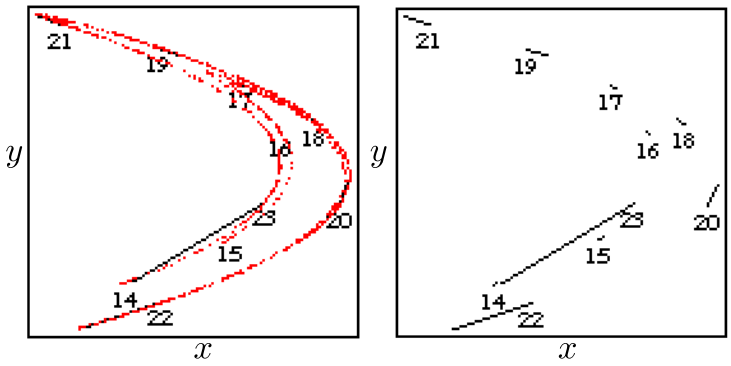

Figure 4.7: Hénon divergence of nearby orbits, with and without the attractor.

Thus, the Hénon map is always contracting if $|b| < 1$, as it is for the canonical parameter values $a = 1.4$, $b = 0.3$.

Examine the eigenvalues of the Jacobian to find that the fixed point $\{x_+, y_+\}$ is unstable for $a > 3(b-1)^2/4$, while the fixed point $\{x_-, y_-\}$ is always unstable. If $b = 0.3$ is fixed and a varies from 0 to 1.4, the map undergoes a **periodic-doubling cascade** to chaos.

Problems

1. **Julia Sets.** Use Mathematica to create and explore the Eq. 4.13 Julia sets.

2. **Standard Map.** Use Mathematica to explore the Chirikov standard map

$$\theta_{n+1} = \theta_n + p_{n+1}, \tag{4.21a}$$
$$p_{n+1} = p_n + K \sin\theta_n, \tag{4.21b}$$

   where θ_n and p_n are modulo 2π. The map models a kicked rotator at angle θ with momentum p. Unlike the Hénon map, which is **area contracting**, the standard map is **area preserving**. It generates periodic *and* chaotic orbits for different initial conditions $\{\theta, p\}$ at *the same* parameter K. (Hint: Create a ListPlot of a NestList of a compiled vector $\{\theta, p\}$ variation of Eq. 4.21 Mod 2π.)

Chapter 5

Nonlinear Pendulum

The linear (small angle) pendulum is a canonical example of introductory physics and makes possible time-keeping, while the nonlinear (large angle) is a paradigm of nonlinear dynamics.

5.1 Flows

Flows are defined by **differential equations** like

$$\frac{d\vec{x}}{dt} = \dot{\vec{x}} = \vec{f}[\vec{x}]. \tag{5.1}$$

The **dimension** of the flow is the dimension of the vector $\vec{x}$ An important source of flows are the **Newtonian**, **Lagrangian**, and **Hamiltonian** formulations of classical mechanics. Introduce tools for the analysis of flows by first examining in detail the case of the **nonlinear pendulum**.

5.2 Classical Analysis

5.2.1 Small Angles

Consider a simple pendulum of mass m suspended from a massless rod of length ℓ. Let θ be the angle the rod makes with downward, as in Fig. 5.1.

According to **Newton's Second Law**, with respect to the pivot, the torque on the pendulum

$$-\ell mg\sin\theta = \tau = I\alpha = m\ell^2\ddot{\theta} \tag{5.2}$$

so

$$\ddot{\theta} + \frac{g}{\ell}\sin\theta = 0. \tag{5.3}$$

This **nonlinear** differential equation cannot be solved in terms of finite number of common named functions (like polynomials, trigonometrics, exponentials and

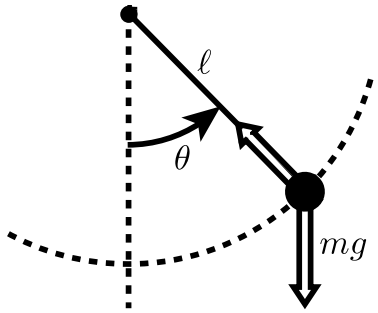

Figure 5.1: Simple pendulum of length ℓ and mass m in a gravity field $\vec{g}$.

logarithms). However, neglecting the nonlinear terms in the sine infinite series

$$\sin\theta = \theta - \frac{\theta^3}{3!} + \frac{\theta^5}{5!} - \frac{\theta^7}{7!} + \cdots \tag{5.4}$$

for small angles $\theta \ll 1$ simplifies the equation to

$$\ddot{\theta} + \frac{g}{\ell}\theta = 0, \tag{5.5}$$

which famously has the sinusoidal solution

$$\theta = \theta_i \sin[\omega t + \varphi_i] \tag{5.6}$$

if the **natural frequency** $\omega_0 = \sqrt{g/\ell}$. The amplitude θ_i and phase shift φ_i depend on the initial angle and angular velocity. For small angles, the frequency and period $T_0 = 2\pi/\omega$ are independent of amplitude, and this makes possible timekeeping by pendulum-based clocks.

5.2.2 Large Angles

Recapitulate the classical analysis of the nonlinear pendulum for large angles beginning with the motion equation

$$\ddot{\theta} + \omega_0^2 \sin\theta = 0. \tag{5.7}$$

Multiply both sides by $\dot{\theta}$ from the right to get

$$0 = \ddot{\theta}\,\dot{\theta} + \omega_0^2 \sin\theta\,\dot{\theta} = \left(\frac{1}{2}\dot{\theta}^2 - \omega_0^2\cos\theta\right)^{\cdot} \tag{5.8}$$

and integrate the product to find the **non-dimensional energy** motion constant

$$\epsilon = \frac{1}{2}\dot{\theta}^2 - \omega_0^2\cos\theta = \text{constant} \equiv -\omega_0^2\cos\theta_m, \tag{5.9}$$

where θ_m is the maximum angular deflection of the pendulum. (At this **turning point**, the angular velocity $\dot{\theta}$ momentarily vanishes.) This differential equation is **separable**. Solve for

$$\frac{d\theta}{dt} = \dot{\theta} = \pm\omega_0\sqrt{2(\cos\theta - \cos\theta_m)} \tag{5.10}$$

where the different signs handle clockwise and counterclockwise rotations. Integrate

$$\omega_0 dt = \frac{1}{\sqrt{2(\cos\theta - \cos\theta_m)}}. \tag{5.11}$$

to find

$$\omega_0 t = \int_0^\theta d\theta' \frac{1}{\sqrt{2(\cos\theta' - \cos\theta_m)}}. \tag{5.12}$$

Use the half-angle formula $\cos\theta = 1 - 2\sin^2[\theta/2]$ to rewrite as

$$\omega_0 t = \frac{1}{2}\int_0^\theta d\theta' \frac{1}{\sqrt{\sin^2[\theta_m/2] - \sin^2[\theta'/2]}}. \tag{5.13}$$

Implicitly define a new angle φ by

$$\sin[\theta/2] = \sin[\theta_m/2]\sin\varphi = k\sin\varphi, \tag{5.14}$$

where $\varphi \in [-\pi, \pi]$ when $\theta \in \{-\theta_m, \theta_m\}$, to get

$$\begin{aligned}\omega_0 t &= \frac{1}{2}\int_0^\varphi \frac{k\cos\varphi'\, d\varphi'}{\cos[\theta'/2]/2}\frac{1}{k\cos\varphi'} \\ &= \int_0^\varphi d\varphi' \frac{1}{\sqrt{1 - k^2\sin^2\varphi'}} \\ &= \mathrm{am}^{-1}[\varphi, k^2],\end{aligned} \tag{5.15}$$

which inverts to the **Jacobi amplitude elliptic function**

$$\varphi = \mathrm{am}[\omega_0 t, k^2]. \tag{5.16}$$

Beginning with Eq. 5.14, solve for

$$\begin{aligned}\theta &= 2\arcsin\left[k\sin\varphi\right] \\ &= 2\arcsin\left[k\sin\left[\mathrm{am}\left[\omega_0 t, k^2\right]\right]\right] \\ &= 2\arcsin\left[\sin\left[\theta_m/2\right]\sin\left[\mathrm{am}\left[\omega_0 t, \sin^2\left[\theta_m/2\right]\right]\right]\right] \\ &= 2\arcsin\left[\sin\left[\theta_m/2\right]\mathrm{sn}\left[\omega_0 t, \sin^2\left[\theta_m/2\right]\right]\right],\end{aligned} \tag{5.17}$$

where the elliptic function $\mathrm{sn}[x, y] = \sin\mathrm{am}[x, y]$. This provides angle versus time when released from rest, $\{\theta[0], \dot{\theta}[0]\} = \{\theta_m, 0\}$. Unfortunately, finding

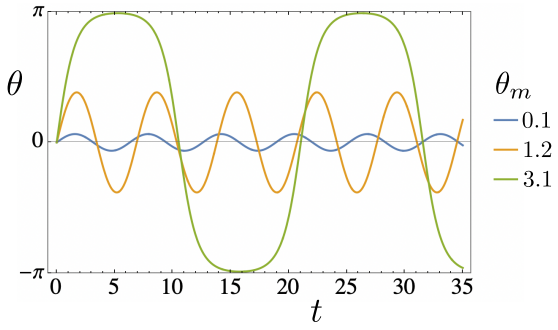

Figure 5.2: Pendulum time series for three different amplitudes.

integration constants for *arbitrary* initial conditions requires solving systems of nonlinear equations, which is not always possible, making numerical techniques sometimes necessary (and desirable). Figure 5.2 plots angle θ versus time t for different maximum angles θ_m.

For small angles, the oscillations are nearly sinusoidal and the pendulum periods are insensitive to amplitude. But for large angles, the oscillations are not sinusoidal and the periods increase with amplitude. From Eq. 5.15, the period

$$\omega_0 T = 4\int_0^{\pi/2} d\varphi \frac{1}{\sqrt{1-k^2\sin^2\varphi}} = 4K[k^2] = 4K\left[\sin^2[\theta_m/2]\right], \tag{5.18}$$

where $K[\bullet]$ is the **complete elliptic integral** of the first kind. Expand the integrand in the power series

$$\frac{1}{\sqrt{1-k^2\sin^2\varphi}} = 1 + \frac{1}{2}k^2\sin^2\varphi + \frac{3}{8}k^4\sin^4\varphi + \frac{5}{16}k^6\sin^6\varphi + \cdots \tag{5.19}$$

and integrate term-by-term to get

$$\frac{\omega_0 T}{2\pi} = 1 + \frac{1}{4}k^2 + \frac{9}{64}k^4 + \frac{25}{256}k^2 + \cdots. \tag{5.20}$$

Substitute $k = \sin[\theta_m/2]$, expand each k term in a θ_m power series, and collect θ_m terms to find

$$\frac{T}{T_0} = 1 + \frac{1}{16}\theta_m^2 + \frac{11}{3072}\theta_m^4 + \frac{173}{737\,280}\theta_m^6 + \cdots. \tag{5.21}$$

Figure 5.3 plots the period versus the maximum angle. The plot diverges near $\theta_m = \pi$ when the pendulum inverts.

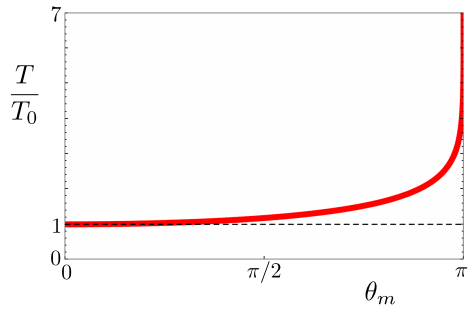

Figure 5.3: Ideal stiff pendulum period diverges as maximum angle $\theta_m \to \pi$ when pendulum inverts.

5.3 Qualitative Analysis

At the end of the nineteenth century, beginning with Henri Poincaré, and continuing throughout the twentieth century, qualitative geometric techniques have become increasingly important in the analysis of dynamical systems. Consider the Eq. 5.9 pendulum nondimensional energy

$$\epsilon = \frac{1}{2}\dot{\theta}^2 + V[\theta] \tag{5.22}$$

in units where $\omega_0^2 = 1$. Assume the potential energy

$$V[\theta] = 1 - \cos\theta \tag{5.23}$$

so that $V[0] = 0$. If the motion is bounded, the intersections of the potential function and the constant energy are the **turning points** of the motion, as in Fig. 5.4.

Write the pendulum second-order differential equation as two first-order differential equations

$$\dot{\omega} = -\sin\theta, \tag{5.24a}$$

$$\dot{\theta} = \omega. \tag{5.24b}$$

This differential system describes a flow in the 2D state space $\{\theta, \omega\}$ of the pendulum. The flow is like that of an **incompressible fluid**; curves of constant energy never cross and state space areas are preserved. Fixed points of the flow are the stable and unstable (inverted) equilibrium configurations of the pendulum. Near the stable points, the flow is **elliptical**. Near the unstable points, the flow is **hyperbolic**. The elliptic and hyperbolic points alternate in the common pattern $\circ \times \circ \times \circ$.

The Fig. 5.4 blue curves correspond to **libration** of the pendulum back-and-forth through small angles, bounded closed orbits of low energy. The Fig. 5.4

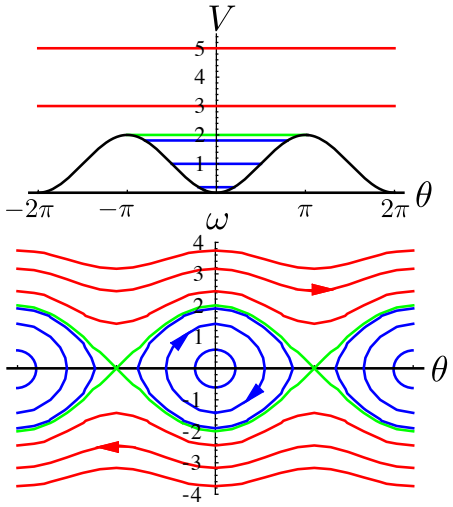

Figure 5.4: Pendulum potential energy (top) and state space (bottom). Flows include rotation (red), libration (blue), and separatrix (green).

red curves correspond to **rotation** of the pendulum end-over-end, unbounded open orbits of high energy.

Addition of a viscous torque $\tau = -\gamma\omega$ damps the motion of the pendulum and dramatically changes its state space flow, as in Fig. 5.5. State space volumes now decrease to zero as orbits spiral in to the stable fixed points, 0D **attractors** of the 2D states space. In higher dimensions, the inclusion of dissipation can produce **strange attractors** of fractional dimension.

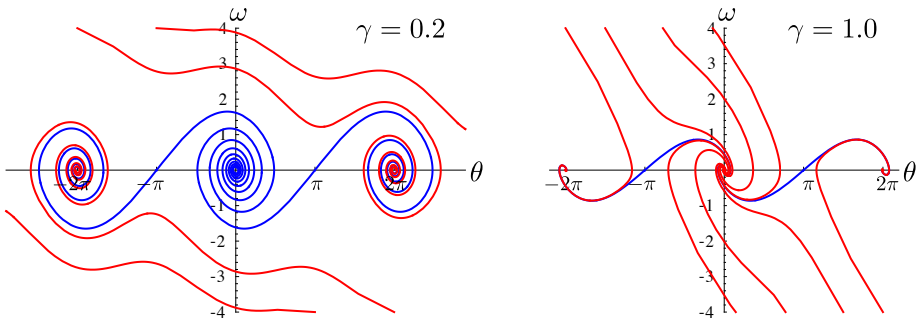

Figure 5.5: Pendulum state space flow with small (left) and large (right) viscosity.

5.4 Numerical Analysis

Most differential systems cannot be integrated exactly in terms of a finite number of elementary functions. Consequently, numerical methods are vital to the modern study of dynamical systems. Indeed, it is the widespread availability of fast and cheap computers that fueled the revolution in nonlinear dynamics.

Furthermore, the real content of **Newton's Second Law** is arguably an **algorithm** for evolving a dynamical system forward in time. For example, **Euler-Cromer** (or semi-implicit Euler) integration [1] of Newton's second law

$$F_x = ma_x = m\ddot{x} \tag{5.25}$$

is equivalent to the algorithm

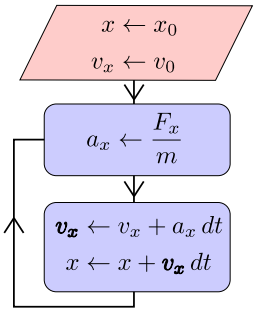

(5.26)

provided the **time step** dt is sufficiently small. Given an initial condition $\{x_0, v_0\}$, use this simple **first-order Runge-Kutta** technique to evolve the system forward in time. Each time step makes an error $\mathcal{O}[dt^2]$, so eventually the calculated orbit may diverge significantly from the true orbit. Many more accurate – and complicated – algorithms are available, but the Euler-Crmer algorithm is simple and for bounded orbits is stable. (The key to the stability, as Cromer noted, is to update the velocity *before* the position.)

5.5 Forced Damped

Much of the phenomena and many of the techniques of nonlinear dynamics can be related to a sinusoidally forced damped pendulum described by

$$\ddot{\theta} = -\sin\theta - \gamma\dot{\theta} + A\cos[2\pi t/T + \delta]. \tag{5.27}$$

The dynamics of the unforced pendulum generates 2D flows in the $\{\theta, \omega\}$ state space, but forcing adds another dimension. Figure 5.6 graphically summarizes its behavior by "strobing" the motion once each forcing period to create a **Poincaré** section of the 3D flow. The forced undamped pendulum exhibits **conservative chaos** while the forced damped pendulum exhibits **dissipative chaos**.

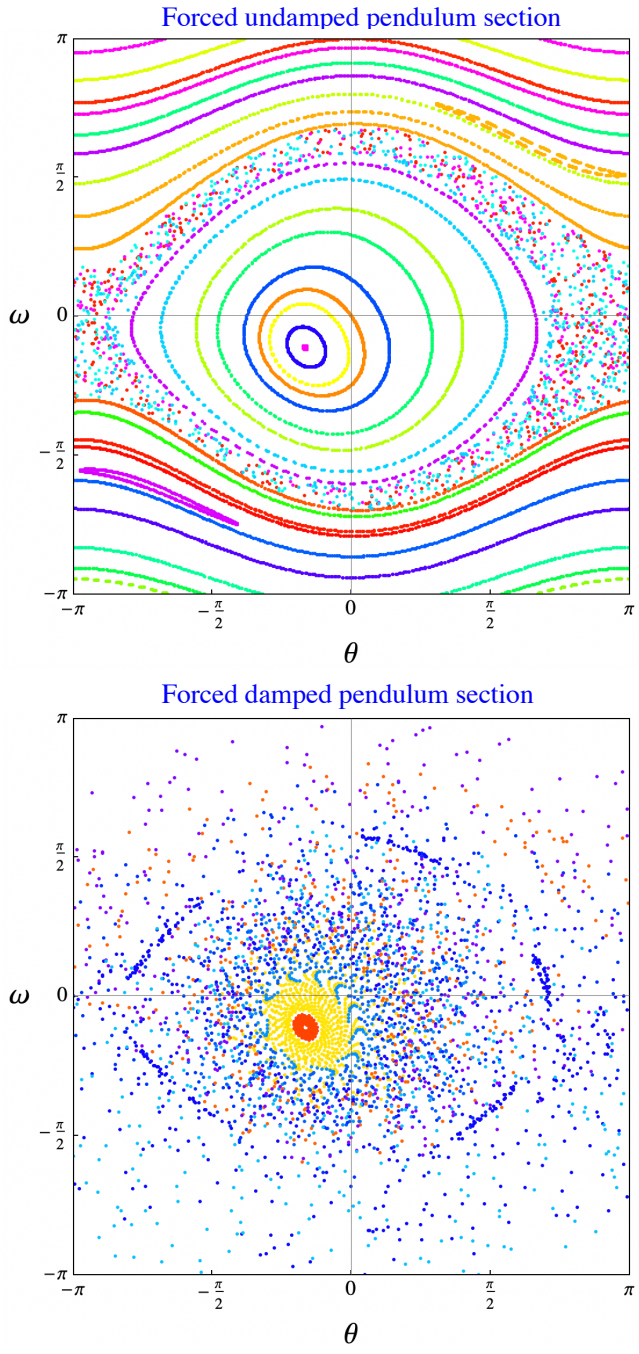

Figure 5.6: Pendulum state space sections: undamped sinusoidally forced (top) and damped sinusoidally forced (bottom) strobed once per forcing period. Location of fixed point (red) rotates about the origin with the phase shift δ of the forcing.

Problems

1. **Pendulum Correction.** Consider a nonlinear pendulum released from rest at an angle θ_m. Use Mathematica to provide the intermediate steps to the Eq. 5.21 derivation of its period T, and extend the series to higher orders. Overlay plots $\{\theta_m, T\}$ with different numbers of series terms, and check for convergence.

2. **Custom Function.** Inspired by the Jacobi and Elliptic special functions of the nonlinear pendulum problem, create your own function! For example, invent a second-order nonlinear differential equation, unusual enough that prior use is unlikely, and numerically study its solutions as you vary the initial conditions. Name your function and choose a symbol for it.

Chapter 6

1D Flows

Even the simplest nonlinear differential equations often cannot be solved in terms of a finite number of elementary functions. However, qualitative techniques can unveil their behavior.

6.1 Fixed Points

Flows on a line are governed by differential equations of the form

$$\dot{x} = f[x]. \tag{6.1}$$

Flows are controlled by **fixed points**, also called **equilibria** or **stationary states**. In 1D, fixed points $f[x] = 0$ correspond to vanishing velocities $\dot{x} = 0$, which divide space into noninteracting regions. Classify the fixed points according to their stability. A sufficient condition that the fixed point x_* is **stable** is the derivative $\lambda \equiv f'[x_*] < 0$. Such points are also called **sinks**, **attractors**, or **nodes**. A sufficient condition that the fixed point is **unstable** is $\lambda > 0$. Such points are also called **sources** or **repellors**. These generic cases are indicated in the Fig. 6.1 velocity field diagrams, along with special cases where $\lambda = 0$. Such nongeneric cases require the coincidence that both $f[x]$ and its derivative vanish simultaneously. They are **structurally unstable** because such coincidence can typically be destroyed by small parameter changes. Structurally unstable fixed points are not observed experimentally because of noise and uncertainty. However, such points can still demarcate different classes of system behavior.

6.2 Lyapunov Exponent

Analyze the flow about a fixed point x_* by expanding $f[x] = 0$ in a power series

$$f[x] = f[x_*] + (x - x_*)f'[x_*] + \cdots . \tag{6.2}$$

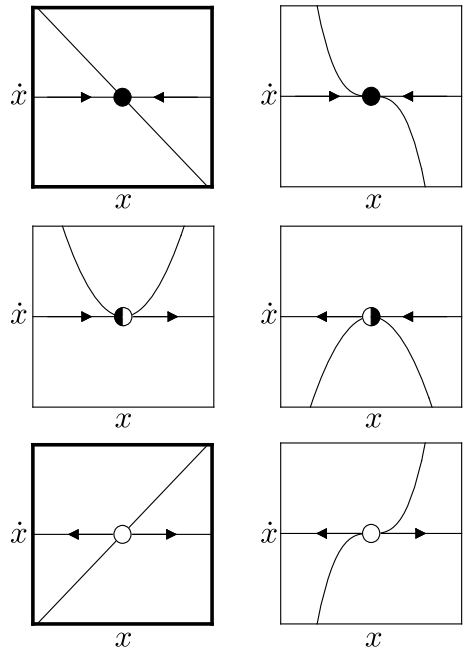

Figure 6.1: Velocity fields near stable (top), bistable (middle), and unstable (bottom) fixed points. Black circles represent stability and white circles represent unstabilty.

Nearby x_* write

$$\frac{d}{dt}(x - x_*) = f[x] - f[x_*] \sim (x - x_*)\lambda, \tag{6.3}$$

where $\lambda = f'[x_*]$ is the slope of the velocity curve. Thus

$$\frac{d}{dt}\delta x \sim \delta x\, \lambda, \tag{6.4}$$

where $\delta x = x - x_*$. Solve to find

$$\delta x = \delta x_0 e^{\lambda t} = \delta x_0 e^{t/\tau}. \tag{6.5}$$

If $\lambda < 0$, then the trajectory is exponentially attracted to the stable fixed point. If $\lambda > 0$, then the trajectory is exponentially repelled from the stable fixed point. λ is the fixed-point's **Lyapunov exponent**, and $\tau = 1/\lambda$ is its **e-folding** time. If the exponential base is 2 and the time t is in seconds, then the Lyapunov exponent is in bits-per-second.

If $\lambda = 0$, higher-order terms in the power series indicate a nonexponential or "critically slow" motion near the fixed point.

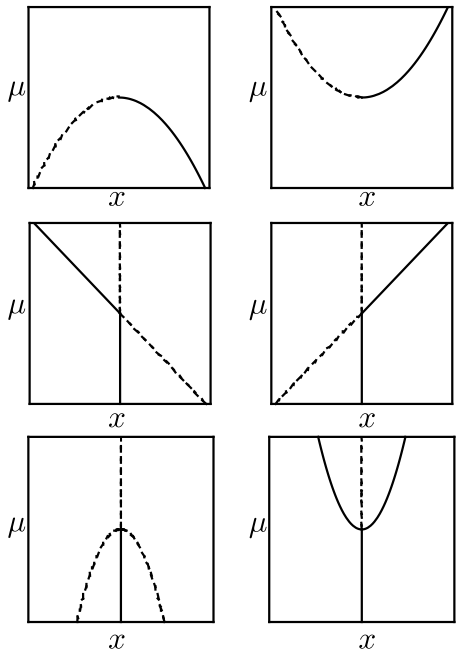

Figure 6.2: Limit point (top), transcritical (middle), and pitchfork (bottom) bifurcations. Solid lines represent stability and dashed lines represent unstability.

6.3 Bifurcations

6.3.1 Overview

Bifurcations provide models for the transitions of 1D flows $\dot{x} = f_\mu[x]$ as a control parameter μ varies. A bifurcation occurs when the fixed point structure undergoes a qualitative **topological** change as a parameter μ varies. The three classes of bifurcations we will consider are illustrated by Fig. 6.2. Solid lines denote stable fixed points while dashed lines denote unstable fixed points.

6.3.2 Limit Point

Limit point bifurcations are the basic mechanism by which fixed points are created and destroyed. The prototypical example or **normal form** of a limit point bifurcation is

$$\dot{x} = \mu - x^2. \tag{6.6}$$

This is the simplest differential equation that exhibits the bifurcation. Figure 6.3 sketches the velocity field for negative, zero, and positive parameter μ. The velocity function is the inverted parabola $\mu - x^2 = f_\mu[x]$. Geometrically, for $\mu < 0$, the inverted parabola does not intersect the x axis, and no fixed points

exist. For for $\mu > 0$, the inverted parabola intersects the x axis (and the velocity $\dot{x}$ vanishes) in two places $x \pm \sqrt{\mu}$, and two fixed points exist, one unstable and the other stable. For $\mu = 0$ only, the inverted parabola is tangent to the x axis, and an isolated bistable point exists. Increasing μ through zero from negative to positive creates a pair of fixed points of opposite stability.

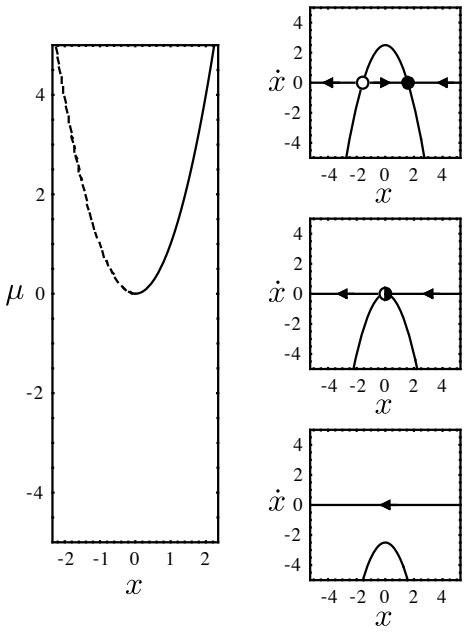

Figure 6.3: Pair creation limit point bifurcation (left); corresponding velocity fields (right). Solid lines and black circles represent stability, while dashed lines and white circles represent unstability.

A couple of different strategies for classifying fixed points exist. One technique is to inspect the slope of the velocity curve $f_\mu[x]$ at the fixed point; positive slope means positive Lyapunov exponent, which means exponential repulsion from an unstable point; negative slope means negative Lyapunov exponent, which means exponential attraction to a stable point. Of course, this test fails if the slope vanishes. However, another technique is to sketch the velocity field on either side of a fixed point to determine its stability. Note how the velocities flip-flop crossing a stable or unstable point.

A complementary normal form is

$$\dot{x} = \mu + x^2. \tag{6.7}$$

Note the sign change. Figure 6.4 sketches the velocity field for negative, zero, and positive parameter μ. The velocity function is the upright parabola $\mu + x^2 = f_\mu[x]$. Geometrically, for $\mu > 0$ the upright parabola does not intersect the $\dot{x}$

axis, and no fixed points exist. For $\mu < 0$, the upright parabola intersects the x axis in two places $x = \pm\sqrt{\mu}$, and two fixed points exist, one stable and the other unstable. For $\mu = 0$ only, the upright parabola is tangent to the x axis, and an isolated bistable point exists. Increasing μ through zero from negative to positive, annihilates a pair of fixed points of opposite stability.

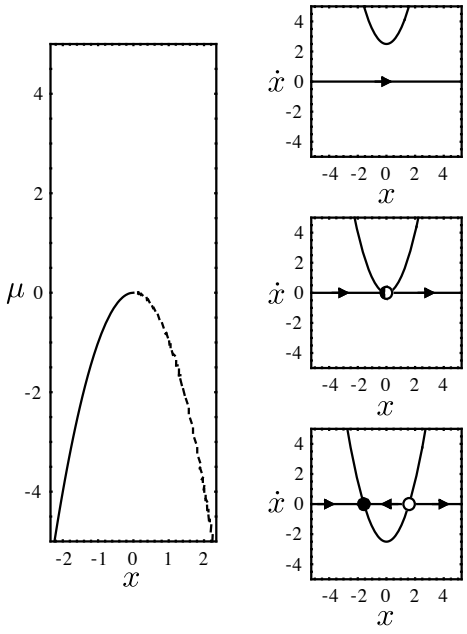

Figure 6.4: Pair annihilation limit point bifurcation (left); corresponding velocity fields (right). Solid lines and black circles represent stability, while dashed lines and white circles represent unstability.

6.3.3 Transcritical

Transcritical bifurcations illustrate an exchange of stabilities between fixed points as a parameter varies. The normal form is

$$\dot{x} = \mu x - x^2. \tag{6.8}$$

Note the extra x factor. Figure 6.5(left) sketches the velocity field for negative, zero, and positive parameter μ. The velocity function is the inverted shifted parabola $\mu x - x^2 = f_\mu[x]$. Geometrically, for $\mu < 0$, the parabola intersects the x axis in two places, $x < 0$ and $x = 0$, and a pair of fixed points exists, one unstable and the other stable. For $\mu > 0$, the parabola intersects the x axis in two places $x = 0$ and $x > 0$, and a pair of fixed points exists, one unstable and the other stable. Increasing μ through zero from negative to positive, exchanges the stability of these two fixed points.

A complementary normal form is

$$\dot{x} = \mu x + x^2. \tag{6.9}$$

Note the sign x change. Figure 6.5(right) sketches the velocity field for negative, zero, and positive parameter μ. The velocity function is the inverted shifted parabola $\mu x + x^2 = f_\mu[x]$. Geometrically, this is the inverse of the previous bifurcation.

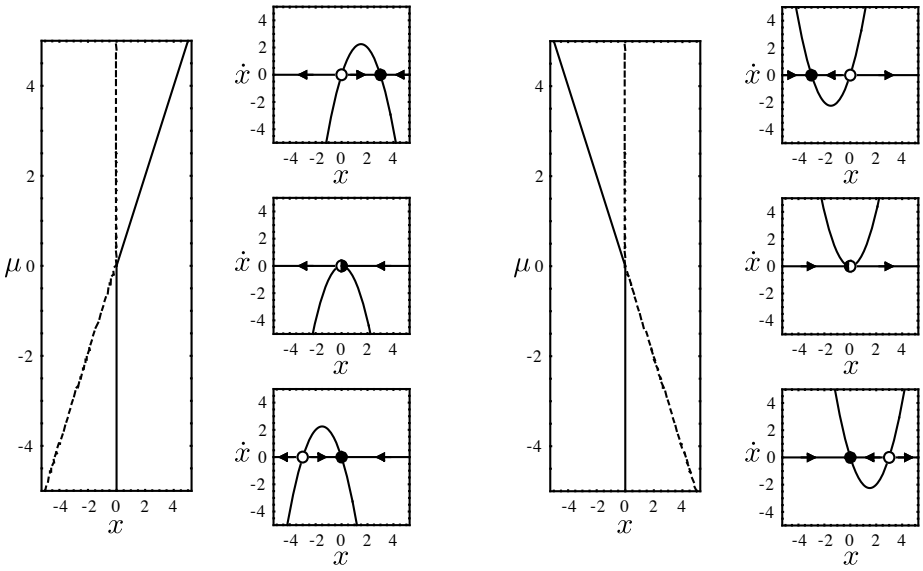

Figure 6.5: Complementary transcritical bifurcations and corresponding velocity fields.

6.3.4 Pitchfork

Pitchfork bifurcations are common in physical problems involving (for example) spatial symmetry. Two distinct types exist. The **supercritical pitchfork** bifurcation normal form is

$$\dot{x} = \mu x - x^3. \tag{6.10}$$

Note the cubic term. This equation is symmetric under parity inversion, $+x \to -x$. (Try it.) Figure 6.6(left) sketches the velocity field for negative, zero, and positive parameter μ. The velocity function is the cubic polynomial $\mu x - x^3 = f_\mu[x]$. For $\mu < 0$, the cubic intersects the x axis only at $x = 0$, a stable fixed point. For $\mu = 0$, the cubic intersects the x axis in three places, $x = 0$ and $x = \pm\sqrt{\mu}$, a pair of stable fixed points separated by a single unstable fixed point. Increasing mu through zero from negative to positive unstabilizes the origin and

simultaneously a pair of stable fixed points are born at small amplitudes. In the engineering literature, this is known as a **subtle** or **soft** or **safe** bifurcation.

A subcritical pitchfork bifurcation is described by the complementary normal form

$$\dot{x} = \mu x + x^3. \tag{6.11}$$

Note the sign change. Figure 6.6(right) sketches the velocity field for negative, zero, and positive parameter μ. The velocity function is the cubic polynomial $\mu x + x^3 = f_\mu[x]$. For $\mu < 0$, the cubic intersects the x axis in three places, $x = 0$ and $x = \pm\sqrt{-\mu}$, a pair of unstable fixed points separated by a single stable fixed point. For $\mu > 0$, the cubic intersects the x axis only at $x = 0$, an unstable fixed point. Increasing μ through zero from negative to positive unstablizes the origin and simultaneously a pair of stable fixed points annihilates. In the engineering literature, this is known as a **catastrophic** or **hard** or **dangerous** bifurcation.

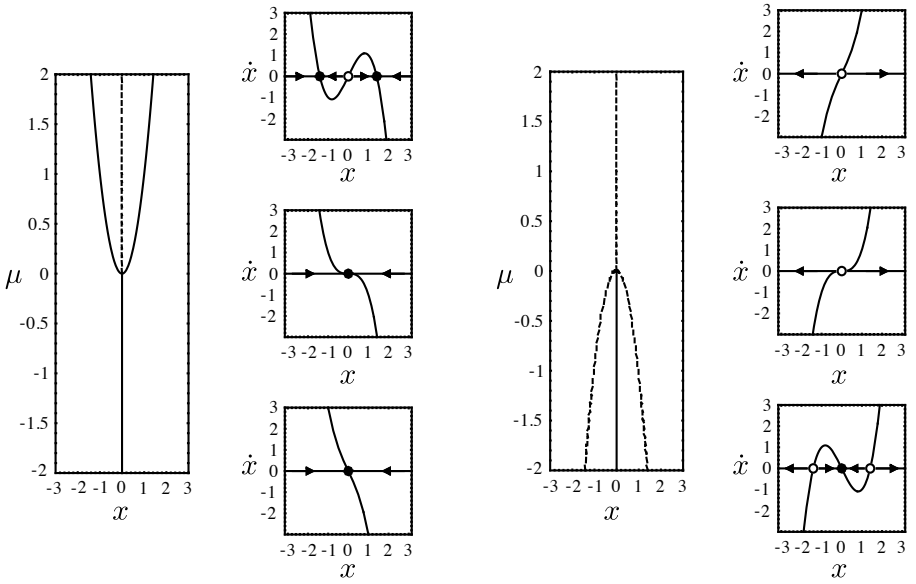

Figure 6.6: Complementary pitchfork bifurcations and corresponding velocity fields.

6.3.5 Broken Pitchfork

Pitchfork bifurcations are **structurally unstable**. The addition of the constant λ to a pitchfork normal form

$$\dot{x} = \lambda + \mu x + x^3 \tag{6.12}$$

disconnects the pitchfork bifurcation, as in Fig. 6.7. If $\lambda < 0$, then increasing μ through 0 induces a smooth evolution from the symmetric $x = 0$ state to the

negative asymmetric $x < 0$ state; the disconnected positive asymmetric $x > 0$ state can only be reached by a discontinuous jump. Positive $\lambda > 0$ favors the positive asymmetric state.

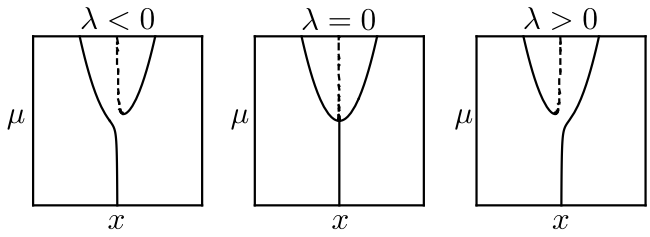

Figure 6.7: Pitchfork bifurcations symmetry-breaking imperfections.

The buckling of an elastic beam is a good physical example. Balance a stack of books on a vertical plastic ruler. If the load is not too great, then the ruler remains straight. However, add too many books and the load exceeds a critical value beyond which the ruler bends left or right. While ideal rulers may exhibit pitchfork bifurcations, real rulers always have a preferred bending direction, even at small loads, which break the symmetry of the pitchfork.

6.3.6 Hysteresis

As an example of a higher-order 1D flow, incorporating both a pitchfork bifurcation and two limit point bifurcations, that illustrates the phenomenon of **hysteresis**, consider the normal form

$$\dot{x} = \mu x + x^3 - x^5 = f_\mu[x]. \tag{6.13}$$

Note the quintic term. The velocity function $f_\mu[x]$ is a quintic polynomial that factors into

$$\begin{aligned} f_\mu[x] = x &\left(x - \sqrt{\frac{1-\sqrt{1+4\mu}}{2}}\right)\left(x - \sqrt{\frac{1+\sqrt{1+4\mu}}{2}}\right) \\ &\left(x + \sqrt{\frac{1-\sqrt{1+4\mu}}{2}}\right)\left(x + \sqrt{\frac{1+\sqrt{1+4\mu}}{2}}\right). \end{aligned} \tag{6.14}$$

Clearly, $\mu = 0$ and $\mu = -1/4$ are important values. Figure 6.8(left) carefully sketches the quintic between these values. With a little more analysis, the global behavior emerges. For $\mu < -1/4$, a single stable fixed point at the origin exists. For $-1/4 < \mu < 0$, in addition two pairs of stable and two pairs of unstable fixed points exist – five fixed points altogether, the maximum the quintic can provide. For $0 < \mu$, one pair of stable fixed points separated by one unstable fixed point at the origin exists. At $\mu = -1/4$, limit point bifurcations create two pairs of stable and unstable fixed points. At $\mu = 0$, a subcritical pitchfork

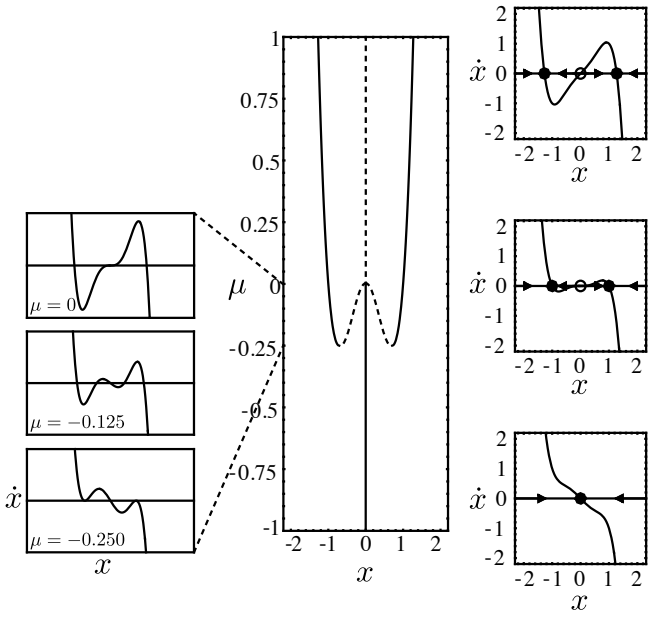

Figure 6.8: A subcritical pitchfork with two creation limit point bifurcations.

bifurcation absorbs the unstable fixed points and exchanges the stability of the origin.

Consider the following scenario, as Fig. 6.9. At $\mu = 0$, place the system in the negative stable branch. Gradually decrease μ to $-1/4$, where this stable branch disappears, forcing the system to jump to the sole remaining stable fixed point at the origin. Now, gradually increase μ back to 0, where this stable branch disappears, forcing the system to jump back to the negative (or positive) stable branch. The system has gone through a **hysteresis** cycle.

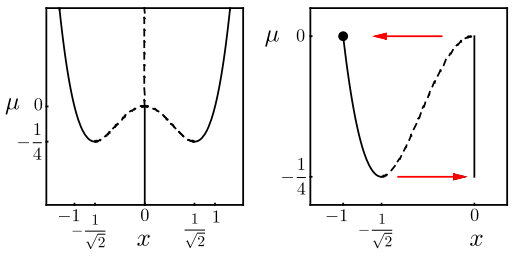

Figure 6.9: Bifurcation diagram (left) and hysteresis cycle close-up (right).

6.4 Bead on Hoop Example

Apply these techniques to a real system. A famous physical example is the motion of an overdamped bead sliding on a rotating hoop. Let the bead have mass m and the hoop have radius R. Assume the hoop is upright and rotates about a vertical axis with angular velocity ω. Let the bead slide on the hoop with coefficient of viscosity γ. Locate the position of the bead on the hoop with the angle θ, as in Fig. 6.10.

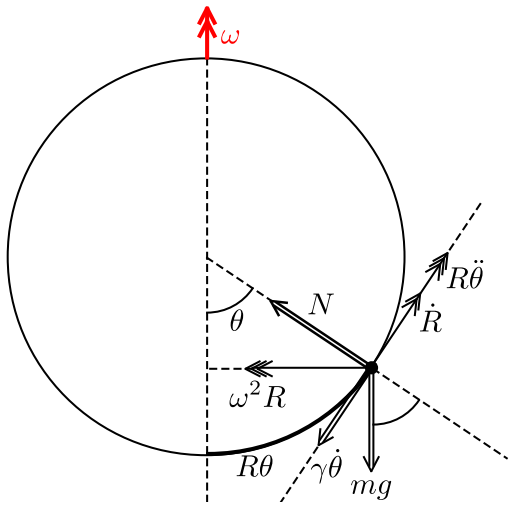

Figure 6.10: Forces and accelerations of a bead sliding on a rotating hoop.

In an inertial reference frame, **Newton's Second Law** of motion requires

$$m\vec{a} = \vec{F} = \vec{N} + m\vec{g} + \gamma\vec{v}_{\|}, \tag{6.15}$$

where $\vec{N}$ is the normal force of the hoop on the bead. Decompose this vector equation tangent to the hoop (in the direction of increasing θ) to get

$$m(-\omega^2 R\sin\theta\cos\theta + R\ddot{\theta}) = F_\theta = 0 - mg\sin\theta - \gamma\dot{\theta}. \tag{6.16}$$

Note how the tangential component of the centripetal acceleration contributes to this equation (on the left), while the unknown normal force makes no contribution (on the right). Rearrange to get

$$mR\ddot{\theta} + \gamma\dot{\theta} = -mg\sin\theta + m\omega^2 R\sin\theta\cos\theta. \tag{6.17}$$

If the mass m is small or the viscosity γ is large, the inertial term $mR\ddot{\theta}$ is negligible with respect to the viscous term $\gamma\dot{\theta}$. Specifically, assume

$$\frac{\gamma}{m} \gg \sqrt{\frac{g}{R}}. \tag{6.18}$$

where $\omega_0 = \sqrt{g/R}$ is the natural frequency of small oscillations of the bead about the bottom of the hoop. Physically, this amounts to assuming that the decay time of such oscillations is much smaller than the period of the oscillations: the decay time is so short that the oscillations damp out before even one oscillation has completed. This assumption reduces the problem to the 1D flow

$$\frac{\gamma}{mg}\dot{\theta} = \sin\theta\left(\frac{\omega^2 R}{g}\cos\theta - 1\right). \tag{6.19}$$

Rescale the time that appears in the derivative to absorb the constants on the left hand side and write

$$\dot{\theta} = \sin\theta(\mu\cos\theta - 1), \tag{6.20}$$

where

$$\mu \equiv \left(\frac{\omega}{\omega_0}\right)^2. \tag{6.21}$$

This 1D flow has fixed points when θ is 0 and $\pm\pi$ for all μ and, in addition, when θ is $\arccos[1/\mu]$ for $\mu \geq 1$. The Fig. 6.11 sketches the velocity curves and the bifurcation diagram. Note the supercritical pitchfork bifurcation at $\mu = 1$. This is made possible mathematically by the invariance of the differential equation under the parity transformation $+\theta \to -\theta$ and physically by the symmetry of the hoop.

What does this analysis tell us about the actual behavior of the bead on the hoop? For slow rotations, when $\omega < \omega_0$ and $\mu < 1$, the $\theta = 0$ hoop bottom is a **stable equilibrium** for the bead, but the $\theta = 0\pi$ hoop top is an **unstable equilibrium**. (Physically, small perturbations cause small oscillations about stable equilibria but cause faraway motion from unstable equilibria.) For fast rotations, when $\omega > \omega_0$ and $\mu > 1$, the hoop bottom becomes unstable and two new stable points are born, symmetrically placed on the hoop about the axis of rotation, as in Fig. 6.12. As the rotation frequency ω increases, these points drift farther and farther from the axis, approaching a maximum distance of R at angles of $\theta = \pm\pi/2$.

In a noninertial reference frame rotating with the hoop, Newton's Second Law fails unless we introduce a **centrifugal pseudo-force** that increases with distance from the rotation axis. The centrifugal pseudo-force is insufficient to balance gravity at slow rotations but can balance gravity at fast rotations, where it amplifies small displacements of the bead from the hoop bottom.

Which fixed point does the bead slide to as the rate of rotation increases through $\omega = \omega_0$? Any slight asymmetry in initial conditions chooses one of the two stable fixed points over the other. This **spontaneous symmetry breaking** makes the solution less symmetric than the equation of motion.

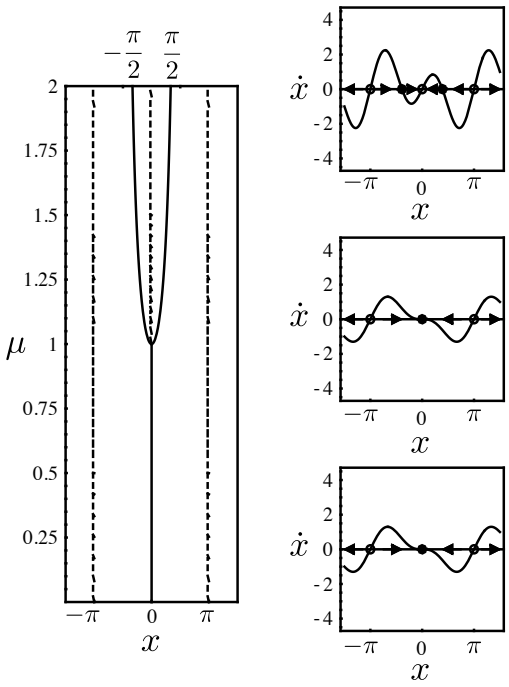

Figure 6.11: Supercritical pitchfork bifurcation of an overdamped bead sliding on a rotating hoop.

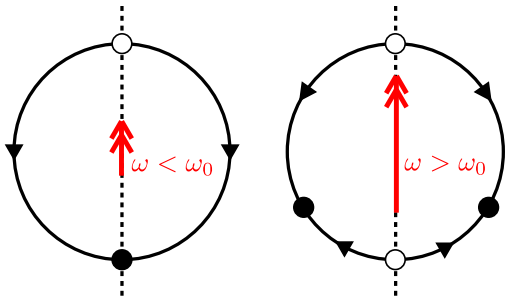

Figure 6.12: Stable and unstable equilibria for slow (left) and fast (right) rotation.

Problems

1. **1D Flows.** Use Mathematica to analyze the 1D flows

   (a) $\dot{x} = 1 + \mu x + x^2$,

   (b) $\dot{x} = x - \mu x(1 - x)$,

   (c) $\dot{x} = x - \mu x^3$.

   Plot all the qualitatively different velocity fields. Construct the bifurcation diagrams.

2. **Broken Pitchfork Bifurcation.** Use Mathematica to analyze the 1D flow

   $$\dot{x} = \lambda + \mu x + x^3. \tag{6.22}$$

   Plot its velocity fields and bifurcation diagrams for positive, zero, and negative symmetry-breaking term λ. Is the pitchfork bifurcation structurally stable?

Chapter 7

2D Flows

Matrices generalize the analysis of 2D flows from 1D flows. Asymptotic behavior includes limit cycles as well as fixed points but no chaos.

7.1 Fixed Points

7.1.1 Classification

Flows on a plane are governed by differential equations of the form

$$\dot{\vec{r}} = \vec{v}[\vec{r}] \tag{7.1}$$

or

$$\frac{d}{dt}\boxed{\begin{array}{c} x \\ y \end{array}} = \boxed{\begin{array}{c} v_x \\ v_y \end{array}}. \tag{7.2}$$

The state space flow is organized in part by the fixed points $\vec{r}_*$ for which the velocity field $\vec{v}[\vec{r}_*]$. Taylor expand the velocity field about these fixed points to infer the local linearized flow

$$\delta\dot{\vec{r}} = J\delta\vec{r}, \tag{7.3}$$

where

$$J = \frac{\partial \vec{v}}{\partial \vec{r}} = \boxed{\begin{array}{cc} \partial_x v_x & \partial_y v_x \\ \partial_x v_y & \partial_y v_y \end{array}} \tag{7.4}$$

is the **Jacobian matrix** of partial derivatives evaluated at the fixed point $\vec{r}_*$, and $\vec{r} = \vec{r} - \vec{r}_*$ is the relative position with respect to the fixed point.

The Jacobian matrix generalizes the single derivative of the 1D theory. Its **eigenvalues** and **eigenvectors** determine the linearized state space flow. The Jacobian

$$J = \boxed{\begin{array}{cc} a & b \\ c & d \end{array}} \tag{7.5}$$

has eigenvalues

$$\lambda_\pm = \frac{1}{2}(\tau \pm D) \tag{7.6}$$

and eigenvectors

$$\vec{v}_\pm = \boxed{\begin{matrix} \lambda_\pm - d \\ c \end{matrix}} = \boxed{\begin{matrix} b \\ \lambda_\pm - a \end{matrix}}, \tag{7.7}$$

where J's **determinant**

$$\delta \equiv \det J = ad - bc = \lambda_+ \lambda_-, \tag{7.8}$$

trace

$$\tau \equiv \mathrm{tr} J = a + b = \lambda_+ + \lambda_-, \tag{7.9}$$

and **discriminant**

$$D \equiv \sqrt{\tau^2 - 4\delta} = \lambda_+ - \lambda_-. \tag{7.10}$$

If the eigenvalues are distinct, then the eigenvectors are linearly independent and the local flow is

$$\delta\vec{r} = c_+ e^{\lambda_+ t}\vec{v}_+ + c_- e^{\lambda_- t}\vec{v}_-, \tag{7.11}$$

where initial conditions determine the constants $c_\pm$.

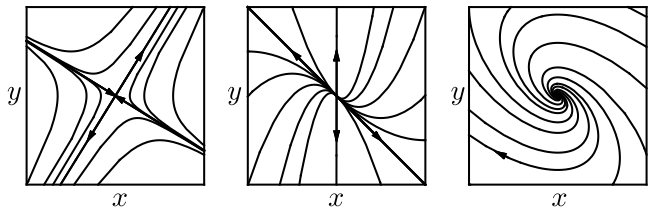

Figure 7.1: Three generic fixed points: saddle (left), node (center), spiral (right).

Three generic kinds of local flow characterize the fixed points, as in Fig. 7.1. If the eigenvalues are real, then the eigenvectors are real also. If the real eigenvalues have different signs, for example $\lambda_- < 0 < \lambda_+$, then the fixed point is a **saddle point**. The corresponding eigenvectors correspond to stable (incoming) and unstable (outgoing) directions, and the local flow is hyperbolic. This velocity field is reminiscent of the motion of marbles rolling on a horse's saddle. If the real eigenvalues are both negative, for example $\lambda_- < \lambda_+ < 0$, then the fixed point is a **stable node**. The corresponding eigenvectors correspond to fast and slow stable directions. The local $t \to +\infty$ flow is tangent to the slower direction, while the distant (linearized) $t \to -\infty$ is tangent to the faster direction. If the real eigenvalues are both positive, for example $0 < \lambda_- < \lambda_+$, then the fixed point is an **unstable node**. The node and saddle eigenvectors are **tangent vectors** to the full nonlinear flow.

If the eigenvalues are complex, then the eigenvectors are complex also, so that the state space points are real. Since the eigenvalues are complex conjugate

pairs, $\lambda_\pm = \alpha \pm i\omega$, the components of $\delta\vec{r}$ are linear combination of $\exp[\alpha \pm i\omega]$, which is equivalent to a linear combinations of $\exp[\alpha t]\sin[\omega t]$ and $\exp[\alpha t]\cos[\omega t]$ by Euler's formula. Thus, the local flow spirals around the fixed point. If the real part of the eigenvalues is positive, then the fixed point is an unstable spiral repellor. If the real part of the eigenvalues is negative, then the fixed point is a stable spiral attractor. A special nongeneric case is when the real part vanishes, and the local flow circles a center or elliptic point.

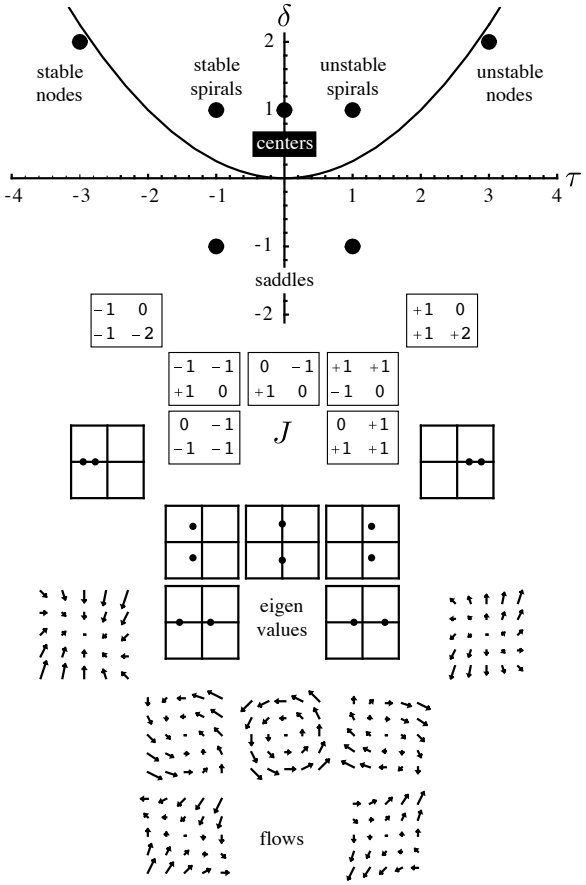

Figure 7.2: Fixed point classification, according to Jacobian's trace τ and determinant δ (1st row); representative Jacobian matrices (2nd row); corresponding eigenvalues, shown in complex planes (3rd row); corresponding linearized flows: nodes (top), spirals (center), saddles (bottom) (4th row).

The trace and determinant of the Jacobian matrix of partial derivatives can classify the fixed points. Figure 7.2 summarizes the classification in the $\{\tau, \delta\}$ plane. If the linearized analysis predicts a generic local state space flow (saddles, nodes, or spirals), then the full nonlinear flow will exhibit topologically similar behavior nearby. However, if the linearized analysis predicts a nongeneric local state space flow (such as a center), then the full nonlinear flow may or may not

exhibit similar behavior nearby.

7.1.2 Compound Example

Often the global behavior of a state space flow extrapolates from the local behaviors in the vicinities of the fixed points. For example, consider the nonlinear flow

$$\dot{x} = x - y, \tag{7.12a}$$

$$\dot{y} = x^2 - 2. \tag{7.12b}$$

Fixed points are obviously $\{\pm\sqrt{2}, \pm\sqrt{2}\}$. The Jacobian is

$$J[x, y] = \boxed{\begin{matrix} 1 & -1 \\ 2x & 0 \end{matrix}}. \tag{7.13}$$

Its eigenvalues at $\{\sqrt{2}, \sqrt{2}\}$ are $(1 \pm i\sqrt{15})/2$, an unstable spiral. Its eigenvalues at $\{-\sqrt{2}, -\sqrt{2}\}$ are $(-1 \pm \sqrt{17})/2$, a saddle with unstable and stable directions given by the corresponding eigenvectors $\{(-1 \pm \sqrt{17})/8, 1\}$. Figure 7.3 plots the vector field. Note how the local flows dovetail to form the global flow.

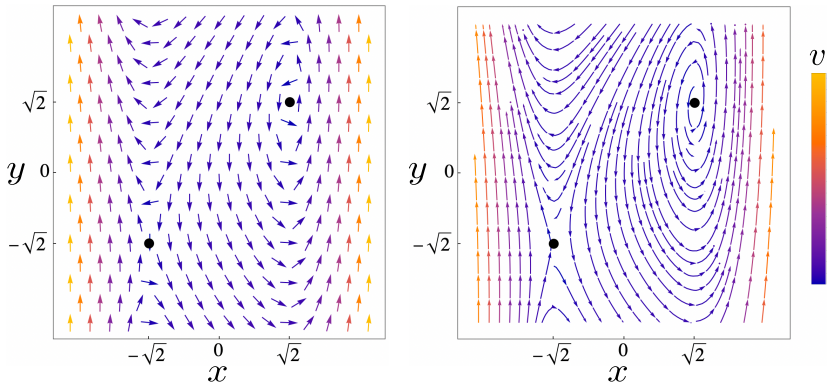

Figure 7.3: 2D velocity field of state space flow, with saddle and unstable spiral.

7.1.3 Homoclinic & Heteroclinic Orbits

Newton's Second Law of motion is a rich source of many important flows. The nonlinear **double-well** nonlinear-spring equation

$$\ddot{x} = x - x^3 \tag{7.14}$$

is equivalent to the 2D flow

$$\dot{x} = y, \tag{7.15a}$$

$$\dot{y} = x - x^3. \tag{7.15b}$$

Linearizaton predicts a saddle at $\{0,0\}$ and two centers at $\{\pm 1,0\}$. Because the flow is invariant under the transformation $\{y,t\} \to \{-y,-t\}$, every orbit in the upper half plane has a time-reversed mirror-reflected orbit in the lower half plane. This symmetry ensures that the linear centers are also nonlinear centers.

Figure 7.4(left) plots the flow. **Homoclinic orbits** connect the unstable directions of the saddle to its stable directions and separate the state space flow into three distinct regions. These **separatrices** require infinite time to traverse.

Newton's Second Law also provides a familiar example, now viewed in a new light. The nonlinear pendulum equation

$$\ddot{x} = -\sin x \tag{7.16}$$

is equivalent to the 2D flow

$$\dot{x} = y, \tag{7.17a}$$
$$\dot{y} = -sinx. \tag{7.17b}$$

Linearizaton predicts saddles at $\{\pm\pi,0\}$ and a center at $\{0,0\}$. Because the flow is invariant under the **parity** transformation $\{x,y \to \{-x,-y\}\}$, it must be both left-right and top-bottom symmetric. This symmetry ensures that the linear center at the origin is also a nonlinear center.

Figure 7.4(right) plots the flow. **Heteroclinic orbits** connect the unstable directions of one saddle to the stable directions of another saddle (and vice versa) and separate the state space flow into distinct regions (of **rotation** and **libration**). These separatrices require infinite time to traverse.

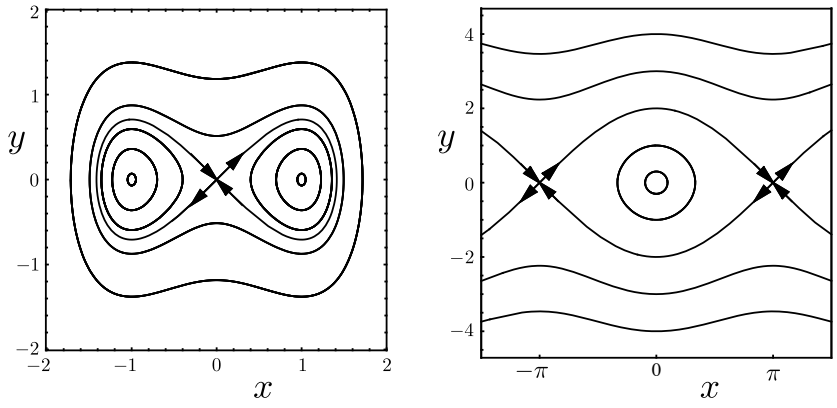

Figure 7.4: Homoclinic orbits connect stable and unstable directions of same saddle (left). Heteroclinic orbits connect stable and unstable directions of different saddles (right).

7.2 Limit Cycles

7.2.1 Overview

In 1D state spaces, fixed points alone organize that state space flow. However, 2D state spaces admit another possibility, namely isolated closed trajectories called **limit cycles**. Limit cycles may be stable or unstable (or bistable). Stable limit cycles can model systems that exhibit self-sustained oscillations, like heart beats. Limit cycles are inherently nonlinear and are qualitatively distinct from linear centers (elliptic fixed points). A center is a family of closed nonisolated orbits whose amplitudes depend upon initial conditions. A limit cycle is a closed isolated orbit whose amplitude (and frequency and waveform) depends on the system and not on the initial conditions.

7.2.2 Limit Cycle Example

Consider the 2D flow.

$$\dot{x} = x - y - x^3 - xy^2, \tag{7.18a}$$

$$\dot{y} = x + y - x^2 y - y^3. \tag{7.18b}$$

A fixed point is the origin. The Jacobian

$$J[x,y] = \boxed{\begin{array}{cc} \partial_x \dot{x} & \partial_y \dot{x} \\ \partial_x \dot{y} & \partial_y \dot{y} \end{array}} = \boxed{\begin{array}{cc} 1 - 3x^2 - y^2 & -1 - 2xy \\ 1 - 2xy & 1 - x^2 - 3y^2 \end{array}} \tag{7.19}$$

at the origin is

$$J[0,0] = \boxed{\begin{array}{cc} +1 & -1 \\ +1 & +1 \end{array}}, \tag{7.20}$$

which has eigenvalues $\lambda_\pm = 1 \pm i$. Thus, the origin is an unstable spiral – but with a surprise. Converting to polar coordinates to further analyze the spiral motion is natural. Let

$$x = r\cos\theta, \tag{7.21a}$$

$$y = r\sin\theta, \tag{7.21b}$$

and the 2D flow becomes

$$\dot{r}\cos\theta - r\sin\theta\,\dot{\theta} = r\cos\theta - r\sin\theta - r^3\cos\theta, \tag{7.22a}$$

$$\dot{r}\sin\theta + r\cos\theta\,\dot{\theta} = r\cos\theta + r\sin\theta - r^3\sin\theta, \tag{7.22b}$$

which simplifies to

$$\dot{r} = r - r^3, \tag{7.23a}$$

$$r\dot{\theta} = r \tag{7.23b}$$

or

$$\dot{r} = r(1-r)(1+r), \tag{7.24a}$$

$$\dot{\theta} = 1. \tag{7.24b}$$

The radial and angular dynamics are uncoupled! Integrate the θ equation immediately to get $\theta = \theta_0 + t$, which represents rotation at constant angular velocity. The r equation is a nonlinear 1D flow with (unsurprisingly) an unstable fixed point at $r = 0$ but also a stable fixed point at $r = 1$. In the $\{x, y\}$ plane, this stable radial fixed point corresponds to a stable limit cycle that separates the unstable spiral at the origin from infinity, as in Fig. 7.5.

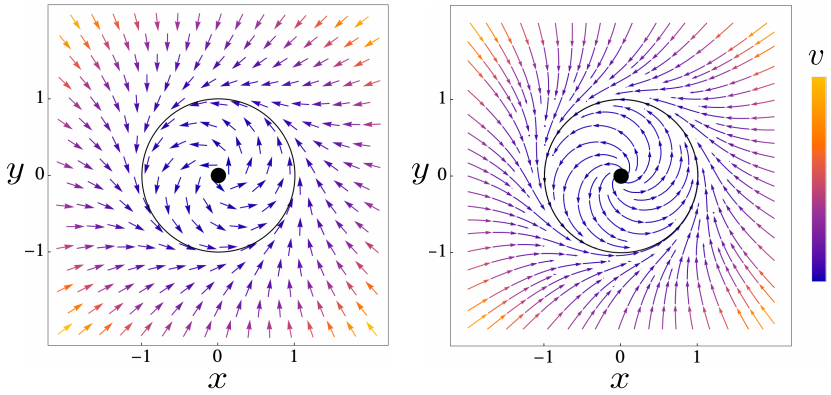

Figure 7.5: Example stable limit cycle at $r = 1$.

7.2.3 Poincaré-Bendixson Theorem

In 2D state space, are there any asymptotic sets other than fixed points and limit cycles? The **Poincaré-Bendixson theorem** says no. Specifically, suppose a state space trajectory is confined to a finite region in a 2D state space. Then, as $t \to \infty$, the trajectory either approaches a fixed point or a limit cycle. The proof relies on the **No-Intersection theorem** of ordinary differential equations. (State space trajectories cannot intersect themselves.)

The Poincaré-Bendixson theorem holds only in 2D, because only in 2D does a closed curve separate space into an "inside" and an "outside". An important consequence is that in 2D, only two types of attractors exist: 0D attractors (fixed or limit points) and 1D attractors (limit cycles). In particular, no chaotic attractors exist in 2D.

7.3 Bifurcations

7.3.1 Overview

Bifurcations in 2D state space generalize bifurcations in 1D state space. Once again, a signature of a bifurcation is qualitative change in the state space flow as a parameter varies. Fixed points can be created or destroyed, stabilized or destabilized. Similarly, limit cycles can be create or destroyed and spontaneous oscillations can start or stop.

7.3.2 Fixed Point

Fixed point bifurcations in 2D are analogous to fixed point bifurcations in 1D with no new surprises. The following simple examples introduce exponentially damped motion orthogonal to the 1D normal forms. For example, the 2D flow

$$\dot{x} = \mu - x^2, \tag{7.25a}$$
$$\dot{y} = -y \tag{7.25b}$$

exhibits a **saddle-node** bifurcation. As the parameter μ decreases through zero, a saddle and a node coalesce and annihilate. The flow

$$\dot{x} = \mu x - x^2, \tag{7.26a}$$
$$\dot{y} = -y \tag{7.26b}$$

exhibits a **transcritical** bifurcation. As the parameter μ decreases through zero, the stable node collides with an unstable node at the origin. The nodes swap stability, thereby stabilizing the origin. The flow

$$\dot{x} = \mu x - x^3, \tag{7.27a}$$
$$\dot{y} = -y \tag{7.27b}$$

exhibits a **pitchfork** bifurcation. As the parameter μ decreases through zero, two stable nodes converge on a saddle at the origin, thereby converting it to a stable node.

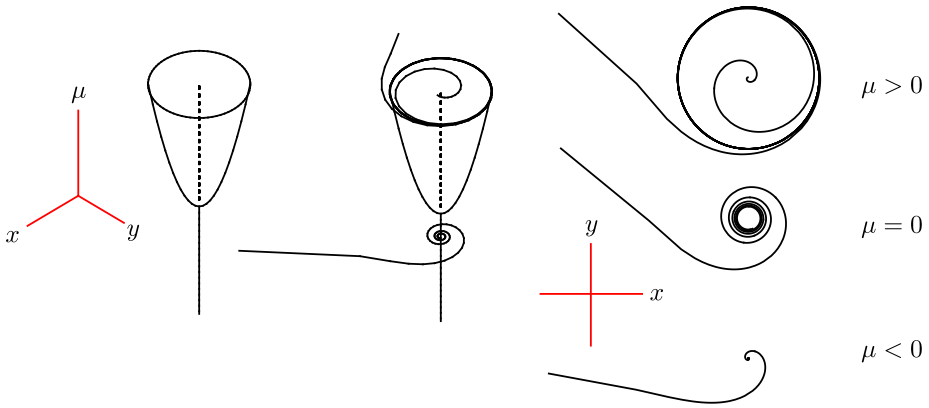

Figure 7.6: Supercritical Hopf bifurcation: a stable limit cycle appears at $\mu = 0$. As μ increases, the appearance of a stable limit cycle destabilizes a spiral point.

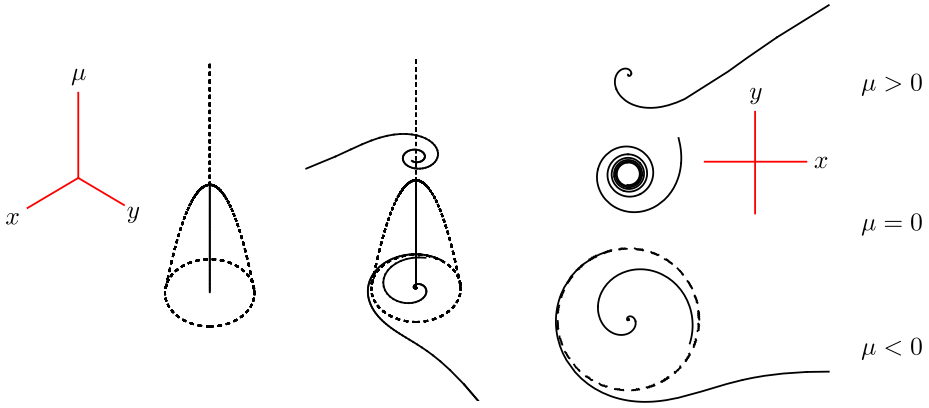

Figure 7.7: Subcritical Hopf bifurcation: a unstable limit cycle disappears at $\mu = 0$. As μ increases, the disappearance of an unstable limit cycle destabilizes a spiral point.

7.3.3 Limit Cycle

Easily concoct a simple example of limit cycle bifurcation by working in polar coordinates. Let the radial coordinate be governed by the 1D pitchfork bifurcation normal form, and the let the angular coordinate increase at a constant rate,

$$\dot{r} = \mu r - r^3, \tag{7.28a}$$

$$\dot{\theta} = 1. \tag{7.28b}$$

In rectangular coordinates, this becomes

$$\dot{x} = \mu x - y - x^3 - xy^2, \tag{7.29a}$$

$$\dot{y} = x + \mu y - x^2 y - y^3. \tag{7.29b}$$

Since the angular and radial dynamics are uncoupled, and the angular dynamics is a trivial constant rotation, all the action comes from the pitchfork bifurcation of the radial coordinate. Note, however, that here $r > 0$. The origin is a stable spiral for $\mu < 0$. However, as μ increase through zero, this spiral destabilizes and gives birth to a stable limit cycle at $r = \sqrt{\mu}$. This is an example of a **supercritical Hopf** bifurcation. For $\mu < 0$, perturbations damp out naturally, while for $\mu > 0$, perturbations grow into stable oscillations, as in Fig. 7.6.

Notice the very slow spiral flow as μ passes through zero. Linearized stability analysis predicts a nongeneric center point at the origin for $\mu = 0$. However, the full nonlinear equations exhibit a nonexponential spiral. The linearized analysis can fail only when it predicts such nongeneric behavior.

Similarly, consider the flow

$$\dot{r} = \mu r + r^3, \tag{7.30a}$$

$$\dot{\theta} = 1. \tag{7.30b}$$

Again, the origin is a stable spiral for $\mu < 0$, but now it is accompanied by an unstable limit cycle at $r = \sqrt{-\mu}$. As μ increase through zero, the unstable limit cycle shrinks to zero and destabilizes the spiral at the origin. This is an example of a **subcritical Hopf** bifurcation, as in Fig. 7.7.

Problems

1. **2D Flows.** Use Mathematica to analyze the 2D flows

$$\dot{x} = x - y, \tag{7.31a}$$
$$\dot{y} = x^2 - 4, \tag{7.31b}$$

and

$$\dot{x} = y - y^3, \tag{7.32a}$$
$$\dot{y} = -x - y^2. \tag{7.32b}$$

Find and classify each fixed point. Linearize and plot the local flows. Plot the global flows.

2. **Newton's Second Law.** Analyze the nonlinear pendulum

$$\ddot{x} = -\sin x \tag{7.33}$$

and nonlinear spring

$$\ddot{x} = x - x^3 \tag{7.34}$$

flows.

3. **Van der Pol Oscillator.** Use Mathematica to investigate the 2D flow

$$\ddot{x} - \mu(1 - x^2)\dot{x} = -x, \tag{7.35}$$

where μ controls the nonlinear damping. In the 1920s, this oscillator was constructed using vacuum tubes. It beat spontaneously like a heart, but also exhibited irregular "noise", which was much later understood to be chaos.

Chapter 8

3D Flows

Physicist George Gamow wrote a general science book entitled *One, Two, Three, ... Infinity*, which well describes nonlinear dynamical flows. In nonlinear dynamics, 2D state spaces are much richer than 1D state spaces, but 3D spaces are much richer still. Like infinite dimensional state spaces, 3D state spaces exhibit strange attracting sets characterized geometrically by fractional dimensions and characterized dynamically by extreme sensitivity to initial conditions, or chaos.

8.1 Fixed Points

3D flows are governed by differential equations of the form

$$\dot{\vec{r}} = \vec{v}[\vec{r}] \tag{8.1}$$

or

$$\frac{d}{dt}\boxed{\begin{array}{c} x \\ y \\ z \end{array}} = \boxed{\begin{array}{c} v_x \\ v_y \\ v_z \end{array}}. \tag{8.2}$$

The state space flow is organized in part by the fixed points $\vec{r}_*$ for which the velocity field $\vec{v}[\vec{r}_*]$. **Taylor expand** the velocity field about these fixed points to infer the local linearized flow

$$\delta\dot{\vec{r}} = J\delta\vec{r}, \tag{8.3}$$

where

$$J = \frac{\partial \vec{v}}{\partial \vec{r}} = \boxed{\begin{array}{ccc} \partial_x v_x & \partial_y v_x & \partial_z v_x \\ \partial_x v_y & \partial_y v_y & \partial_z v_y \\ \partial_x v_z & \partial_y v_z & \partial_z v_z \end{array}} \tag{8.4}$$

is the **Jacobian matrix** of partial derivatives evaluated at the fixed point $\vec{r}_*$, and $\vec{r} = \vec{r} - \vec{r}_*$ is the relative position with respect to the fixed point.

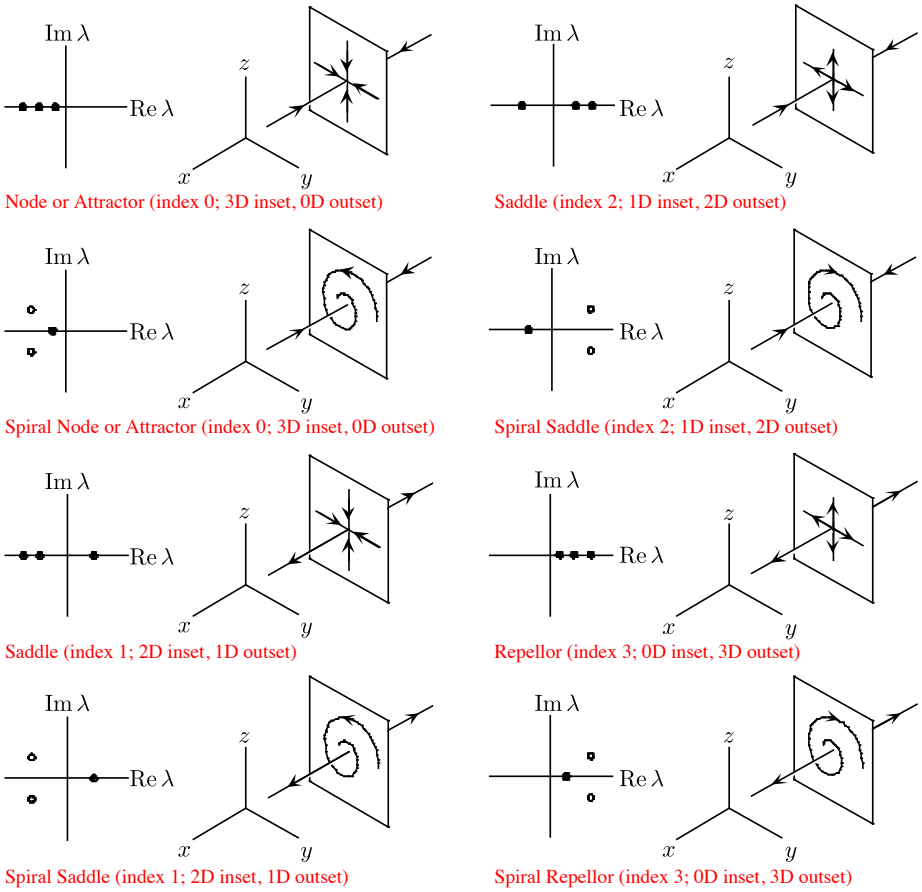

Figure 8.1: Classification of 3D fixed points.

The 3D Jacobian matrix generalizes the single derivative of the 1D theory and the corresponding 2D matrix of the 2D theory. Its **eigenvalues** and **eigenvectors** determine the linearized state space flow. Explicit expressions for these three eigenvalues and eigenvectors are cumbersome and not very useful.

If the eigenvalues λ_n are distinct, then the eigenvectors $\vec{v}_n$ are linearly independent and the local flow is

$$\delta\dot{\vec{r}} = c_1 e^{\lambda_1 t}\vec{v}_1 + c_2 e^{\lambda_2 t}\vec{v}_2 + c_3 e^{\lambda_3 t}\vec{v}_3, \tag{8.5}$$

where the constants c_n are determined by the initial conditions. Four pairs of generic local flow characterize the fixed points: nodes or attractors, repellors, and two kinds of saddles. Classify these according to the location of the eigenvalues in the complex plane.

To help distinguish higher-dimensional saddles, whose stable and unstable

locally-Euclidean **manifolds** may have one or two dimensions, introduce the following terminology. Let the **index** of a fixed point denote the number of dimensions of its unstable manifold. Alternately, the index is the number of eigenvalues of a fixed point whose real parts are positive. Let the **inset** (or "in-set") and **outset** (or "out-set") denote, respectively, the sets of all incoming and outgoing trajectories. Figure 8.1 classifies generic 3D fixed points.

8.2 Limit Cycles

Limit cycles also help organize 3D flows. These can combine with fixed points in several different ways. Figure 8.2 demonstrates a saddle cycle.

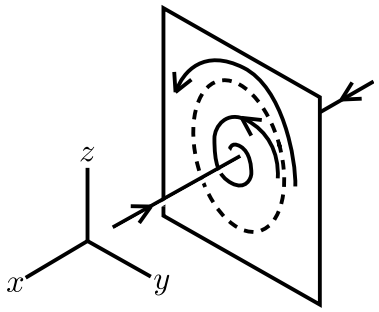

Figure 8.2: Schematic of a saddle cycle in 3D state space.

8.3 Lorenz Flow

8.3.1 Equations

The most famous 3D flow is the Lorenz model of fluid convection

$$\dot{x} = -\sigma x + \sigma y, \tag{8.6a}$$

$$\dot{y} = -y + \rho x - xz, \tag{8.6b}$$

$$\dot{x} = -\beta z + xy. \tag{8.6c}$$

The derivation of these equations from the Navier-Stokes fluid flow equations is complicated and not specifically relevant. Take them as given. Notice the two nonlinear terms xz and xy. The 3D parameter space $\{\sigma, \beta, \rho\}$ is large. Like Lorenz, focus on $\sigma = 10$, $\beta = 8/3$, and $0 < \rho < 28$. (ρ is proportional to the experimentally accessible temperature differential in the convection model.)

8.3.2 Obervations

First, the Lorenz flow is invariant under reflections in the z axis. If $\{x[t], y[t], z[t]\}$ is a solution, then $\{-x[t], -y[t], -z[t]\}$ is also solution. Thus, if a solution is not

itself symmetric, then it must have a symmetric partner.

Second, the Lorenz flow is dissipative. Since the divergence of the flow

$$\vec{\nabla} \cdot \vec{v} = \partial_x v_x + \partial_y v_y + \partial_z v_z = -(\sigma + \beta + 1) < 0 \tag{8.7}$$

is always negative, state space volumes must decrease

$$\dot{V} = \int \vec{\nabla} \cdot \vec{v}\, dV = -(\sigma + \beta + 1)V < 0 \tag{8.8}$$

and shrink exponentially to zero like

$$V[t] = V[0]e^{-(\sigma+\beta+1)t}. \tag{8.9}$$

The flow in the 3D state space must be squeezed onto an attractor of smaller dimension, and hence zero volume.

Third, a **trapping region** shows that the Lorenz flow cannot escape to infinity, but must remain bounded. Consider the sphere defined by

$$r^2 = x^2 + y^2 + (z - \rho - \sigma)^2. \tag{8.10}$$

The distance r to the point $\{0, 0, \rho + \sigma\}$ decreases along an orbit provided

$$0 < (r^2)^{\cdot} = 2x\dot{x} + 2y\dot{y} + 2(z - \rho - \sigma)\dot{z}, \tag{8.11}$$

which via the Lorentz equations becomes

$$0 < -\sigma x^2 - y^2 - \beta z(z - \rho - \sigma), \tag{8.12}$$

and after completing the square and rearranging becomes

$$\sigma x^2 + y^2 + \beta \left(z - \frac{\rho + \sigma}{2} \right)^2 > \beta \left(\frac{\rho + \sigma}{2} \right)^2. \tag{8.13}$$

Hence, r must decrease for all orbits outside this ellipsoid, which is centered on $\{0, 0, (\rho + \sigma)/2\}$.

8.3.3 Bifurcation

The Lorenz flow has 3 fixed points, the origin $\mathcal{O}$ and the symmetrically placed $\mathcal{C} \equiv \{\pm\sqrt{\beta(\rho - 1)}, \pm\sqrt{\beta(\rho - 1)}, \rho - 1\}$. They may be classified according to the eigenvalues of the Jacobian matrix of partial derivatives

$$J[x, y, z] = \begin{bmatrix} -\sigma & \sigma & 0 \\ \rho - z & -1 & -x \\ y & x & -\beta \end{bmatrix} \tag{8.14}$$

evaluated at the fixed points. The **characteristic equation** for the eigenvalues λ at $\mathcal{O}$ is

$$0 = (\lambda + \beta)\left(\lambda^2 + (\sigma + 1)\lambda - \sigma(\rho - 1)\right), \tag{8.15}$$

and the characteristic equation at $\mathcal{C}_\pm$ is

$$0 = \lambda^3 + (1 + \sigma + \beta)\lambda^2 + \beta(\rho + \sigma)\lambda + 2\sigma\beta(\rho - 1). \tag{8.16}$$

Explicit solutions to generic cubic equations are available, but they are cumbersome. Figure 8.3 summarizes the qualitative changes in the fixed point stability below for $\sigma = 10$, $\beta = 8/3$, and $0 < \rho < 28$.

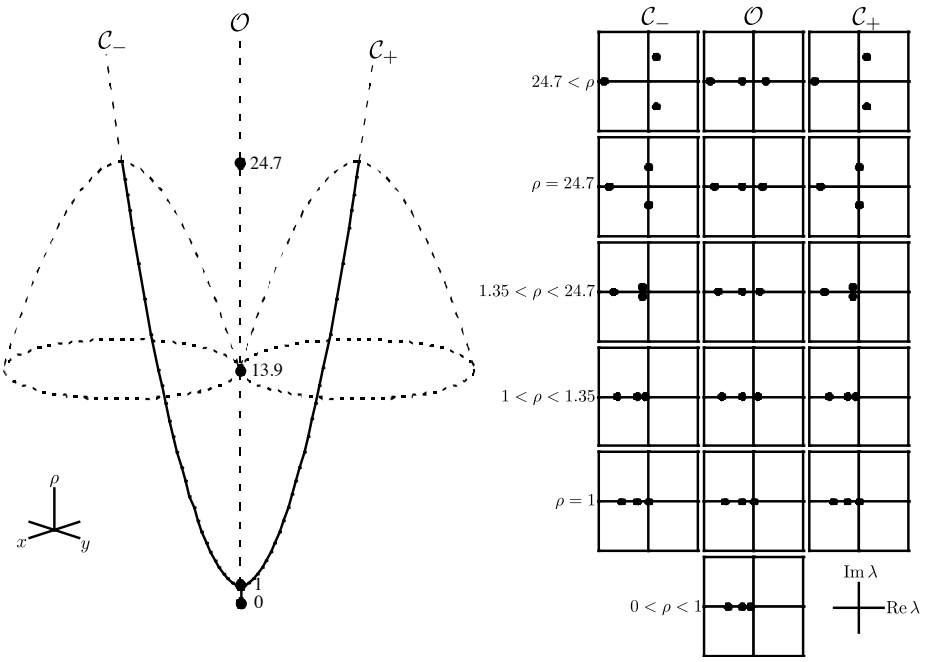

Figure 8.3: Lorenz bifurcation diagram (left); fixed point eigenvalues in the complex plane (right). Other parameters $\sigma = 10$ and $\beta = 8/3$.

Imagine increasing the parameter ρ from zero. The origin $\mathcal{O}$ is an attracting fixed point, a node, for $\rho < 1$. But $\mathcal{O}$ loses its stability in a **supercritical pitchfork** bifurcation at $\rho = 1$, when it gives rise to a pair of nodes $\mathcal{C}_\pm$, which become stable spiral saddles at $\rho \approx 1.35$. However, at $\rho \approx 24.7$, $\mathcal{C}_\pm$ lose stability by absorbing an unstable limit cycle in a **subcritical Hopf** bifurcation. Now, imagine decreasing ρ from this point. The saddle cycles grow in size until they touch the stable and unstable manifolds of the $\mathcal{O}$ saddle, at $\rho \approx 13.9$, and disappear in a **homoclinic** bifurcation.

The bifurcation diagram reflects the behavior of the fixed points' eigenvalues in the complex plane. Notice, in particular, the transitions that occur at $\rho = 1$ and $\rho \approx 24.7$. For $\rho < 1$, all orbits are attracted to the origin $\mathcal{O}$. For $1 < \rho \lesssim 24.7$, orbits are deflected from $\mathcal{O}$ to the pair $\mathcal{C}_\pm$. These spiral points become weaker and weaker as ρ increases, resulting in **transient chaos**. Finally, for $24.7 \lesssim \rho$, the spirals become unstable and orbits bounce back and

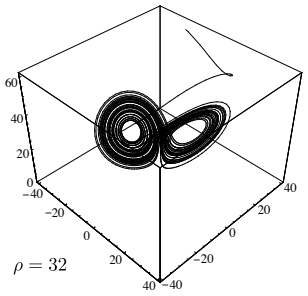

Single chaotic orbit bounces between unstable spirals.

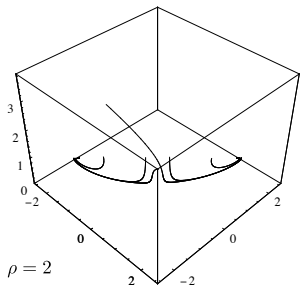

Six orbits asymptote to a pair of strongly stable spirals.

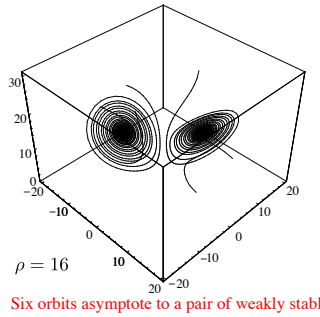

Six orbits asymptote to a pair of weakly stable spirals.

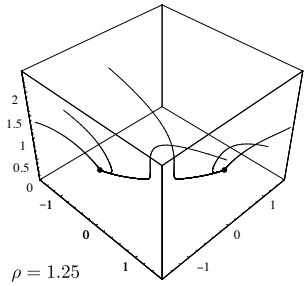

Six orbits asymptote to a pair of nodes.

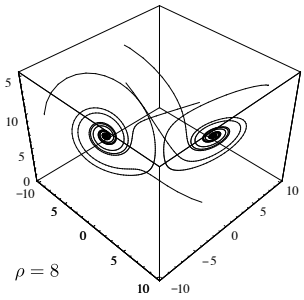

Six orbits asymptote to a pair of stable spirals.

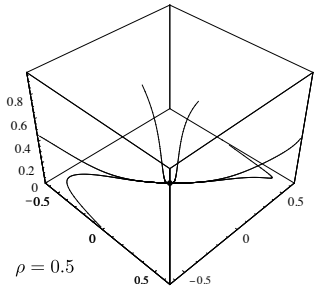

Six orbits asymptote to a node at the origin.

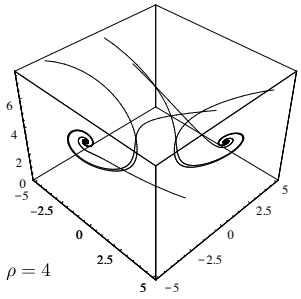

Six orbits asymptote to a pair of stable spirals.

Figure 8.4: Lorenz $\{x, y, z\}$ flows for $0 < \rho < 32$. Other parameters $\sigma = 10$ and $\beta = 8/3$. Plot ranges are larger for larger ρ.

forth between $\mathcal{C}_+$ and $\mathcal{C}_-$ on a **strange** and **chaotic attractor**. Figure 8.4 summarizes the Lorenz bifurcating flows. The Lorenz velocity field results from a pair of misaligned vortices separated by a saddle.

8.4 Rössler Flow

8.4.1 Equations

Another famous 3D flow is due to the **Rössler system**

$$\dot{x} = -y - z \tag{8.17a}$$
$$\dot{y} = x + ay, \tag{8.17b}$$
$$\dot{z} = b - cz + xz. \tag{8.17c}$$

This is an artificial flow designed by Otto Rössler [13]. It mimics the folding and bending of taffy in a taffy machine. It contains only one nonlinear term, the xz in the third equation. The 3D parameter space $\{a, b, c\}$ is large. Focus attention on $0 < a < 2$, $b = 2$, and $c = 4$.

8.4.2 Observations

The Rössler flow lacks the symmetry of the Lorenz flow, which makes it more difficult to analyze. Since the divergence of the flow is

$$\vec{\nabla} \cdot \vec{v} = \partial_x v_x + \partial_y v_y + \partial_z v_z = a - c + x, \tag{8.18}$$

state space volumes sometimes decrease and sometimes increase. No global trapping region exists, as orbits can be spun out to infinity (by the far fixed point).

8.4.3 Bifurcation

The flow has 2 fixed points, $\vec{x}_\pm = \{c \pm D, -(c \pm D)/a, (c \pm D)/a\}/2$, where $D \equiv \sqrt{c^2 - 4ab}$. $\vec{x}_+$ is near the origin, while $\vec{x}_-$ is faraway; they coalesce and disappear at $c^2 = 4ab$. The fixed points may be classified according to the eigenvalues of the Jacobian matrix of partial derivatives

$$J[x, y, z] = \boxed{\begin{array}{ccc} 0 & -1 & -1 \\ 1 & a & 0 \\ z & 0 & x - c \end{array}} \tag{8.19}$$

evaluated at the fixed points. The **characteristic equation** for the eigenvalues λ is

$$\lambda^3 + (c - a - x)\lambda^2 + (1 - ac + ax + z)\lambda + (c - x - az) = 0. \tag{8.20}$$

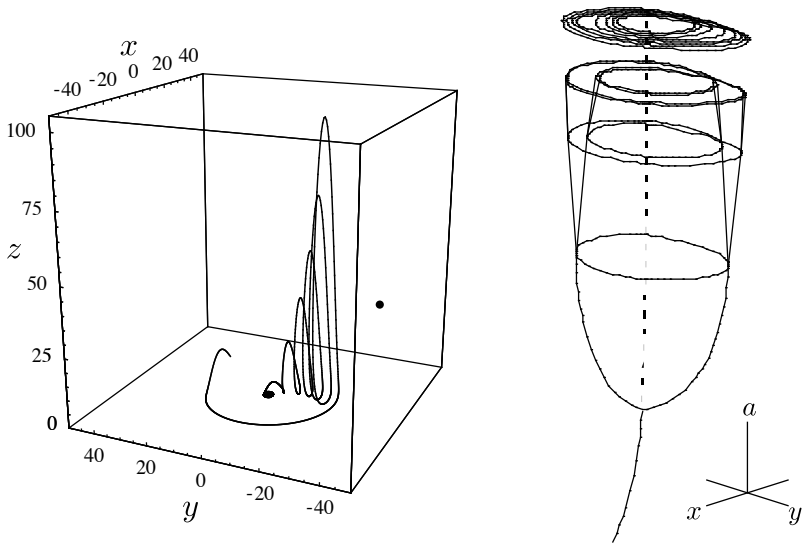

Figure 8.5: Rössler flow for $a = 0.1$ (left), illustrating the interaction of the near and far fixed points. Schematic bifurcation diagram (right). Other parameters $b = 2$ and $c = 4$.

Explicit solutions to generic cubic equations are available, but they are cumbersome. Figure 8.5 summarizes the qualitative changes in the fixed point stability for $0 < a < 2$, $b = 2$, and $c = 4$.

Imagine increasing the parameter a from zero. The near fixed point is a spiral attractor (index 0). The far fixed point is a spiral saddle (index 1). Its 2D inset acts as a separatrix by either spiralling an orbit out to infinity or spiralling it into the near fixed point at the origin.

For $a \lesssim 0.12$, orbits near the origin spiral into the near fixed point. At $a \approx 0.12$, the stable spiral at the near fixed point undergoes a Hopf bifurcation as it becomes unstable in giving birth to a stable limit cycle. The stable limit cycle grows in size until, at $a \approx 0.35$, the cycle bifurcates into a stable 2-cycle. At $a \approx 0.375$, the cycle bifurcates again into a stable 4-cycle. This continues until a ∞-cycle chaotic attractor emerges at $a \approx 0.398$. Thereafter, windows of periodicity appear amid the chaos. For example, at $a \approx 0.411$, a stable 3-cycle exists. Figure 8.6 summarizes the bifurcating flows.

The Rössler velocity field results from the interaction of two crossed vortices, one near the origin, the other far away, pointing at the "fold" in the Rössler "band".

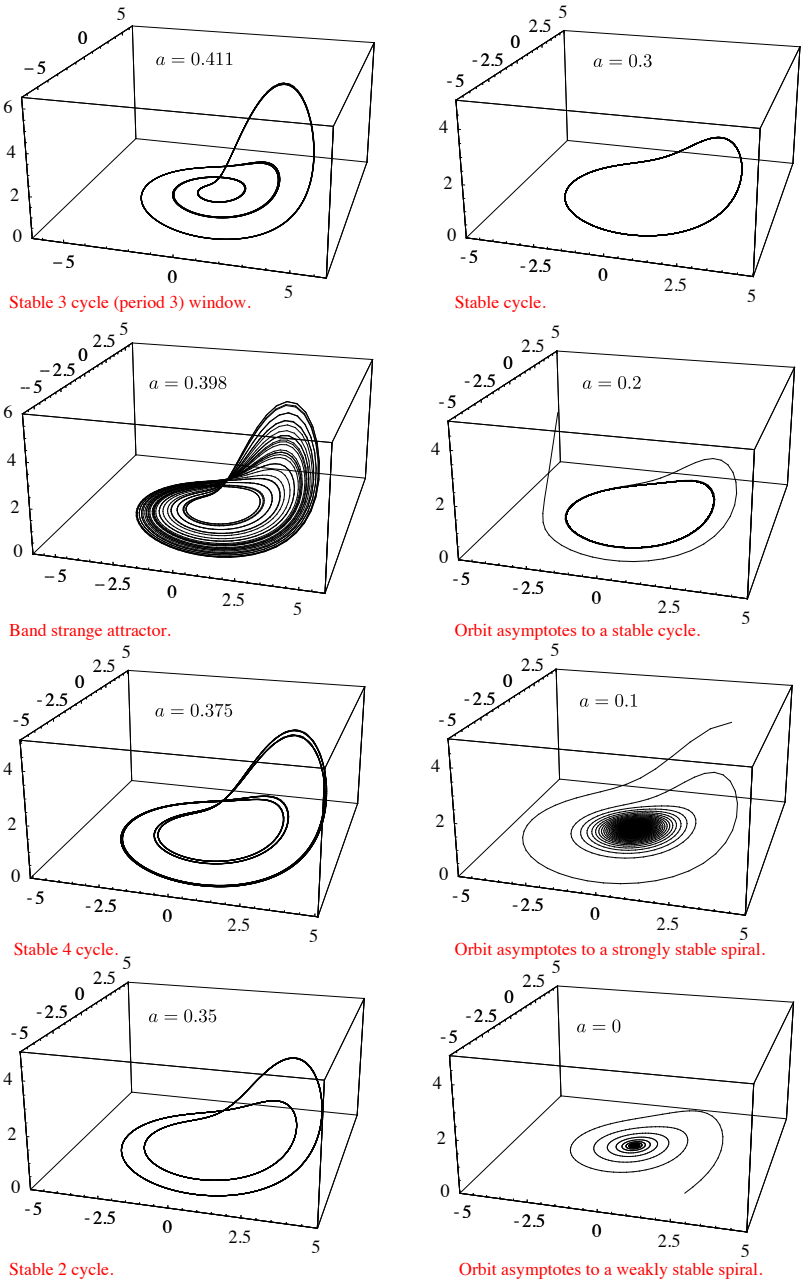

Figure 8.6: Rössler $\{x, y, z\}$ flows for $0 < a < 0.411$. Other parameters $b = 2$ and $c = 4$. Vertical plot ranges are larger for larger a.

8.5 Strange & Chaotic Attractors

Attractors are invariant sets that attract all sufficiently near orbits. Orbits on a **chaotic attractor** exhibit sensitive dependence on initial conditions, while a **strange attractor** exhibits the self-similar microstructure of a **fractal**. The properties of strange and chaotic often occur together, but not always: there exists **strange nonchaotic attractors**. However, the Lorenz and Rössler attractors are both strange and chaotic.

The splitting and interlacing of the Lorenz flow produce a strange attractor. Imagine a cloud of initial points on the attractor being split apart by the saddle at the origin, spun around each unstable spiral many times, and finally interlaced at the saddle again. The layers seem to merge into a 2D surface, but this is impossible, as merging surfaces would imply intersecting trajectories which would violate the uniqueness of the state space flow. Instead, tiny gaps remain on all scales. Figure 8.7(top) illustrates the splitting and interlacing of the Lorenz flow.

It is the continuous folding of the Rössler flow that produces a strange attractor. The near spiral alone would generate a flat band attractor, but the interaction of the far spiral lifts the band into the third dimension and folds it, along the outer edge, back into the band. As with the Lorenz flow, the merging can not be complete. Tiny gaps remain on all scales. Figure 8.7(bottom) illustrates the splitting and interlacing of the Rössler flow.

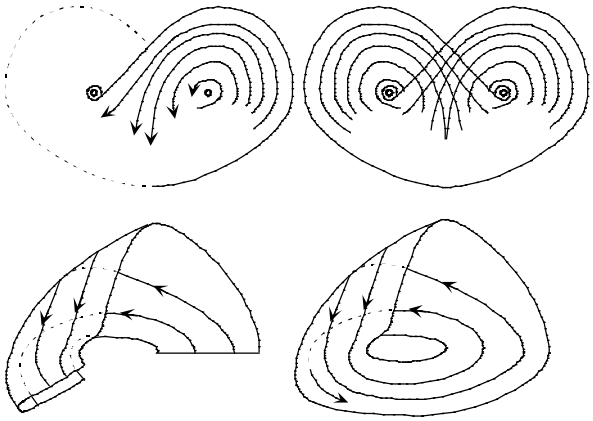

Figure 8.7: Splitting and interlacing of the Lorenz flow (top); continuous folding of the Rössler flow (bottom).

Both the Lorenz flow and the Rössler flow can be reduced to quasi-1D maps, either by taking a 2D **Poincaré** section or by plotting successive maxima against each other, as in Fig. 8.8. The steep slopes of the maps reveal that nearby trajectories diverge exponentially. This provides the extreme sensitivity to initial conditions that is the hallmark of chaotic attractors.

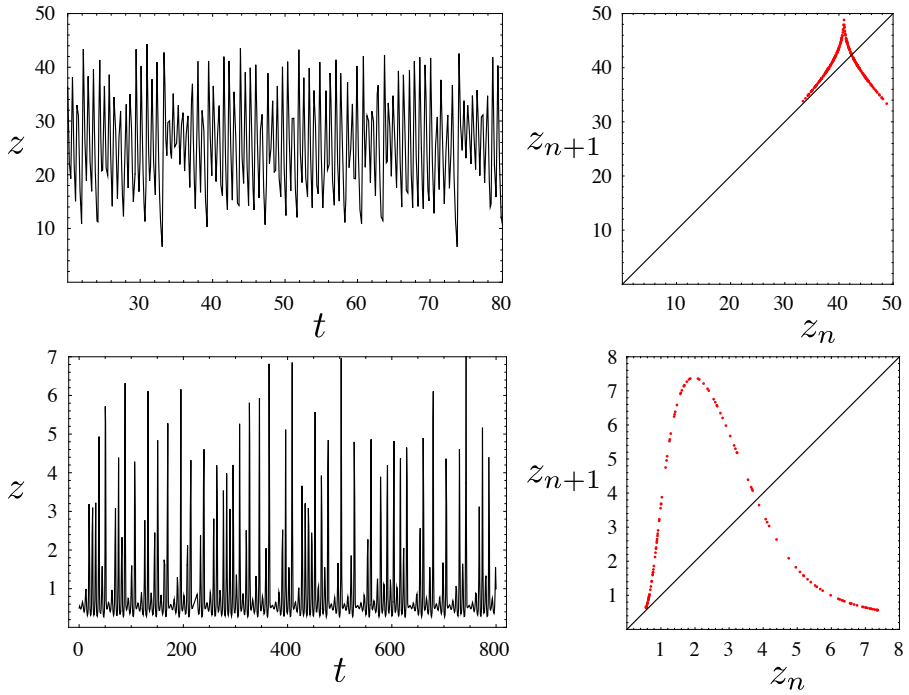

Figure 8.8: Lorenz z-flow and map of successive maxima (top); Rössler z-flow and map of successive maxima (bottom).

Problems

1. **Chua Circuit.** Use Mathematica to investigate the 3D flow from the circuit equations

$$\dot{x} = \alpha(y - x - g[x]), \tag{8.21a}$$
$$\dot{y} = x - y + z, \tag{8.21b}$$
$$\dot{z} = -\beta y, \tag{8.21c}$$

   where the nonlinear conductance

$$g[x] = m_1 x + \frac{1}{2}(m_0 - m_1)(|x+1| - |x-1|). \tag{8.22}$$

   Try $m_0 = -8/7$, $m_1 = -5/7$, $\alpha = 15.6$, and vary β. Can you find the **double scroll attractor**?

2. **Duffing Oscillator.** Use Mathematica to investigate the 3D flow from the forced, damped bistable oscillator described by

$$m\ddot{x} = ax - bx^3 - \gamma\dot{x} + A\cos[\omega t + \delta]. \tag{8.23}$$

   Try bistable potential well $a = 0.5$ and $b = 0.5$, mass $m = 1.0$, viscosity $\gamma = 0.15$, forcing amplitude and frequency $A = 0.19$ and $\omega = 0.833$. What happens as the phase shift δ varies? Strobe the motion once each forcing period to create a famous **strange attractor**. (Hint: Use Mathematica's Reap and Sow functions in conjunction with NDSolve and WhenEvent.)

Chapter 9

The N-Body Problem

9.1 2-Bodies

By 1682, Newton himself had solved the central force "inverse" problem (orbit to force law), using his laws of motion and gravity to recover Kepler's laws. By 1710, Johann Bernoulli had solved the "direct" problem (force law to orbit) for $2\times(3+3) = 12$ position and velocity components subject to $1+3+3+3-1-1 = 11$ motion constants (energy, center-of-mass position, linear momentum, angular momentum, eccentricity, with two interdependencies), where the only remaining degree of freedom is the zero of time.

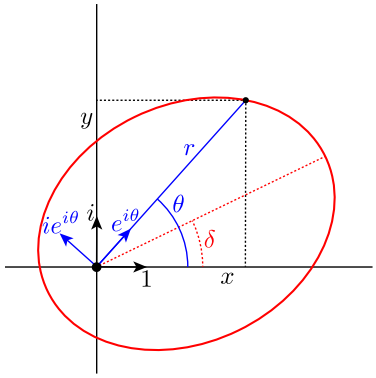

Figure 9.1: A Kepler ellipse rotated through angle δ in the complex plane, where $\{1, i\}$ and $\{e^{i\theta}, ie^{i\theta}\}$ act like rectangular and polar basis vectors.

In the *reduced* 2D problem, a point mass orbits a fixed center. Since the motion is planar by angular momentum conservation, efficiently solve it using complex numbers

$$z = x + iy = re^{i\theta}, \tag{9.1}$$

where $i = \sqrt{-1}$. In the complex plane, $\{1, i\}$ act like rectangular basis vectors, and $\{e^{i\theta}, ie^{i\theta}\}$ act like polar basis vectors, as in Fig. 9.1, because multiplying a complex number by $i = e^{i\pi/2}$ rotates it 90°. Suppose a mass m orbits a fixed mass M at $z[t]$. Its velocity

$$\begin{aligned} \dot{z} &= \dot{r}e^{i\theta} + re^{i\theta}i\theta \\ &= \left(\dot{r} + ir\dot{\theta}\right) e^{i\theta}, \end{aligned} \tag{9.2}$$

and its acceleration

$$\begin{aligned} \ddot{z} &= \left(\ddot{r} + i\dot{r}\dot{\theta} + ir\ddot{\theta}\right) e^{i\theta} + \left(\dot{r} + ir\dot{\theta}\right) e^{i\theta} i\dot{\theta} \\ &= \left(\ddot{r} - r\ddot{\theta}^2\right) e^{i\theta} + \left(r\ddot{\theta} + 2\dot{r}\dot{\theta}\right) ie^{i\theta}. \end{aligned} \tag{9.3}$$

where the dots are Newton's notation for time derivatives. Newton's second law of motion implies

$$\ddot{z} = -\frac{\mu}{r^2} e^{i\theta}, \tag{9.4}$$

where $\mu = GM$. Compare with Eq. 9.3 to infer

$$0 = r\ddot{\theta} + 2\dot{r}\dot{\theta} = \frac{2r\dot{r}\dot{\theta} + r^2\ddot{\theta}}{r} = \frac{1}{r}\left(r^2\dot{\theta}\right)^{\cdot} \tag{9.5}$$

and so

$$r^2\dot{\theta} = \text{constant} \equiv \lambda \tag{9.6}$$

is a motion constant (proportional to the angular momentum). Substitute into the motion Eq. 9.4 to find

$$\ddot{z} = -\frac{\mu}{\lambda}\dot{\theta}e^{i\theta} \tag{9.7}$$

or

$$i\lambda\ddot{z} = -i\mu\dot{\theta}e^{i\theta} = -\mu\left(e^{i\theta}\right)^{\cdot} \tag{9.8}$$

or

$$0 = \left(i\lambda\dot{z} + \mu e^{i\theta}\right)^{\cdot} \tag{9.9}$$

and so

$$i\lambda\dot{z} + \mu e^{i\theta} = \text{constant} \equiv \epsilon\, e^{i\delta} \tag{9.10}$$

is a motion constant (proportional to the orbital eccentricity), where ϵ and δ are real. Use the velocity and angular momentum to write

$$\epsilon\, e^{i\delta} = i\lambda\left(\dot{r} + ir\dot{\theta}\right) e^{i\theta} + \mu e^{i\theta} = \left(i\lambda\dot{r} - \frac{\lambda^2}{r} + \mu\right) e^{i\theta} \tag{9.11}$$

or

$$\epsilon\, e^{i(\delta-\theta)} = i\lambda\dot{r} - \frac{\lambda^2}{r} + \mu \tag{9.12}$$

whose real part is

$$\epsilon\cos[\delta - \theta] = -\frac{\lambda^2}{r} + \mu. \tag{9.13}$$

Solve for

$$r = \frac{\lambda^2}{\mu - \epsilon \cos[\delta - \theta]} = \frac{\ell}{1 - \mathfrak{e} \cos[\theta - \delta]}, \tag{9.14}$$

where $\ell = \lambda^2/\mu$ and $\mathfrak{e} = \epsilon/\mu$, which is the equation of an ellipse focused at the origin and rotated through an angle δ.

Although Newton's gravitational force is spherically and circularly symmetric, the Kepler solutions are elliptical, an example of **spontaneous symmetry breaking**. Figure 9.2 illustrates and orbit. Kepler tried unsuccessfully to fit a circle to Mars orbit, but reluctantly settled for an ellipse. However, his circle is in velocity space.

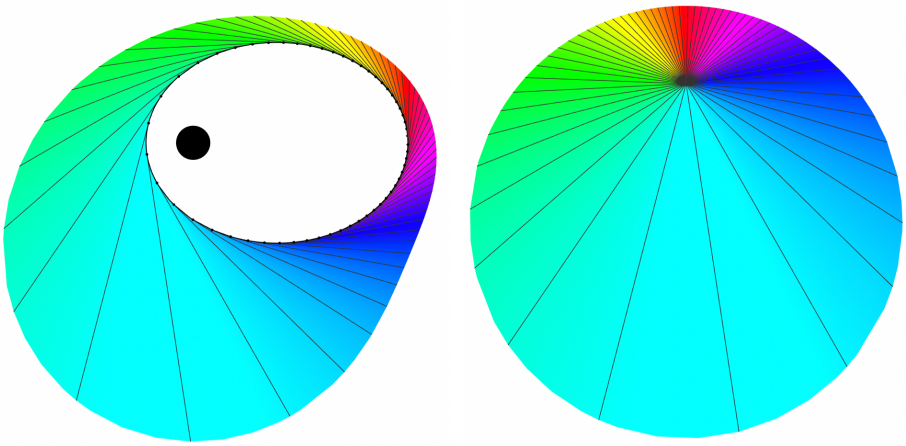

Figure 9.2: Position versus time for a mass bound to another by gravity sweeps out an ellipse; tangents are velocities and rainbow hues code time: a $\{z, \dot{z}, t\} = \{x, y, \dot{x}, \dot{y}, t\}$ 5-dimensional graph (left). Just the velocity vectors sweep out a circle (right), which might have pleased Kepler.

9.2 3-Bodies

In 1895, for his 60th birthday, King Oscar II of Sweden and Norway established a mathematics prize, whose first challenge was finding a convergent power series sollution to the 3-body problem for $3 \times (3 + 3) = 18$ position and momentum components subject to only $1+3+3+3 = 10$ motion constants (energy, center-of-mass position, linear momentum, angular momentum). No one succeeded, although the prize went to Henri Poincaré, for his discovery of what we now call chaos [11].

In 1913, by excluding a negligible set of initial conditions of zero angular moment (to eliminate triple collisions), Karl Sundman proved the existence

of a convergent power series solution for the 3-body problem [15]. But infinitely many possible double collisions causes this series to converge impractically slowly, and Sundman's solution does not contradict Poincaré's discovery of deterministic but practically unpredictable motion.

9.3 Restricted 3-Body Problem

9.3.1 Inertial Reference Frame

Poincaré considered the **restricted, planar, circular 3-body problem**, where a small mass moves in the plane of two large masses orbiting each other in circles, and the small mass is pulled by the large masses but not vice versa.

Assume the large masses

$$M_1 = fM, \tag{9.15a}$$
$$M_2 = (1-f)M \tag{9.15b}$$

and their distances from their center-of-mass

$$d_1 = dM_2/M, \tag{9.16a}$$
$$d_2 = dM_1/M. \tag{9.16b}$$

By **Kepler's third law**, the period of the large masses

$$\frac{2\pi}{\omega} = T = \sqrt{\frac{4\pi^2}{GM}d^3}. \tag{9.17}$$

The motion of the large masses

$$\vec{d_1} = +d_1\{\cos\omega t, \sin\omega t, 0\}, \tag{9.18a}$$
$$\begin{aligned}\vec{d_2} &= -d_2\{\cos\omega t, \sin\omega t, 0\} \\ &= +d_2\{\cos[\omega t+\pi], \sin[\omega t+\pi], 0\}.\end{aligned} \tag{9.18b}$$

Position of small mass relative to large masses

$$\delta\vec{r}_1 = \vec{r} - \vec{d_1}, \tag{9.19a}$$
$$\delta\vec{r}_2 = \vec{r} - \vec{d_2}. \tag{9.19b}$$

Newton's second law implies

$$\ddot{\vec{r}} = -\frac{GM_1}{\delta r_1^2}\delta\hat{r}_1 - \frac{GM_2}{\delta r_2^2}\delta\hat{r}_2. \tag{9.20}$$

Initial conditions

$$\vec{r}[0] = \{x_0, 0, 0\}, \tag{9.21a}$$
$$\dot{\vec{r}}[0] = \{0, v_0 + \omega x_0, 0\} \tag{9.21b}$$

Table 9.1: Planar circular 3-body problem parameters.

description	symbol	value
gravitational constant	GM	1
large masses distance	d	1
large masses fraction	f	0.4
small mass initial distance	x_0	-0.11659
small mass initial speed	v_0	$+1.39641$
pseudo-energy (Jacobi constant)	ϵ	-1.70711
unstable manifold slope	s	-1.818

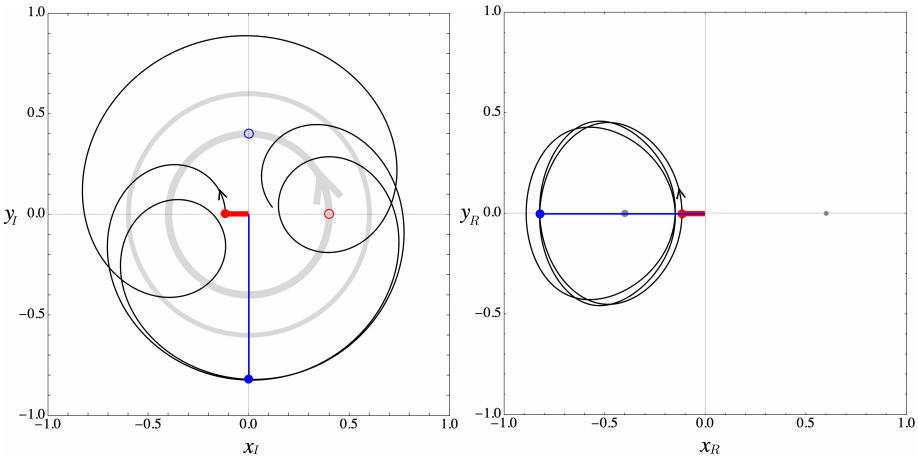

Figure 9.3: Small mass (black) orbiting large masses (gray) in an inertial reference frame (left) and a rotating frame (right). Start (red) and later (blue) positions highlight correspondence.

complete the **initial value problem**, and Table 9.1 lists the parameters. Numerical integration generates the Fig. 9.3(left) orbit.

Because the small mass does not pull the large masses in this model, energy is not conserved, but the **specific pseudo-energy**

$$\epsilon = \frac{\tilde{E}}{m} = \frac{1}{2}\dot{\vec{r}}\cdot\dot{\vec{r}} - \frac{GM_1}{\delta r_1} - \frac{GM_2}{\delta r_2} - \vec{\omega}\cdot\vec{\lambda}, \tag{9.22}$$

where the **specific angular momentum**

$$\vec{\lambda} = \frac{\vec{L}}{m} = \vec{r}\times\dot{\vec{r}}, \tag{9.23}$$

is proportional to the **Jacobi motion constant**.

9.3.2 Rotating Reference Frame

In a reference frame rotating with the large masses, they are still, and the small mass motion equations

$$\ddot{\vec{r}} = -\frac{GM_1}{\delta r_1^2}\delta\hat{r}_1 - \frac{GM_2}{\delta r_2^2}\delta\hat{r}_2 - \vec{\omega}\times(\vec{\omega}\times\vec{r}) - 2\vec{\omega}\times\dot{\vec{r}} \tag{9.24}$$

include centrifugal and coriolis **pseudo-accelerations**. Initial conditions

$$\vec{r}[0] = \{x_0, 0, 0\}, \tag{9.25a}$$

$$\dot{\vec{r}}[0] = \{0, v_0, 0\}. \tag{9.25b}$$

Numerical integration generates the rotating Fig. 9.3(right) orbit. The **specific pseudo-energy**

$$\epsilon = \frac{\tilde{E}}{m} = \frac{1}{2}\dot{\vec{r}}\cdot\dot{\vec{r}} - \frac{GM_1}{\delta r_1} - \frac{GM_2}{\delta r_2} - \frac{1}{2}\vec{r}\cdot\vec{r} \tag{9.26}$$

is constant.

9.3.3 Poincaré Section

The $\{x, y, v_x, v_y\}$ state space flow of the small mass m is 4D. Figure 9.4 includes a 3D $\{x, y, v_x\}$ projection (top) and a 2D $\{x, 0, v_x, v_0\}$ cross section (bottom). The flow is a continuous curve while the section is a set of points, the two trefoils, each consisting of three hyperbolic period-6 points whose stable and unstable manifolds enclose three "exterior" elliptical points and one "interior" elliptical point, as in Fig. 9.5, where the colors code sections of orbits with slightly different initial conditions.

In his King Oscar prize-winning essay, Poincaré thought that the stable and unstable manifolds of adjacent hyperbolic points coincide. But just *after* his essay was published, he realized that they could cross **transversely**, and each crossing map to another crossing infinitely often, with the manifolds oscillating with larger and larger amplitude, as in Fig. 9.6, creating a **chaotic tangle**. He wrote, "These intersections form a sort of trellis, web, or infinitely tight mesh ... One is struck by the complexity of this figure, which I shall not even attempt to draw." His publication was recalled, revised, and republished.

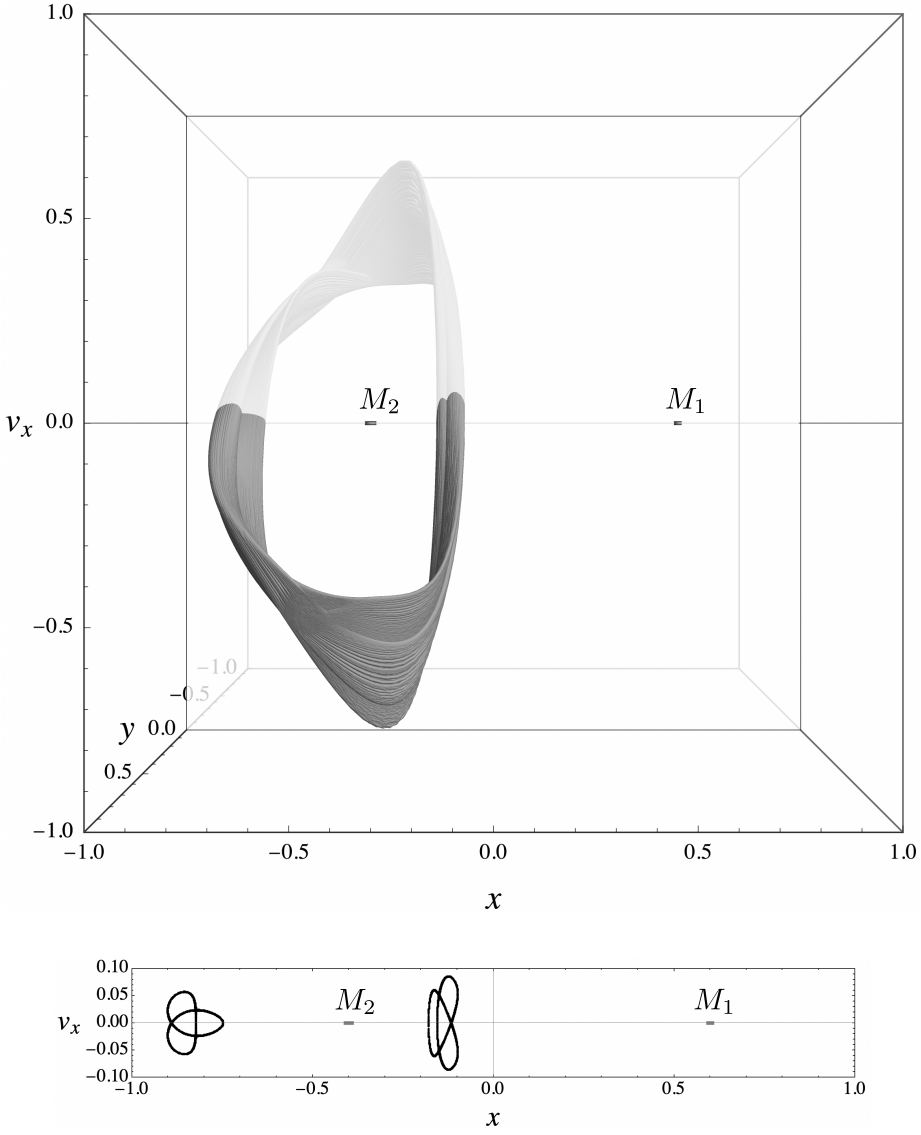

Figure 9.4: Small mass 3D $\{x, y, v_x\}$ projection of full 4D $\{x, y, v_x, v_y\}$ flow (top); $\{x, 0, v_x, v_0\}$ cross section (bottom).

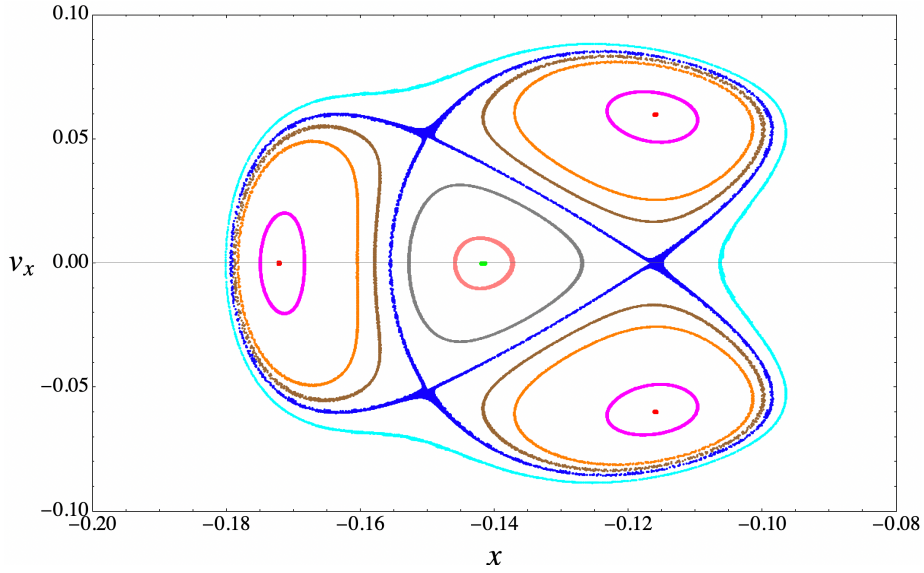

Figure 9.5: Close-up of small mass Poincaré section right half, where point colors correspond to slightly different initial conditions. Colored "curves" are *not* continuously traversed.

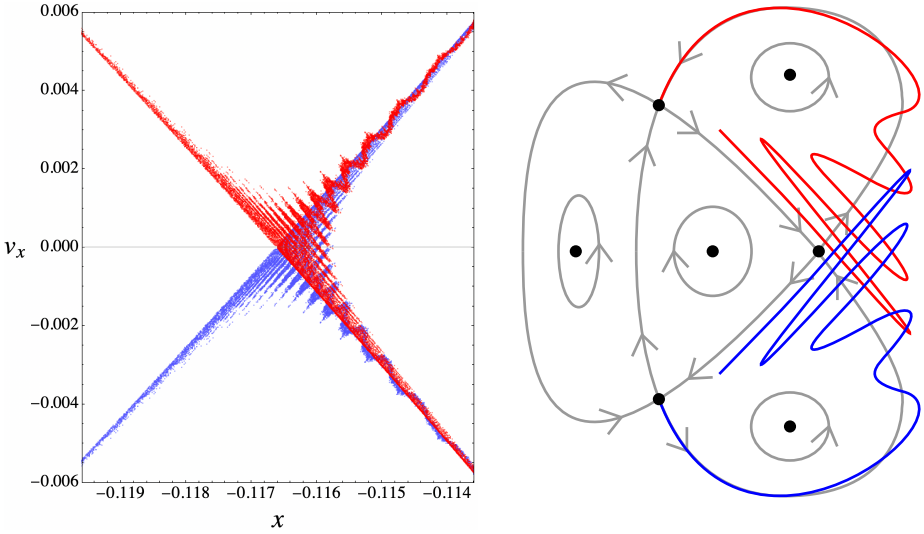

Figure 9.6: Further closeup of the rightmost unstable hyperbolic point including a Poincaré trellis or chaotic tangle (left). Schematic diagram illustrates a state space flow dominated by three hyperbolic period-6 fixed points (top-right).

Problems

1. **Rectangular Ellipse**. Transform the Eq. 9.14 ellipse into rectangular coordinates, and write it in the standard form of an ellipse. Find the major and minor radii.

2. **Inertial Jacobi Constant**. Show that the time-derivative of the Eq. 9.22 inertial pseudo-energy vanishes.

3. **Rotational Jacobi Constant**. Show that the time-derivative of the Eq. 9.26 rotational pseudo-energy vanishes.

Chapter 10

Fractals

After long times, the Lorenz and Rössler flows settle down to complicated state space sets called fractals, a term coined by Benoit Mandelbrot in the 1970s. Fractals are complex geometric shapes with fine structure at arbitrarily small scales. This fine structure, while sometimes exactly self-similar, is often only approximately or statistically self-similar.

10.1 Canonical Examples

10.1.1 Cantor Dust

The prototypical fractal set was invented in the late 1800s by mathematician Georg Cantor. Cantor's "middle-third" set can be approached via the following **recursive** construction. Begin with the unit interval and remove the (open) middle thirds of each successive remaining interval, as in Fig. 10.1.

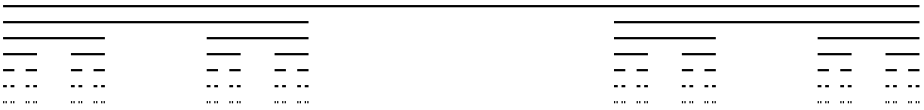

Figure 10.1: First six steps in the recursive construction of the Cantor dust.

If the set remaining after the nth step is C_n, then $C \equiv C_\infty = \lim_{n\to\infty} C_n$ is the Cantor set. Apparently, it consists of an infinite number of infinitesimal pieces separated by gaps of various sizes, large and small.

The Cantor set C is an invaluable counter-example in **topology**, as it simultaneously manifests a number of seemingly contradictory properties. C is a "large" set in the sense that it contains an uncountable infinity of points, yet C is a "small" in that its total length is zero: $L_n = (2/3)^n \to 0$ as $n \to \infty$. Because C contains no intervals, it is totally disconnected, yet because each of

its points has (infinitely many) neighbors arbitrarily close, C has no isolated points: its points are simultaneously "spread apart" and "packed together".

Clearly, C has structure on all scales. In fact, it is exactly self-similar, made of smaller copies of itself, one part being equal to the whole. It is more than a point but less than a line and can be assigned a **dimension** between 0 and 1.

10.1.2 Koch Curve

A second prototypical fractal set was invented by mathematician Helge von Koch. Koch's set can be approached via the following **recursive** construction. Begin with the unit interval, and erect equilateral triangles on each successive middle third, as in Fig. 10.2.

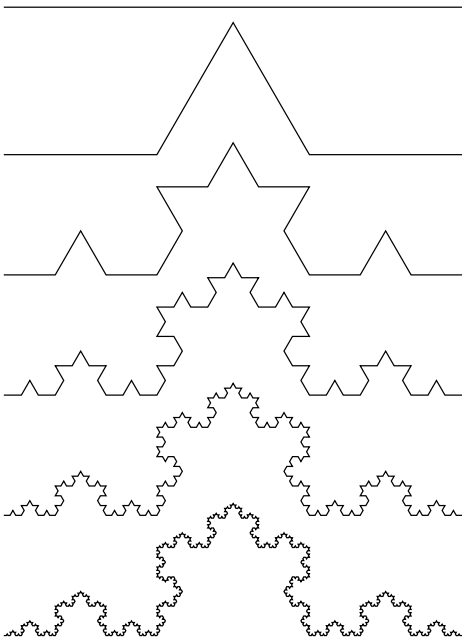

Figure 10.2: First five steps in the recursive construction of the Koch curve.

If the curve at the nth step is K_n, then $K \equiv K_\infty = \lim_{n\to} K_n$ is the Koch curve. Apparently, it consists of an infinite wiggly, nowhere differentiable curve.

The Koch curve K suggests a very rugged coastline and recalls Mandelbrot's famous article "How long is the coast of Britain?" [8] inspired by work of Lewis Fry Richardson. In fact, K is infinitely long: $L_n = (4/3)^n \to \infty$ as $n \to \infty$.

Clearly, K has structure on all scales. In fact, it is exactly self-similar, made of smaller copies of itself, one part being equal to the whole. It is more than a line but less than an area and can be assigned a dimension between 1 and 2.

10.2 Dimension Generalizations

10.2.1 Coordinate

To generalize the notion of dimension to include the fractional dimensions of fractal sets, start with the very intuitive **coordinate dimension**. The coordinate dimension of a set is the minimum number of coordinates needed to locate every point in the set. For example, a line has coordinate dimension 1 because points along the line can be located by a single coordinate, say, the distance from one end. Similarly, a plane has coordinate dimension 2 because points in the plane can be located by 2 coordinates, rectangular $\{x, y\}$ or polar $\{r, \theta\}$.

Unfortunately, the coordinate dimension fails for fractal sets. For example, a point in the Koch curve K cannot be located by its distance from one end because the curve is infinitely long and every point is infinitely far from every other point. Also, a point in the Cantor dust C cannot be located by its distance from one end because it is a set of measure zero.

10.2.2 Similarity

First generalize the notion dimension to include exactly self-similar sets like the Cantor dust and the Koch curve, which consist of scaled-down copies of themselves. Familiar self-similar sets include lines, squares, and cubes.

Notice that a square consists of $N = 4$ copies of itself each scaled down by a factor of $s = 2$, or $N = 9$ copies of itself each scaled down by a factor of $s = 3$, as in Fig. 10.3(top). More generally, a square consists of $N = s^2$ copies of itself scaled down by a factor of s. Similarly, a cube consists of $N = 8$ copies of itself scaled down by a factor of $s = 2$, or $N = 27$ copies of itself scaled down by a factor of $s = 3$, as in Fig. 10.3(bottom). More generally, a cube consists of $N = s^3$ copies of itself scaled down by a factor of s.

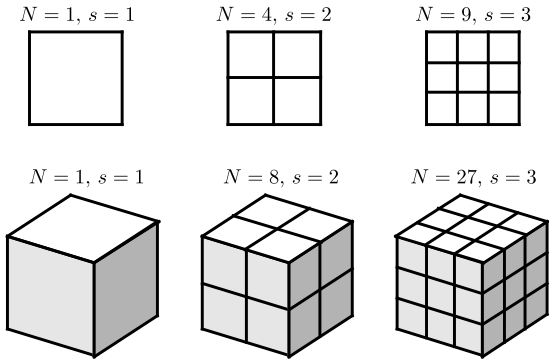

Figure 10.3: A square consists of $N = s^2$ copies of itself scaled down by a factor s (top), while a cube consists of $N = s^3$ copies of itself scaled down by a factor s (bottom).

An arbitrary self-similar set consists of $N = s^d$ copies of itself scaled down by a factor of s, where d is the similarity dimension of the set. Formally, the similarity dimension can be expressed as

$$d = \frac{\log N}{\log s}. \tag{10.1}$$

The Cantor dust C consists of 2 copies of itself, each scaled down by a factor of 3. Hence, the similarity dimension of C is $d = \log 2/\log 3 \approx 0.63 < 1$. The Koch curve K consists of 4 copies of itself, each scaled down by a factor of 3. Hence, the similarity dimension of K is $d = \log 4/\log 3 \approx 1.26 > 1$.

10.2.3 Box

To handle fractal sets that are not exactly self-similar, generalize the notion of dimension even further. Multiple ways to do this exist, but each involves measuring a set at a certain resolution ϵ and studying how its size varies as the resolution increases $\epsilon \to 0$.

Consider a line (embedded in a plane). Imagine covering the line with boxes of size ϵ, as in Fig. 10.4(left). Let N_ϵ be the minimum number of boxes needed to cover the line. Clearly, halving the size of each box ϵ, doubles the number of boxes N_ϵ. Thus, $N_\epsilon \propto \epsilon^{-1}$ for a line. Similarly, imagine covering an area with boxes of size ϵ, as in Fig. 10.4(right). Halving the size of each box ϵ quadruples the number of boxes N_ϵ. Thus, $N_\epsilon \propto \epsilon^{-2}$ for an area.

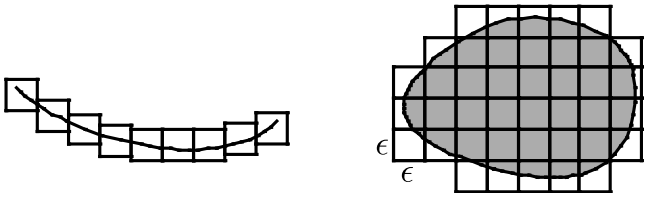

Figure 10.4: Minimal covering of a line by $N_\epsilon \propto \epsilon^{-1}$ boxes of size ϵ (left), and minimal covering of an area by $N_\epsilon \propto \epsilon^{-2}$ boxes of size ϵ (right).

For a minimal covering of an arbitrary set, demand that $N_\epsilon \propto \epsilon^{-d}$, where d is the box dimension of the set. (The **box dimension** is also known as the **capacity dimension**, and it is related to the more technical **Hausdorff dimension**.) Formally, write

$$N_\epsilon = N_1 \epsilon^{-d}. \tag{10.2}$$

A plot $\log N_\epsilon$ versus $\log \epsilon$ asymptotes to a straight line of slope $-d$, for small ϵ, as in Fig. 10.5. However, the plot departs from the straight line, for large ϵ, because only a crude minimal covering of a given set is possible, for too large boxes. To formally eliminate this ambiguity, take the limit

$$d = \lim_{\epsilon \to 0} \frac{\log N_\epsilon}{\log \epsilon^{-1}} = -\lim_{\epsilon \to 0} \frac{\log N_\epsilon}{\log \epsilon}. \tag{10.3}$$

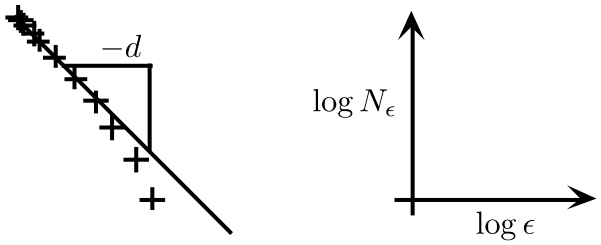

Figure 10.5: Extracting a box dimension from covering data, with typical errors at large ϵ.

Exploit the recursive definition of the Cantor dust and the Koch curve to find their box dimensions. At the nth stage in the construction of the Cantor dust C, $N = 2^n$ boxes of length $\epsilon = 1/3^n$ will just cover the set. Because $\epsilon \to 0$ as $n \to$,

$$d = \lim_{n\to\infty} \frac{\log 2^n}{\log 3^n} = \frac{\log 2}{\log 3} \approx 0.63 \tag{10.4}$$

as before. Similarly, at the nth stage in the construction of the Koch curve K, $N = 4^n$ boxes of length $\epsilon = 1/3^n$ will just cover the set. Hence,

$$d = \lim_{n\to\infty} \frac{\log 4^n}{\log 3^n} = \frac{\log 4}{\log 3} \approx 1.26 \tag{10.5}$$

as before.

10.2.4 Correlation

Unfortunately, the box dimension is often prohibitively computationally intensive, especially when applied to attractors of high dimension. Seek a more efficient dimension algorithm to apply to dynamical data.

A starting point is the fact that, crudely speaking, a point has more close neighbors in higher dimensions than in lower dimensions. For example, the number of points N_ϵ in a d-dimensional ball (interval, disk, sphere, hypersphere) of radius ϵ scales like $N_\epsilon \propto \epsilon^d$, as in Fig. 10.6.

Embed an attractor in a sufficiently large space, choose a point on the attractor, find the number of points N_ϵ in the attractor within a ball of radius ϵ, average this over the attractor to find $\bar{N}_\epsilon$, and demand that $\bar{N}_\epsilon \propto \epsilon^d$, where d is the correlation dimension of the attractor. Formally, write

$$\bar{N}_\epsilon = \bar{N}_1 \epsilon^d. \tag{10.6}$$

A plot $\log \bar{N}_\epsilon$ versus $\log \epsilon$ is linear with slope d, for ϵ not too small or not too large. However, the data saturates for small and large ϵ, as in Fig. 10.7. The balls must be smaller than the size of the attractor but larger than the minimum separation between points on the attractor (whose resolution is typically limited by experimental or numerical constraints).

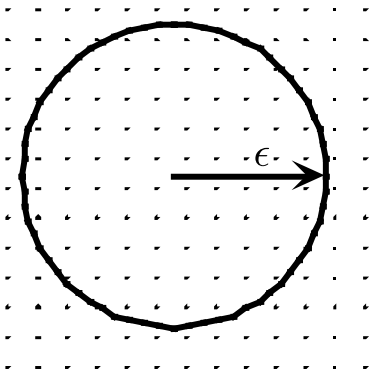

Figure 10.6: Number of points in a circle scales like the area or radius squared.

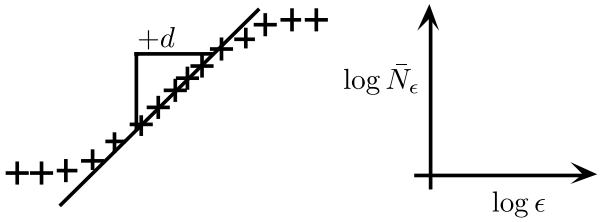

Figure 10.7: Extracting a correlation dimension, with data saturating at small and large ϵ.

Because the correlation dimension is sensitive to the density of points on the attractor, it equals the box dimension only if the points on the attractor are uniformly distributed. This is not always the case, but the correlation dimension is always greater than or equal to the box dimension.

10.3 Applications

At the onset of chaos $\mu \approx 3.56994$, the correlation dimension of the **logistic map attractor** is $d = 0.500 \pm 0.005$. At the standard parameters $\rho = 28$, $\sigma = 10$, and $\beta = 8/3$, the correlation dimension of the **Lorenz attractor** is $d = 2.05 \pm 0.01$.

Problems

1. **Koch Variation.** To what dimension does the following sequence of curves converge?

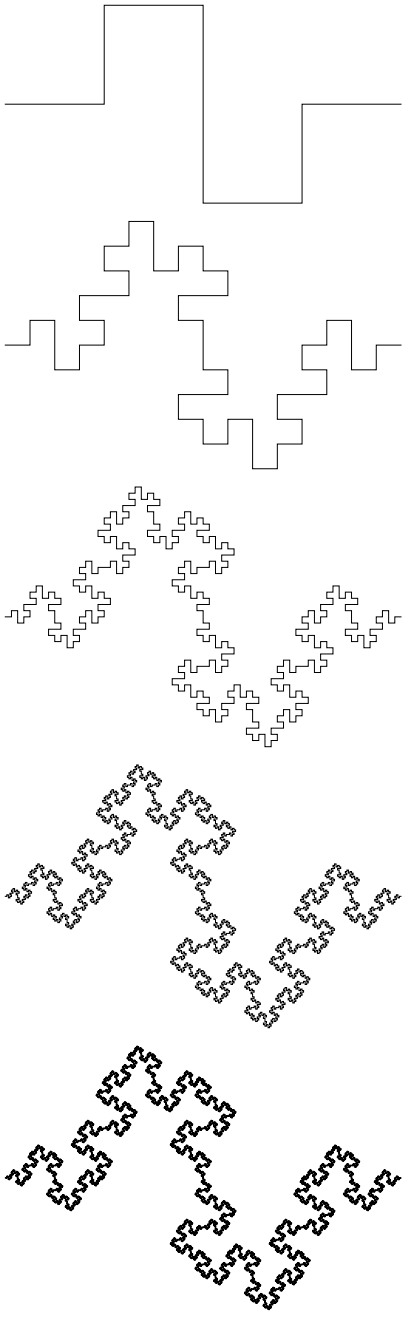

Appendix A

Mathematics Background

A.1 Complex Numbers

Complex numbers are used extensively in quantum mechanics. They also enable beautiful theorems in mathematics, like the Fundamental Theorem of Algebra, which says that an nth degree polynomial has exactly n complex roots

$$z = x + iy, \tag{A.1}$$

where x and y are real numbers and the *imaginary unit*

$$i = \sqrt{-1}. \tag{A.2}$$

A common operation is *complex conjugation*

$$z^* = x - iy = \overline{z}. \tag{A.3}$$

The real and imaginary parts of a complex number,

$$\operatorname{Re} z = \frac{z + z^*}{2} = x \tag{A.4}$$

and

$$\operatorname{Im} z = \frac{z - z^*}{2i} = y \tag{A.5}$$

are both real. The *modulus*

$$\operatorname{mod} z = |z| = \sqrt{z^* z} = \sqrt{z z^*} = \sqrt{x^2 + y^2} \tag{A.6}$$

and *argument*

$$\arg z = \operatorname{atan}\left[\frac{y}{x}\right] \tag{A.7}$$

offer an alternate way of specifying the complex number, as in Figure A.1.

Euler's theorem

$$e^{i\theta} = \cos\theta + i \sin\theta, \tag{A.8}$$

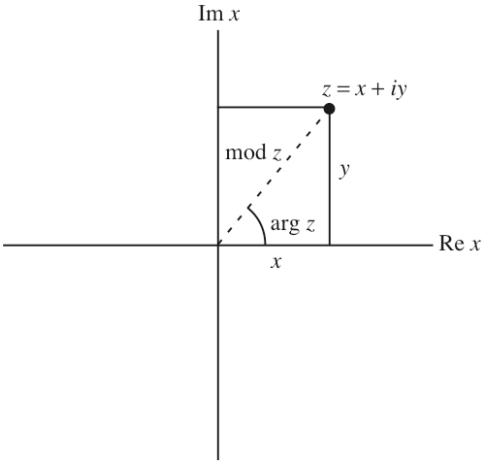

Figure A.1: The complex plane.

which can be proved by expanding each term in a Taylor series, allows us to interconvert the *polar* and *rectangular* representations of a complex number by

$$re^{i\theta} = r\cos\theta + ir\sin\theta = x + iy, \tag{A.9}$$

where $r = \mathrm{mod} z$ and $\theta = \arg z$. A special case of Euler's theorem, $\theta = \pi$, generates the remarkable formula (purportedly engraved on Euler's tombstone)

$$e^{i\pi} + 1 = 0, \tag{A.10}$$

which elegantly and surprisingly interconnects the base of the natural logarithms, the imaginary unit, the ratio of a circle's circumference to its diameter, unity, and zero!

A.2 Hyperbolic Functions

Hyperbolic functions are intimately related to trigonometric functions. Recall Euler's theorem

$$e^{i\theta} = \cos\theta + i\sin\theta \tag{A.11}$$

and its complex conjugate

$$e^{-i\theta} = \cos\theta - i\sin\theta. \tag{A.12}$$

Adding and subtracting implies

$$\cos\theta = \frac{e^{i\theta} + e^{-i\theta}}{2} \tag{A.13}$$

and

$$\sin\theta = \frac{e^{i\theta} - e^{-i\theta}}{2i}. \tag{A.14}$$

The substitution $\theta \to i\theta$ replaces a real angle with an imaginary angle and generates hyperbolic functions from trigonometric functions. For example,

$$\cos[i\theta] = \frac{e^{-\theta} + e^{\theta}}{2} = \cosh\theta \tag{A.15}$$

and

$$\sin[i\theta] = \frac{e^{-\theta} - e^{\theta}}{2i} = i\frac{e^{\theta} - e^{-\theta}}{2} = i\sinh\theta. \tag{A.16}$$

Hence,

$$\cosh[i\theta] = \frac{e^{-i\theta} + e^{i\theta}}{2} = \cos\theta \tag{A.17}$$

and

$$\sinh[i\theta] = \frac{e^{-i\theta} - e^{i\theta}}{2i} = i\frac{e^{i\theta} - e^{-i\theta}}{2} = i\sin\theta. \tag{A.18}$$

Notice how the cosine "swallows" the i when becoming a hyperbolic cosine, while the sine "spits out" the i when becoming a hyperbolic sine. (Similarly, the cosine swallows a minus sign, $\cos[-\theta] = \cos\theta$, while the sine spits out a minus sign, $\sin[-\theta] = -\sin[\theta]$.)

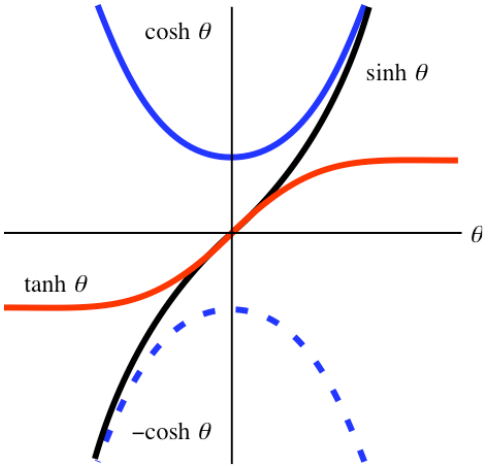

Figure A.2: Graphs of hyperbolic functions, with $\tanh\theta = \sinh\theta/\cosh\theta$.

Every trigonometric identity corresponds to a hyperbolic identity. For example, take $(\cos\theta)^2 + (\sin\theta)^2 = 1$ and substitute $\theta \to i\theta$ to get $(\cos[i\theta])^2 + (\sin[i\theta])^2 = 1$ or

$$(\cosh\theta)^2 - (\sinh\theta)^2 = 1. \tag{A.19}$$

The hyperbolic functions are real, exponential, and nonrepeating functions, as depicted in Figure A.2.

A.3 Spatial Rotations

Spatial rotations are analogues for Lorentz-Einstein transformations. Suppose an (x', y') coordinate system is rotated counterclockwise through an angle θ relative to an (x, y) coordinate system, as in Figure A.3.

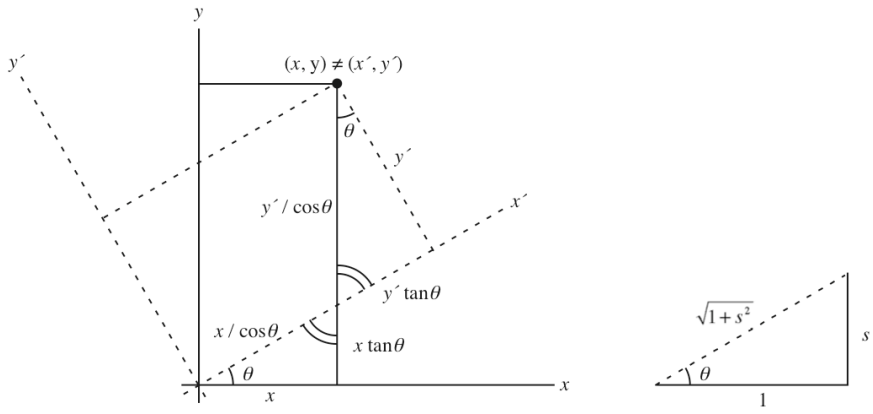

Figure A.3: Two coordinate systems with a common origin but rotated through an angle θ relative to each other.

From the trigonometry, the y-coordinate can be expressed as

$$y = \frac{y'}{\cos\theta} + x\tan\theta, \tag{A.20}$$

which implies

$$y' = -x\sin\theta + y\cos\theta. \tag{A.21}$$

Similarly, the x'-coordinate can be expressed as

$$x' = \frac{x}{\cos\theta} + y'\tan\theta, \tag{A.22}$$

which implies

$$x = x'\cos\theta - y'\sin\theta \tag{A.23}$$

or, simultaneously negating θ and interchanging primes and un-primes,

$$x' = x\cos\theta + y\sin\theta. \tag{A.24}$$

We can summarize the rotation transformation of Equation A.24 and Equation A.21 in the matrix equation

$$\begin{bmatrix} x' \\ y' \end{bmatrix} = \begin{bmatrix} \cos\theta & \sin\theta \\ -\sin\theta & \cos\theta \end{bmatrix} \begin{bmatrix} x \\ y \end{bmatrix}, \tag{A.25}$$

which readily checks for $\theta = 0$ and $\theta = \pi/2$.

In terms of the relative slope $s = \tan\theta$, $\cos\theta = 1/\sqrt{1+s^2} = \Gamma$ and $\sin\theta = s/\sqrt{1+s^2} = s\Gamma$, and hence

$$\begin{bmatrix} x' \\ y' \end{bmatrix} = \begin{bmatrix} \Gamma & s\Gamma \\ -s\Gamma & \Gamma \end{bmatrix} \begin{bmatrix} x \\ y \end{bmatrix} = \Gamma \begin{bmatrix} 1 & s \\ -s & 1 \end{bmatrix} \begin{bmatrix} x \\ y \end{bmatrix}. \tag{A.26}$$

A.4 Partial Derivatives

In one-dimension, the function

$$f[x] = 3x^2 + 1 \tag{A.27}$$

has the **derivative**

$$\frac{df}{dx} = 6x + 0 = 6x. \tag{A.28}$$

In two dimensions, the function

$$f[x, y] = 3xy^2 + 2x + 3y + 2 \tag{A.29}$$

has the **partial derivatives**

$$\frac{\partial f}{\partial x} = 3y^2 + 2 + 0 + 0 = 3y^2 + 2, \tag{A.30a}$$

$$\frac{\partial f}{\partial y} = 6xy + 0 + 3 + 2 = 6xy + 5, \tag{A.30b}$$

which are just like ordinary derivatives, but with other variables held constant.

A.5 Function Notation

Standard mathematics notation suffers a serious ambiguity involving parentheses. In particular, parentheses can be used to denote multiplication, as in $a(b + c) = ab + ac$ and $f(g) = fg$, or they can be used to denote a function evaluated at a point, as in $f(t)$ and $g(b + c)$. One must sometimes struggle to determine the intended meaning from context.

In this text, to avoid ambiguity, round parentheses $(\bullet)$ always denote multiplication, while square brackets $[\bullet]$ always denote function evaluation. Thus, $f[x]$ denotes a function evaluated at a point, while $a(b) = ab$ denotes the product of two quantities. The Wolfram Language and Mathematica employ the same convention.

Problems

1. **Complex Plotting**. Plot the following numbers and their complex conjugates in the complex $z = x + iy = \{x, y\}$ plane.

   (a) $1 + i$

   (b) $1 - i\sqrt{3}$

   (c) $\sqrt{2}e^{-i\pi/4}$

2. **Complex Simplification**. Simplify the following numbers to the form $x + iy$.

   (a) $\dfrac{1}{1+i}$

   (b) $25e^{2i}$

   (c) $\dfrac{3i-7}{i+4}$

   (d) $\left(\dfrac{1+i}{1-i}\right)^{137}$ (Hint: Don't use a calculator!)

   (e) i^i (Hint: Find the principal value.)

3. **Complex Identities**. Derive the following equations.

   (a) $e^{i\theta} = \cos\theta + i\sin\theta$ (Hint: Try infinite power series expansion.)

   (b) $e^{i\pi} + 1 = 0$

   (c) $\cos\theta = \dfrac{e^{i\theta} + e^{-i\theta}}{2}$

   (d) $\sin\theta = \dfrac{e^{i\theta} - e^{-i\theta}}{2i}$

Bibliography

[1] Alan Cromer. Stable solutions using the Euler approximation. *American Journal of Physics*, 49(5):455–459, 1981.

[2] Adrien Douady and John H. Hubbard. Etude dynamique des polynômes complexes. *Prépublications mathémathiques d'Orsay*, 2/4, 1984/1985.

[3] Mitchell J. Feigenbaum. Quantitative universality for a class of nonlinear transformations. *Journal of Statistical Physics*, 19(1):25–52, July 1978.

[4] M. Hénon. A two-dimensional mapping with a strange attractor. *Communications in Mathematical Physics*, 50(1):69–77, 1976.

[5] Tien-Yien Li and James A. Yorke. Period three implies chaos. *The American Mathematical Monthly*, 82(10):985–992, 1975.

[6] Edward N. Lorenz. Deterministic nonperiodic flow. *Journal of Atmospheric Sciences*, 20(2):130 – 141, 1 March 1963.

[7] Edward N. Lorenz. Predictability: Does the flap of a butterfly's wings in Brazil set off a tornado in Texas? 139th Annual Meeting of the American Association for the Advancement of Science, 29 December 1972.

[8] Benoit Mandelbrot. How long is the coast of Britain? Statistical self-similarity and fractional dimension. *Science*, 156(3775):636–638, 1967.

[9] Benoit Mandelbrot. Fractal aspects of the iteration of $\lambda \to \lambda z(1-z)$ for complex λ, z. *Annals of the New York Academy of Sciences*, 357:249/259, 1980.

[10] Robert M. May. Simple mathematical models with very complicated dynamics. *Nature*, 261(5560):459–467, 1976.

[11] Henri Poincaré. Sur le problème des trois corps et les équations de la dynamique. *Acta Mathematica*, 13:1–270, 1890.

[12] Lewis Fry Richardson. *Weather Prediction by Numerical Process*. Cambridge University Press, 1922.

[13] O. E. Rössler. An equation for continuous chaos. *Physics Letters A*, 57(5):397 – 398, 1976.

[14] A. N. Sharkovsky. Co-existence of cycles of a continuous mapping of the line into itself. *Ukrainian Math. J.*, 16:6171, 1964.

[15] Karl F. Sundman. Mémoire sur le problème des trois corps. *Acta Math.*, 36:105–179, 1913.